ABSTRACT

Title of Dissertation: OUTGOING LONGWAVE RADIATION AT THE TOP OF ATMOSPHERE: ALGORITHM DEVELOPMENT, COMPREHENSIVE EVALUATIONS, AND CASE STUDIES

Yuan Zhou, Doctor of Philosophy, 2019

Dissertation directed by: Dr. Shunlin Liang, Professor

Department of Geographical Sciences

Outgoing longwave radiation (OLR) at the top of the atmosphere (TOA) represents the total outgoing radiative flux emitted from the Earth's surface and atmosphere in the thermal-infrared wavelength range. It plays a role as a powerful diagnostic of Earth's climate system response to absorbed incoming solar radiation (ASR). Long-term measurements of OLR are essential for quantitatively understanding the climate system and its variability. However, inconsistencies and uncertainties have been always existing in OLR estimation among different datasets and algorithms.

The objective of this dissertation is to carry out a comprehensive investigation on OLR with three specific questions: 1) How large are the discrepancies in estimates from various OLR products and what are their spatial and temporal patterns? 2) How to generate more accurate and more useful OLR estimates from multi-spectral satellite observations? 3) How does OLR respond to extreme climate and geological events such as El Niño/Southern Oscillation (ENSO) and giant earthquakes, and does the newly developed OLR products have any advantage to predict such events?

To address those questions, this dissertation 1) conducts comprehensive evaluations on multiple OLR datasets by performing inter-comparisons among different satellite retrieved OLR products and different reanalysis OLR datasets, respectively; 2) develops an algorithm framework for estimating OLR from multi-spectral satellite observations based on radiative transfer simulations and statistical approaches; 3) investigates the correlation between OLR anomalies and historical ENSO events and a typical giant earthquake, and makes an attempt to predict ENSO and earthquake through OLR variations. Results indicate that 1) obvious discrepancies exist among different OLR datasets, with the two Japanese Meteorological Agency's (JMA) Japanese Reanalysis project (JRA) OLRs displays the largest differences with others. However, all OLR products and datasets have comparable magnitude of inter-annual variability and monthly/seasonally anomaly, resulting in similar capability to capture the tropical expansion and ENSO events; 2) the developed OLR algorithm framework can generate reliable OLR estimates from multi-spectral remotely sensed data including Moderate Resolution Imaging Spectroradiometer (MODIS) and Advanced Very High Resolution Radiometer (AVHRR); 3) OLR has a potential to predict ENSO events through traditional statistical approach and machine

learning methods, and it has slight advantage over the sea-surface-temperature (SST) as a metric for this purpose. The developed high resolution AVHRR OLR performs better than High-Resolution Infrared Radiation Sounder (HIRS) and NOAA interpolated AVHRR OLR in predicting ENSO. In addition, the singularities in OLR spatial anomalies around the giant earthquake epicenter starting three days prior to the earthquake days also suggests the OLR as an effective precursor of such an event, and the developed AVHRR OLR showed much stronger sensitivity to the coming earthquake than the existing NOAA interpolated AVHRR OLR, suggesting that the former one as a better indicator for the earthquake prediction.

In this dissertation, the in-depth inter-comparisons among various OLR datasets will contribute as a reference for peers in the climate community who use OLR as one of inputs in their climate models or other diagnostic purpose. The developed OLR algorithm framework could be utilized to estimate OLR from future multi-spectral satellite data. This study also demonstrates that OLR is a promising indicator to predict ENSO and testifies that it is a precursor of giant earthquakes, which has implications for decision making aimed at alleviating the impacts on life and property from these extreme climate variations through some preventive measures such as releasing weather alert and conducting evacuations.

OUTGOING LONGWAVE RADIATION AT THE TOP OF ATMOSPHERE: ALGORITHM DEVELOPMENT, COMPREHENSIVE EVALUATIONS, AND CASE STUDIES

by

Yuan Zhou

Dissertation submitted to the Faculty of the Graduate School of the
University of Maryland, College Park, in partial fulfillment
of the requirements for the degree of
Doctor of Philosophy
2019

Advisory Committee:

Dr. Shunlin Liang, Chair

Dr. Tatiana V. Loboda

Dr. Yunyue Yu

Dr. Dongdong Wang

Dr. Ning Zeng

Dedication

To my parents, my wife, and my baby

Acknowledgements

I would first thank my advisor, Dr. Shunlin Liang, for all his guidance and support on both academic and life scopes. The most important things he brings to me are the ways of thinking in the process of scientific research, which greatly broaden my eyes and inspired me with new ideas. I really appreciate the help and encouragement he gave to me to overcome those big challenges and difficulties during the past six years. I also would like to express my appreciation to all my committee members, Dr. Tatiana Loboda, Dr. Yunyue Yu, Dr. Dongdong Wang, and Dr. Ning Zeng, for their patient help and constructive comments on my dissertation. I would also express special thanks to the advisor of my Master program, Dr. Jin Chen, for his continuous help during my Ph.D program.

In addition, I would also like to thank all my friends and colleagues in our research group, including Dr. Tao He, Yuhan Rao, Yi Zhang, Dr. Yunfeng Cao, Dr. Zhenzhen Jia, Dr. Xin Tao, Dr. Xiaona Chen, Dr. Zhen Song, Dr. Jingjing Peng, and Meredith G. L. Brown, for their instructive discussions and selfless help. Finally, I am grateful for the endless love and support from my parents and my wife.

I would also like to thank the National Oceanic and Atmospheric Administration for their financial support.

Table of Contents

List of Tables

List of Figures

Chapter 1 Introduction

1.1 Background

Earth's climate is determined by the fluxes of energy radiated into and emitted from the planet (Stephens et al., 2012). Long-term studies on the Earth's energy budget play an important role in understanding the climate of our planet, detecting and investigating the impact of human activity on the climate change and other accompanying global changes (Loukachine and Loeb, 2004). In a balanced climate state, the net radiation at the top-of-atmosphere (TOA) should be close to zero (Hansen et al., 2005; Loeb et al., 2009) (Figure 1-1). However, by interacting with clouds, aerosols, and land surfaces, incoming solar radiative energy is transformed into other types of energy such as sensible and latent heat before being emitted back to space as longwave infrared energy (Trenberth and Fasullo, 2012). Positive imbalance between the absorbed and emitted energy exists, and such imbalance results in rising temperature and increased ocean heat content. (Hansen et al., 2005; Loeb et al., 2009), which have direct impact on global warming. The net radiation (R_n) of the whole planet at TOA is defined as the difference between the absorbed incoming solar radiation (ASR) and emitted outgoing longwave radiation (OLR) (Equation 1-1).

$$R_n = ASR - OLR$$

Equation 1-1

Where *ASR* is calculated as the difference between the downward solar radiation (*DSR*) and the upward shortwave radiation (*USR*) at TOA (*ASR* = *DSR* - *USR*).

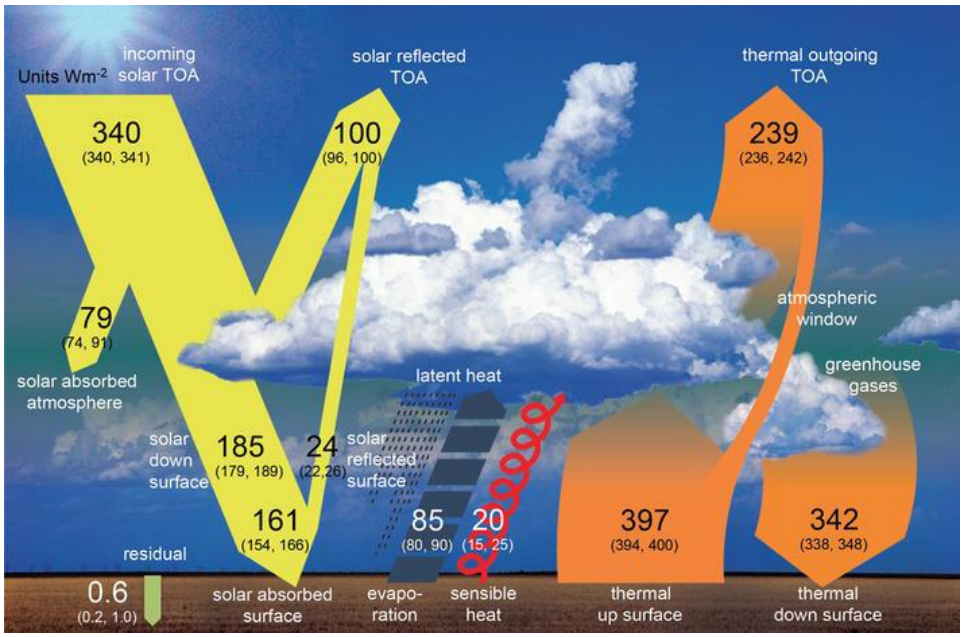

Figure 1-1 Schematic diagram of the annual mean radiation and energy fluxes of the Earth (W m^{-2}) with estimated uncertainty ranges in parentheses from Wild et al. (2013).

From Figure 1-1 and Equation 1-1, OLR (4~100μm) is one of the critical components in the Earth's radiation budget (ERB). It plays a role as a powerful diagnostic of Earth's climate system response to ASR (Comer et al., 2007). In some specific times or regions (i.e., at night or in polar areas) where ASR is negligible, OLR determines the ERB by dominating the TOA net radiation (Kim et al., 2018). As one of the energy fluxes, OLR is a composition of radiative intensities at different spectral wavelength and from different observation directions (Huang et al., 2008). It is thus determined by various atmospheric and surface conditions like surface temperature and emissivity, atmospheric temperature and humidity profiles, and clouds and aerosols, etc. (Huang et al., 2008). Owing to these meaningful properties, OLR is considered particularly critical for the cloud-radiation interaction because clouds can play as a greenhouse ingredient to warm the Earth by increasing the OLR (Inoue and Ackerman, 2002) and is used for the development or improvement of a parameterization model for surface-atmosphere relations (Morel, 1985).

It is used as a key factor in the investigation of the changes in cloud distribution (Cho et al., 2012; Choi and Ho, 2006; Huang et al., 2014; Lau et al., 1996; Lindzen and Choi, 2011; Wang et al., 2002), precipitation (Singh et al., 2014; Xie and Arkin, 1998; Yuanjing et al., 2015), and ecosystems (Bass et al., 1998). Previous studies (Hu and Fu, 2007; Hu et al., 2011; Johanson and Fu, 2009; Lucas et al., 2014; Seidel et al., 2008) also suggested that the tropical expansion can be well identified and monitored through Hadley circulation – a thermally driven meridional circulation. With respect to monitoring and implying climate change and climate anomalies, Harries et al (2001) studied the changes of the Earth's greenhouse effect based on the OLR variation, which is considered to be a measure of how Earth cools and carries the imprint of gases that are responsible for the greenhouse effect. Chandra et al (1998) revealed the eastward shift of the tropical convective activity based on National Oceanic and Atmospheric Administration (NOAA) OLR data (Liebmann and Smith, 1996a) after the 1997–1998 El Niño and explained its impact on tropospheric column ozone and water vapor. Furthermore, OLR has been taken as one of the most important indicators capturing the El Niño/Southern Oscillation (ENSO), which is the dominant climate phenomenon inducing extreme weather conditions worldwide (Cai et al., 2015). Lau and Chan (1986; 1985) explored aspects of the 40–50 day oscillation using OLR during the northern winter and summer, respectively, and found that the oscillation is an important component of the intra-seasonal variability of tropical convection. Zelinka and Hartmann (2011) found two opposite effects of OLR during El Niño: the upward shift of tropical cloud fraction profiles increases OLR, while a reduction in peak coverage lowers OLR. Su et al. (2017) investigated how daytime and nighttime OLR responds to sea surface temperature (SST) changes during the ENSO cycle, reporting that both daytime

and nighttime OLR over the tropics showed decreasing trends starting with El Niño and ending with La Niña, but daytime OLR decreased more rapidly than that of nighttime OLR. Trenberth et al. (2002; 2010; 2015) illustrated the relationship between the tropical SST and each of the TOA radiation components (ASR, OLR, and R_T) and their evolution with ENSO. Another important function of OLR is to play as a precursor of giant earthquakes which have magnitudes larger than 7; before the earthquake, the latent heat release increases the overall energy budget of the lower atmosphere which enhances the OLR flux, showing deviation from its normal values one day to one month prior to earthquakes (Ouzounov et al., 2007; Ouzounov et al., 2013; Pulinets and Ouzounov, 2011). For several recent giant earthquakes like those at China (M=7.9, 2008), Haiti (M=9.0, 2011), Chile (M=8.8, 2010) and Japan (M=9.0, 2011), strong OLR anomalies were observed 5–6 days prior to the earthquakes (Ouzounov et al., 2007; Pulinets and Ouzounov, 2011; Xiong et al., 2010).

In light of these implications, reliable observation or accurate estimation of OLR globally are essential. Remote sensing techniques provide a unique opportunity to obtain OLR data at a global scale. Since 1980s, observations of OLR have been conducted by various broadband sensors, including Earth Radiation Budget Experiment (ERBE) (Barkstrom, 1984), Scanner Radiometer for Radiation Budget (ScaRab) (Kandel et al., 1998), Geostationary Earth Radiation Budget (GERB) (Harries and Crommelynck, 1999), and Clouds and the Earth's Radiant Energy System (CERES) (Loeb et al., 2001; Wielicki et al., 1996). The CERES aboard *Terra* and *Aqua* satellites provides global observations of OLR within 4–100μm range by employing an angular distribution model (ADM) on the broadband thermal observations. With respect to narrowband radiometers, NOAA's

Climate Data Record (CDR) program generates daily OLR from High-Resolution Infrared Radiation Sounder (HIRS) (Lee and Ellingson, 2013; Lee et al., 2007) instruments on board the NOAA TIROS-N series and Eumetsat MetOp polar orbiting satellites and the Imager instruments on board operational geostationary satellites (Gehne et al., 2014). The algorithm originated from (Ellingson et al., 1989) who used narrowband radiance observations to estimate OLR through regression methods. This approach was also employed to produce OLR datasets for the Geostationary Operational Environmental Satellite (GOES) Sounder (Ba et al., 2003), GOES Imager (Lee et al., 2004), and upcoming GOES-R Advanced Baseline Imager (ABI) (Lee et al., 2010). In addition to satellite retrieved OLR, reanalysis datasets are also valuable resources of OLR, such as Japanese Reanalysis (JRA) series, ECMWF Interim Reanalysis (ERA-Interim), National Centers for Environmental Prediction (NCEP) series, Modern-Era Retrospective Analysis for Research and Applications (MERRA) among others. A reanalysis produces a dynamically consistent global analysis of the state of the atmosphere using a "frozen" model (Betts et al., 2006). It is a combination of modeling and measurements, using observations to constrain a dynamic model to achieve an optimal balance between complete coverage and accuracy. The inclusion of observations into models is known as data assimilation (Betts et al., 2006). Compared to satellite retrieval, reanalysis datasets possess the unique advantage of extended data availability, with no data gaps at either spatial or temporal scales, which significantly enhances data usability in long-term global climatic studies (Allan et al., 2004; Rienecker et al., 2011; Yanai and Tomita, 1998). Although providing much more comprehensive estimates, reanalysis data are constrained in obeying the conservation of mass, energy, water or momentum, which may decrease the reliability of

the data compared to the direct retrieval from satellite observations. Moreover, despite the use of a frozen model, there are significant changes with time in the observational data sets, especially during the last few decades in the satellite era (Betts et al., 2006).

Despite the multiple resources of OLR, their estimates could differ largely due to the sensor quality, model performance, and parameter calibration. Plus, direct validation of OLR datasets is far more challenging than that of surface parameters because no field measurement data are available at TOA level. Loeb's group (Loeb et al., 2009) performed inter-comparisons of gridded global monthly mean TOA flux from ERBE, Clouds and the Earth's Radiant Energy System (CERES), Global Energy and Water Cycle Experiment (GEWEX), and International Satellite Cloud Climatology Project (ISCCP), indicating that all-sky and clear-sky OLRs show a range of 4.6 W m^{-2} and 5.8 W m^{-2}, respectively. However, limited studies have followed to conduct comprehensive comparisons to evaluate the consistencies among various OLR datasets including both satellite retrieval and reanalysis data, especially for those after the year of 2000. In addition, there are still some potential resources remained to be explored to generate more robust and useful OLR datasets: Moderate Resolution Imaging Spectroradiometer (MODIS) has been a widely used multi-channel satellite data since 2000, yet no solid algorithms and operational products of OLR have been released; Advanced Very High Resolution Radiometer (AVHRR) is one of few resources that could facilitate a long-term study beyond 35 years, although spatial resolution of current AVHRR OLR products archived in NOAA (Liebmann and Smith, 1996b) is too coarse (2.5°) to meet the requirements of some medium/high resolution (down to 1 km) numerical weather prediction models (Christensen et al., 1998; Guan et al., 2000; Soci et al., 2006).

Since the significance of OLR stated above and according to the current states of studies in this parameter, this dissertation will address the following questions: 1) How large are the discrepancies in estimates from various OLR products and what are their spatial and temporal patterns? 2) How to generate more accurate and more useful OLR estimates from multi-spectral satellite observations? 3) How does OLR respond to extreme climate and geological events such as El Niño/Southern Oscillation (ENSO) and giant earthquakes, and does the newly developed OLR products have any advantage to predict such events?

1.2 Objectives

The overall objective of this study is to develop more reliable and more useful OLR products that have greater capability to characterize climate issues and better predict climate anomalies. In specific:

1) quantifying the inconsistencies and discrepancies among multiple existing OLR products by performing inter-comparisons among them;

2) developing an algorithm framework for estimating more reliable and more useful OLR from multi-spectral satellite observations based on radiative transfer simulation and statistical approaches;

3) investigating the correlation between OLR anomalies and historical ENSO events and giant earthquakes ($M > 7$) and tries to predict those events through OLR variations.

1.3 Dissertation structure

Chapter 1 introduces the background, objective, and overall structure of this dissertation.

Chapter 2 conducts comprehensive inter-comparisons among existing satellite retrieved OLR and reanalysis OLR datasets, respectively, to identify the inconsistencies and uncertainties of current OLR estimates. Both spatial and temporal patterns of OLR variations are compared and analyzed. In addition, the indication of OLR to typical climate events, including tropical expansion and ENSO, are presented and evaluated. According to those results, OLR datasets which have large differences with the reference data are reported.

Chapter 3 describes the algorithm developed for estimating OLR from multi-spectral satellite data. Extensive radiative transfer simulations, along with statistical approaches, are utilized in this study to establish the relationship between TOA spectral radiance and the broadband OLR under various surface and atmospheric conditions. MODIS and AVHRR data are then collected to demonstrate the effectiveness of the algorithm framework, and CERES OLR products are used to evaluate the OLR estimates from them.

Chapter 4 explores the capability of OLR to predict ENSO and a giant earthquake occurred in Nepal. Information of historical ENSO events since 1980s are collected for model construction and testing. Three methods, including extended empirical orthogonal function (EEOF), traditional statistical regression, and machine learning are employed to explore the potential of OLR as an indicator for ENSO prediction. As a reference, those three methods are also used to examine predictive capabilities of SST and the results are

compared with that of OLR. For earthquakes, an earthquake occurred in Nepal with magnitude (Richter Scale) of 7.3 are taken as a case study and the Eddy field calculation mean of OLR is employed to capture the spatial and temporal anomaly of OLR prior to the earthquakes.

Chapter 5 concludes the main findings and contributions of this dissertation. Future study perspectives are also discussed based on the results and limitations of current work.

Chapter 2 Inter-comparisons among existing OLR datasets from satellite retrieval and reanalysis data

Chapter 1 stressed the significance of OLR on various climate issues. Multiple OLR products have been developed in the past four decades including satellite retrievals and reanalysis data. Satellite products estimate OLR from satellite observations through ADM for broadband sensors (e.g., ERBE (Barkstrom et al., 1989), CERES (Loeb et al., 2001; Wielicki et al., 1996)) and statistical regression approaches for narrowband sensors (e.g., HIRS (Lee and Ellingson, 2013; Lee et al., 2007)), respectively. It is basically recognized as reliable resources of Earth parameters because it gains the information of Earth surface and atmosphere from the direct observation. Reanalysis is a method for characterizing how weather and climate are changing over time. In the reanalysis, observations and numerical models that simulates various aspects of the Earth system based on physical principals are combined to generate a synthesized estimate of the state of the system. It usually extends over several decades or longer and covers globally from the Earth's surface to above the stratosphere. Compared to satellite retrieval, reanalysis datasets have the unique advantage of longer data availability, with no gaps at either spatial or temporal scales, which significantly enhances data usability in long-term global climatic studies. However, reanalysis data are constrained in obeying various physical laws of the numerical models, which might have negative impacts on the accuracy of the data compared to the direct retrieval from satellite observations.

Despite the multiple resources of OLR, their estimates could differ largely due to the sensor quality, model performance, and parameter calibration. As a critical parameter to characterize Earth's energy budget and an important input to most of climate models, it

is necessary to quantify the magnitude of such inconsistencies and discrepancies in estimates from various OLR products and their spatial and temporal patterns. However, it is far more challenging to perform direct validation of OLR than that of surface parameters because no field measurement data are available at TOA. Therefore, this chapter will conduct a comprehensive evaluation of multiple OLR products through inter-comparisons among them. To facilitate the comparisons, CERES OLR products are selected as the reference data which are currently widely recognized as the most accurate TOA broadband flux retrievals. In addition, OLR products are also evaluated by examining the capability to capture climate anomalies including tropical expansion and ENSO. Results of this study will play as a reference for peers in the climate community who use OLR as one of inputs in their climate models or other diagnostic purpose. The two resources of OLR data, satellite retrieval and reanalysis data, will be evaluated separately.

2.1 Datasets

2.1.1 Satellite retrievals of OLR

In this study, five satellite OLR products derived from CERES, HIRS, GEWEX SRB, AIRS, and Satellite Application Facility on Climate Monitoring (CM SAF) from EUMETSAT are collected for inter-comparisons and evaluations. CERES is the representative of OLR retrieval from broadband sensors using ADM; HIRS and AIRS are those from narrowband sensors estimated from radiative transfer simulation and statistical regressions; while CM-SAF is a representative of the regional OLR products. Table 2-1 summarizes the data sources and characteristics.

Table 2-1 Details of the satellite retrieved OLR products and SST data used in this study

Data Source	Time Span	Spatial Resolution	Reference
CERES	2001-2016	1° × 1°	(Loeb et al., 2018)
HIRS	1979-2016	2.5°× 2.5°	(Lee et al., 2007)
GEWEX SRB	1983-2007	1° × 1°	(Stackhouse et al., 2011)
AIRS	2002-2016	1° × 1°	(Sun et al., 2010)
CM SAF	2004-2016	0.1° × 0.1°	(Schulz et al., 2009)

2.1.1.1 CERES EBAF-TOA OLR product

The CERES products have been widely recognized as the most accurate TOA broadband flux retrievals. They are designed to provide precise global cloud, aerosol, and TOA radiation data products to facilitate research addressing the role of clouds and aerosols in modulating the radiative energy flow within the Earth–atmosphere system (Wielicki et al., 1996; Wielicki et al., 1995). The two CERES instruments onboard *Terra* (FM-1 and FM-2) and *Aqua* (FM-3 and FM-4), respectively, provide highly accurate radiance measurements in shortwave channel (SW, 0.3 to 5 μm), total channel (TOT, 0.3 to 200 μm), and infrared window channel (WN, 8 to 12 μm), globally at a 20 km spatial resolution at nadir (Loeb et al., 2003a). Due to the nature of OLR, it is difficult to establish in-*situ* measurements at TOA as scientists can do at the land surface. In this situation, the CERES OLR products are taken as the reference data for validating and evaluating other satellite-retrieved OLR products as its widely recognized data reliability. The newest edition of CERES OLR, Energy Balanced and Filled (EBAF) TOA flux products, conducts adjustment to both TOA shortwave flux and OLR to ensure that global mean net TOA flux for July 2005–June 2015 is consistent with the in situ value of 0.71 W/m^2 (Loeb et al., 2018). In this chapter, monthly OLR data from the CERES-EBAF is used as the reference OLR.

2.1.1.2 HIRS OLR product

CERES OLR products are generally accepted and the gold standard OLR measurement, however, they are available only from 2000, making it insufficient for the purpose of long-term assessments. Fortunately, the NOAA CDR program provides a long-term record of daily global OLR (1979 to present) derived from the HIRS instruments. The product provides 1° × 1° daily mean OLR retrieved by multispectral regression models originally proposed by Ellingson et al., (1989). Validations of the HIRS OLR data against the broadband-based OLR products derived from ERBE and CERES scanners/non-scanners observations were shown to have very consistent agreement in terms of accuracy, variability, and stability (Lee and Ellingson, 2013; Lee et al., 2007). In this study, monthly mean HIRS OLR with the resolution of 2.5° × 2.5° from 1979 to 2016 were collected from NOAA NCDC.

2.1.1.3 AIRS OLR estimate

AIRS is a hyperspectral grating spectrometer onboard on National Aeronautics and Space Administration (NASA) Earth Observing System (EOS) Aqua platform. It measures thermal infrared radiances with 2378 spectral channels covering the spectral range of 3.74-4.61, 6.20-8.22, and 8.8-15.4μm (Aumann et al., 2003; Chahine et al., 2006). Taking the advantage that AIRS radiance measurements include more information content about atmospheric state and surface and cloud properties than those of narrowband sounders, Sun et al., (2010) derived OLR directly from high-quality AIRS radiances. A technique for PC regression (Goldberg et al., 2003) was used to derive equations for estimating AIRS OLR by least squares regression of CERES OLR with the principal component scores (PCSs) of

the AIRS radiance measurements. In this study, AIRS monthly OLR with the resolution of 1° × 1° from 2002-2016 were collected from NASA Goddard Earth Sciences Data Information and Services Center (GESDISC).

2.1.1.4 CM-SAF OLR product

The European Organization for the Exploitation of Meteorological Satellites (EUMETSAT) Satellite Application Facility on Climate Monitoring (CM-SAF) program provides satellite derived geophysical parameter datasets suitable for climate monitoring (Schulz et al., 2009). Cloud parameters, surface albedo, surface and TOA radiation fluxes, as well as atmospheric temperature and humidity products are routinely produced as a sound basis for climate monitoring of the atmosphere (Schulz et al., 2009). CM-SAF OLR product is derived from the Global Earth Radiation Budget (GERB) (Harries et al., 2005) on board the METEOSAT Second Generation (MSG) geostationary satellites using a RT model stemmed from theoretical considerations of (Clerbaux et al., 2003). In this study, monthly mean OLR data at a spatial resolution of 0.1° × 0.1° covering the Meteosat disc area were collected from the website of EUMETSAT CM-SAF.

2.1.2 Reanalysis OLR

The National Centers for Environmental Prediction (NCEP), the European Center for Medium-Range Weather Forecasts (ECMWF), the NASA Goddard Space Flight Center (GSFC)'s Global Modeling and Assimilation Office (GMAO), and the Japan Meteorological Agency (JMA) are the four representative organizations that produce "second generation" reanalysis datasets (Zhang et al., 2016). These datasets have been broadly used in various fields to monitor long-term climatic trends (Lohmann et al., 2006),

simulate the radiation budget for weather forecasts (Allan et al., 2004), and estimate precipitation (Rienecker et al., 2011). In this study, seven reanalysis OLR products were selected from these databases, and the data sources and characteristics of them are summarized in Table 2-2.

Table 2-2 Details of the reanalysis OLR products used in this study

Data Source	Time Span	Original Temporal Resolution	Spatial Resolution	Reference
JRA-25	1979-2007	3h	G 0.56° × 0.56°	(Onogi et al., 2007)
JRA-55	1958-2013	3h	G 0.56° × 0.56°	(Kobayashi et al., 2015)
ERA-Interim	1979-2012	3h	0.75° × 0.75°	(Dee et al., 2011)
MERRA	1979-2015	3h	0.5° × 0.667°	(Rienecker et al., 2011)
NCEP-NCAR	1948-2016	6h	G 1.9° × 1.9°	(Kalnay et al., 1996)
NCEP-DOE	1979-2016	6h	G 1.9° × 1.9°	(Kanamitsu et al., 2002)
NCEP-CFSR	1979-2016	6h	G 0.3° × 0.3°	(Saha et al., 2010)

***G: Gaussian grid**

2.1.2.1 JRA-25 and JRA-55

The JMA conducted a long-term (from 1979 to 2004) global atmospheric reanalysis project named "Japanese 25-year Reanalysis (JRA-25)," the first long-term reanalysis undertaken in Asia (Onogi et al., 2007). The project used JMA's traditional numerical assimilation system, the three-dimensional variational method (3D-Var), and specially collected observational data to generate a consistent and high-quality reanalysis dataset (Onogi et al., 2007). The OLR was calculated using a broadband flux emissivity method for four thermal spectral bands (Sugi, 1990).

As the successor to JRA-25, JRA-55 was the second generation of global atmospheric reanalysis project conducted by the JMA. This project covered 55 years from

1958 to 2013, coinciding with the establishment of the global radiosonde observation system. JRA-55 mainly aimed to address issues found in previous reanalyses and to produce comprehensive atmospheric datasets suitable for the study of multidecadal variability and climate change (Kobayashi et al., 2015). Compared to JRA-25, JRA-55 improved many deficiencies in its predecessor by using a higher spatial resolution, employing the TL319 version of the assimilation system, adding newly available and improved past observations, and introducing greenhouse gases with varying concentrations over time (Kobayashi et al., 2015; Zhang et al., 2016). With respect to longwave flux, JRA-55 adjusted the longwave radiation scheme by increasing the number of thermal spectral bands from four to nine. In addition, the basic framework for computing band-averaged transmission functions was replaced with the method of Chou et al. (2001); absorptions due to Doppler broadening were more properly presented, and absorbing gases considered in the forecast model were enriched (Kobayashi et al., 2015).

2.1.2.2 ERA-Interim

ECMWF Interim Reanalysis (ERA-Interim) is a global atmospheric reanalysis produced by the ECMWF, which covers from 1979 to the present day and extending forward in near-real time. Compared to ERA-40, ERA-Interim employs an updated version of the ECMWF forecasting model (Cy31r2) for data assimilation (Dee et al., 2011), and a four-dimensional variational analysis (4D-Var), a temporal extension of the previous 3D-Var (Saha et al., 2010), has been adopted. During data assimilation, the difference between the model and the observation within a 12-hour assimilation window was minimized (Dee et al., 2011; Zhang et al., 2016). The spatial resolution of the data set is 0.75°

(approximately 80 km) on 60 vertical levels from the surface up to 0.1 hPa. Radiation was calculated based on the Rapid Radiation Transfer Model (RRTM) (Mlawer et al., 1997).

2.1.2.3 MERRA

Modern-Era Retrospective Analysis for Research and Applications (MERRA) reanalysis undertaken by NASA's GSFC mainly aimed to place observations from NASA's EOS satellites into a climatic context and to improve upon the hydrologic cycle represented in earlier generations of reanalyses (Rienecker et al., 2011). MERRA reanalysis covers from 1979 to the present, using an updated new version of the Goddard Earth Observing System Data Assimilation System Version 5 (GEOS-5). GEOS-5 used uses an incremental analysis update (IAU) procedure (Bloom et al., 1996) in which analysis correction was applied to the forecast model gradually, through an additional tendency term in the model equations during the corrector segment (Rienecker et al., 2011). MERRA achieves significant advances in the representation of the water cycle by using a catchment-based hydrological land surface model (Rienecker et al., 2011; Zhang et al., 2016). Longwave flux was calculated based on the longwave radiation scheme proposed by Chou et al. (2001).

2.1.2.4 NCEP-NCAR

The NCEP-NCAR reanalysis was conducted to produce a retroactive record of more than 50 years (from 1948 to present) of global analyses of atmospheric fields in support of the needs of the research and climatic monitoring communities (Kistler et al., 2001). Data from land surface, ship, rawinsonde, pibal, aircraft, and satellite were assimilated into the T62/28-level NCEP global spectral model (Kalnay et al., 1996) using

a 3-Dimensional variational (3D-Var) scheme cast in spectral space denoted spectral statistical interpolation (Parrish and Derber, 1992).

2.1.2.5 NCEP-DOE

The NCEP-DOE reanalysis project was conducted to provide an improved version of the NCEP-NCAR reanalysis datasets by correcting human-processing errors (e.g., Southern Hemisphere bogus data, humidity diffusion, oceanic albedo) and incorporating upgrades to the forecast model and a diagnostic package (Kanamitsu et al., 2002). Compared to NCEP-NCAR, the NCEP-DOE was the "second generation" reanalysis and provided more emphasis on data accuracy, resolution, and long-term trends using an improved assimilation mode based on 4D-Var. The resolution of the NCEP-DOE model is the same as that in the NCEP-NCAR, T62 Gaussian grids (1.9° × 1.9°) with 28 vertical sigma levels. Longwave radiation was also refined by employing more realistic cloud-top cooling parameters, updating cloud-tuning coefficients for stratus clouds using preproduction, performing a radiation calculation on the full Gaussian grid, and running radiation code at a higher temporal frequency (Kanamitsu et al., 2002).

2.1.2.6 NCEP-CFSR

The NCEP-CFSR reanalysis is the newest reanalysis dataset from NCEP covering from 1979 to the present. The atmospheric model was upgraded to a T382/64-level from the T62/28-level of the original NCAR (Saha et al., 2010). With regard to longwave radiation, a new Rapid Radiation Transfer Model for Global Models – Longwave (RRTMG-LW) was adopted adapted from the RRTM developed by Atmospheric and Environmental Research (AER) (Mlawer et al., 1997). It employed a computationally

efficient correlated-k method for radiative transfer calculations, and major radiatively absorbing gases (water vapor, ozone, and CO2) and many other radiatively active greenhouse gases are included in the model (Saha et al., 2010).

2.1.3 SST

SST has been widely used in defining ENSO events (Trenberth, 1997a). In this study, data from Extended Reconstructed Sea Surface Temperature (ERSST) Version 4 (v4) was collected to construct an SST-based Niño index. The ERSST dataset is a global monthly SST analysis on a 2° × 2° grid derived from the International Comprehensive Ocean-Atmosphere Dataset (ICOADS). The latest ERSST, v4, has major improvements, based on Version 3b (v3b), in the aspects of input data, Empirical Orthogonal Teleconnections (EOTs) and EOT acceptance criterion, SST quality control procedures, SST anomaly (SSTA) evaluation methods, etc. (Huang et al., 2015). ERSST v4 is generated using in-situ SST data and improved statistical methods that allow stable reconstruction. The monthly analysis extends from January 1854 to the present and is updated monthly (Huang et al., 2015). Associated with ENSO, three-month running average SST anomalies (1981–2010 base period) were also collected from NOAA National Weather Service (NWS) CPC (http://www.cpc.ncep.noaa.gov/data/indices/).

2.2 Methodology

2.2.1 Data pre-processing

According to the data availability of all reanalysis datasets, the investigated time span in this study was approximately 37 years covering from 1979 to 2016. To conduct

inter-comparisons among different products, it is necessary to initially match their spatial resolution. In detail, the reanalysis datasets with Gaussian-grid projection were first converted to a latitude-longitude projection of similar spatial resolution. Then, spatial resolutions of all datasets were unified to 1° by upscaling or downscaling using the nearest-neighbor method. For satellite retrievals, all products were up-scaled to 2.5°× 2.5° to match the coarsest resolution data, HIRS.

2.2.2 Inter-comparisons

In order to explore both the spatial and temporal distribution and changing trends, both long-term mean climatological OLR and a long-term series OLR were calculated for the evaluation. The former calculated multi-year mean OLR climatological records globally for the DJF (December, January, February) and JJA (June, July, August), respectively; the latter calculated the global or regional averaged OLR for each month over multiple years and the OLR time-series were compared and analyzed.

2.2.3 Evaluation of OLR with tropical expansion

Previous studies (Hu and Fu, 2007; Hu et al., 2011; Johanson and Fu, 2009; Lucas et al., 2014; Seidel et al., 2008) suggested that the tropical expansion can be well identified and monitored through Hadley circulation – a thermally driven meridional circulation. Due to the release of latent heat, warmer tropical air rises and flows poleward in both hemispheres. When it comes to the subtropics, air then cools, sinks and flows back to the tropics, generating an enclosed circulation in each hemisphere (Hu and Fu, 2007) (see the right part in Figure 2-1). Hadley circulation is considered one of important standards to identify the boundary of tropical and extratropical regimes, which are a fundamental

distinction of the Earth's climate. In concept, the downward branch of this circulation can be treated as the "edge of the tropics" (Lucas et al., 2014). Since OLR contains integrated information about surface temperature and atmospheric conditions, it has been proven as one of most effective indicators for identifying the boundary of Hadley circulation and characterizing the changing of the tropical belt width thereby (Hu and Fu, 2007; Hu et al., 2011; Johanson and Fu, 2009). In detail, the zonal-mean climatological OLR displays peaks in the subtropics in both hemispheres; the high values of OLR in the subtropics is because of the dryness and lack of clouds caused by subtropical descending motion associated with the subsidence branch of the Hadley circulation. Therefore, the subsidence branch of the Hadley circulation can be identified as the region with high OLR in the subtropics. Existing research took the most poleward latitudes where the zonal-mean OLR equals 250 W/m^2 as the locations of the poleward edges of the Hadley circulation, and all of them reported robust evidence of tropical belt expansion (Hu and Fu, 2007; Hu et al., 2011; Johanson and Fu, 2009). Based on this theory, this study tested whether those OLR products can identify the tropical expansion: the time evolution of zonal-mean OLR is first depicted (Figure 2-2a) and the changing trend of the 250 W/m^2 contour can be quantified with statistical significance test (Figure 2-2b). With that, the global tropical expansion can be obtained, and comparisons of such expansions are performed among various OLR products.

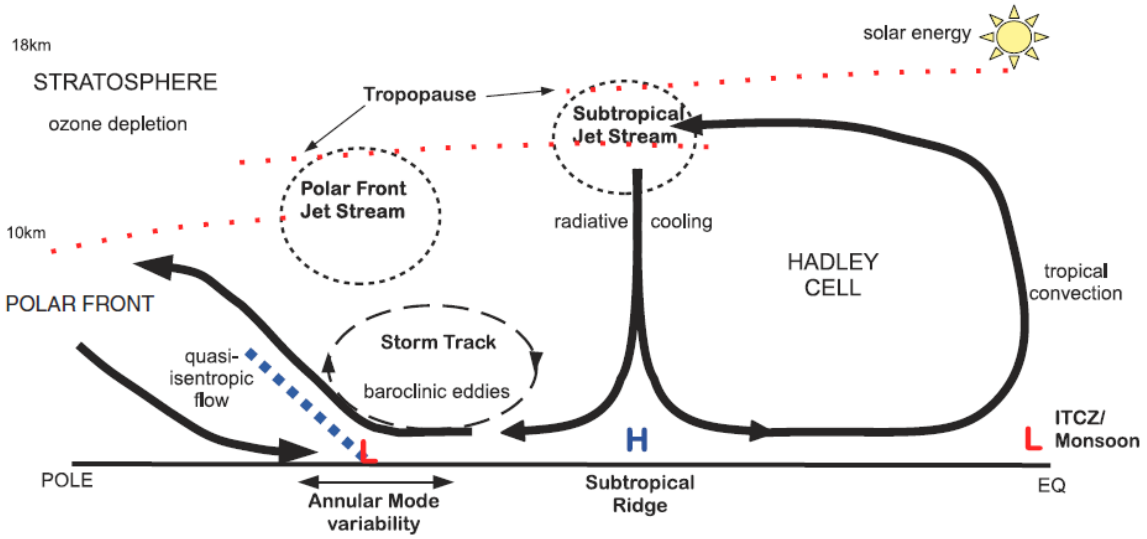

Figure 2-1 Schematic diagram detailing the components and physical processes of the idealized mean meridional circulation (MMC) (Lucas et al., 2014)

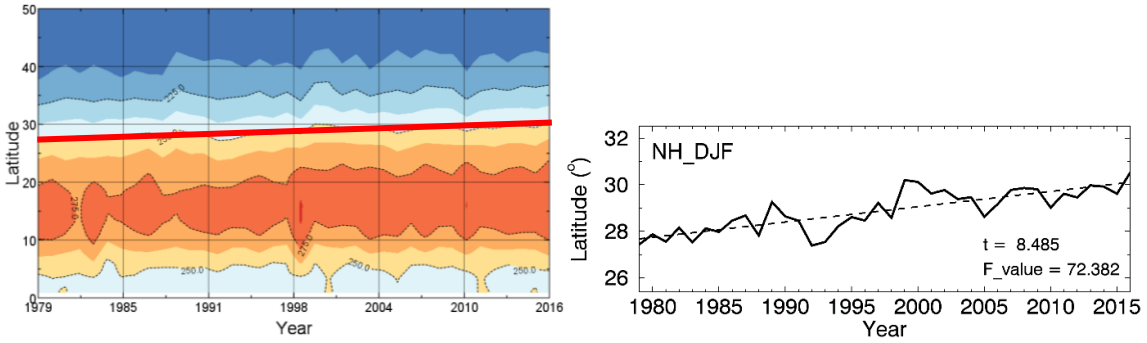

Figure 2-2 a) Time evolution of NH zonal-mean seasonal OLR (W/m^2) from HIRS covering the period from 1979 to 2016 for the DJF season. The 250 W/m^2 OLR contour is marked with the red bold line. b) Time series of the poleward latitudes at which the seasonal and zonal mean OLR is equal to 250 W/m^2 according to panel a).

2.2.4 Evaluation of OLR with ENSO

ENSO is the dominant mode of global climate variations. It results in strong anomalies in the radiation energy budget of the atmosphere-ocean system in tropical Pacific region and even over globe. (Mayer et al., 2016). Since OLR contains the integrated information of surface and atmosphere thermal conditions, anomalies in SST and in cloud properties are often reflected in anomalies in OLR. During ENSO, the tropical SST changes drastically and OLR responds strongly (Loeb et al., 2012; Su et al., 2017; Wong et al., 2006;

Zelinka and Hartmann, 2011). In this study, all OLR products are assessed regarding their capabilities of capturing ENSO cycles. Figure 2-3 shows the four representative Niño regions that have been widely used to investigate ENSO and its relations to SST, OLR, and sea surface level among other factors (Trenberth, 1997a). Niño 1 and Niño 2 (0°–10°S, 80°–90°W) represent the South American coastal SST where ENSO has substantial economic impacts (SCOR, 1983; Zopf et al., 1978). Niño 3 (5°N–5°S, 90°–150°W) and Niño 4 (5°N–5°S, 160°E–150°W) are larger regions in the eastern and central equatorial Pacific, respectively. In Niño 3, the model prediction and field observation achieve the highest consistency regarding ENSO-related parameters (Bamston et al., 1997; Trenberth, 1997b). Niño 3.4 (5°N–5°S, 120°–170°W) was proposed by the NOAA's NCEP CPC (Bamston et al., 1997) to account for the westward extension of the coupled atmospheric–ocean interactions in ENSO compared to that of Niño 3. Currently, an El Niño is characterized typically by five consecutive three-month running mean SST anomalies, known as the ONI, in the Niño 3.4 region above a threshold of +0.5°C. For La Niña, the best choice for determining its occurrence is the Niño 4 region rather than Niño 3.4, but the ONI is still effective and the threshold (< -0.5°C) also applies. Accordingly, this study examined if the inter-annual variations of the satellite-retrieved monthly OLRs can closely respond to El Niño and La Niña events over the Niño 3.4 and Niño 4 regions, respectively. Following the design of ONI, the three-month running mean of OLR anomalies were calculated using 1981–2010 as the base period. Hereinafter, the SST-based ONI is denoted as ONI_{SST} while the OLR-based index is denoted as ONI_{OLR} in the following discussion. With that, three analysis are conducted: 1) the spatial pattern of OLR anomaly over the central Pacific region during ENSO are visually examined and compared; 2) the correlation

of ONI_{OLR} and ONI_{SST} is investigated; and 3) the difference in the capability of OLR to capture El Niño and La Niña are manifested.

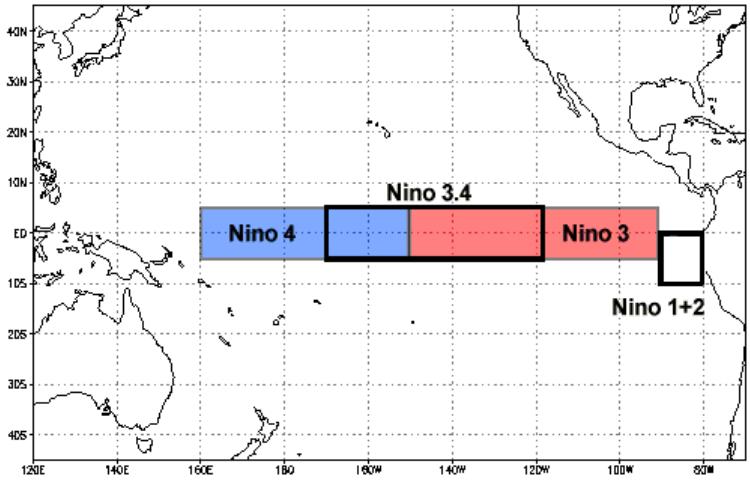

Figure 2-3 Locations of the five representative Niño regions in the equatorial Pacific Ocean. (Source: https://www.ncdc.noaa.gov/teleconnections/enso/indicators/sst.php)

2.3 Results and analysis

2.3.1 Satellite OLR retrievals

2.3.1.1 OLR climatology

Multi-year mean OLR values reflect the mean states of the Earth's emitted radiation to space at a long-term scale, which plays as the foundation of investigation of the OLR anomaly that usually indicates extreme climate events such as El Niño. Thus, OLR climatology comparisons are conducted in this study. In order to follow potential seasonal variations, seasonal OLR climatologies for the DJF and JJA are calculated respectively. As the reference data, Figure 2-4a and Figure 2-5a present the seasonal OLR climatologies of CERES-SYN1Deg for a 16-year period (2001–2016). CERES OLR values display obvious latitude-dependent distributions owing to the surface and atmospheric temperature, and the

northern hemisphere (NH) emits much more longwave radiation during the JJA than it does during the DJF. At the same latitude, OLR varies with surface type and altitude, as seen comparing the Amazon Forest and Middle Africa in Figure 2-4a, and the Sahara Desert and Tibetan Plateau in Figure 2-5a. Maps of OLR differences among the other five OLR products and those of CERES are also plotted accordingly (Figure 2-4b–f and Figure 2-5b–f). Statistics of the three metrics (correlation coefficient (R), bias, and root-mean-squared-deviation (RMSD)) are reported in Table 2-3. In general, all the five examined OLR products have high agreement (>0.94) with CERES product, suggesting no significant discrepancies exit among those products. From the bias maps, it is can be seen that, for each product, the magnitude and distribution of OLR difference against CERES don't have obvious seasonal variations, while the difference maps among those products differ with each other in both seasons. In detail, HIRS data shows obvious surface-based variation, with negative bias presented on vegetated and snow/ice covered surfaces (e.g., Amazon Forest, Greenland, and Antarctica) and positive bias presented on desert (e.g., Sahara Desert) and most parts of oceans. Although these two sides of differences neutralize the overall biases which are quite small (-0.11 W/m^2 for DJF and 1.86 W/m^2 for JJA), the RMSDs are much larger (4.21 W/m^2 for DJF and 3.01 W/m^2 for JJA). GEWEX-SRB display a relatively complicated spatial pattern, but there is also a trend indicating that positive bias is more pronounced in low-latitude areas while negative bias is more pronounced in high-latitude areas. AIRS presents nearly global positive bias expect very slight negative bias in the two polar regions, leading to the overall biases as 3.00 W/m^2 and 3.45 W/m^2 for DJF and JJA, respectively. In contrast, negative biases dominate the CM-SAF, the regional OLR product, over its entire observing region with -4.44 W/m^2 and -

4.47 W/m^2 for DJF and JJA, respectively. In summary, all five examined OLR products agree well with CERES in general (absolute bias < 5 W/m^2, see in Table 2-3). Further considering the RMSDs, HIRS performs best, suggesting that almost no spatial variations are found against CERES.

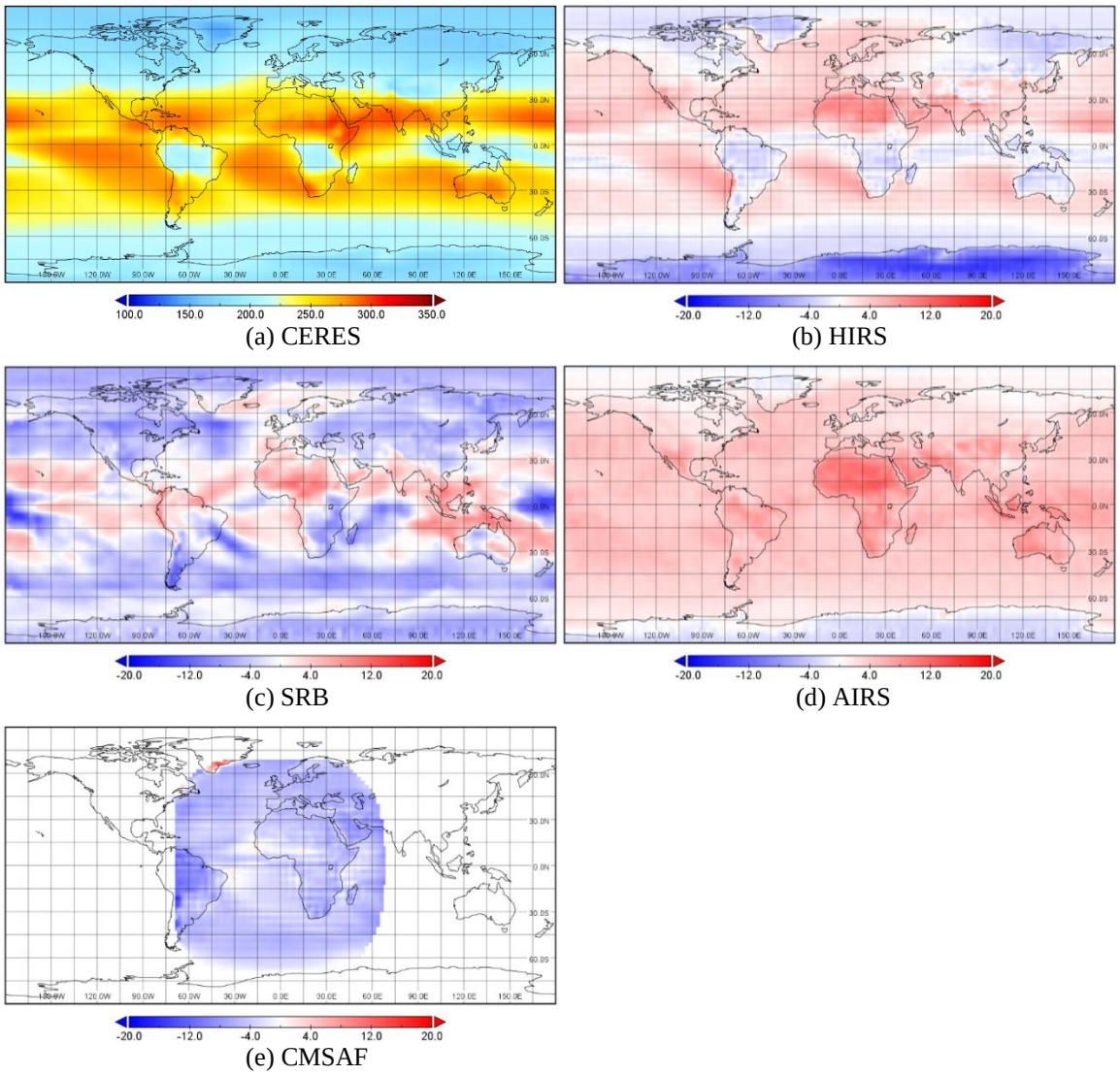

(a) CERES (b) HIRS

(c) SRB (d) AIRS

(e) CMSAF

Figure 2-4 CERES EBAF OLR monthly climatology for DJF and the biases between other OLR products and CERES OLR from 2000 to 2016: a) CERES monthly OLR for DJF; b) HIRS minus CERES; c) SRB minus CERES; d) AIRS minus CERES; e) CMSAF minus CERES.

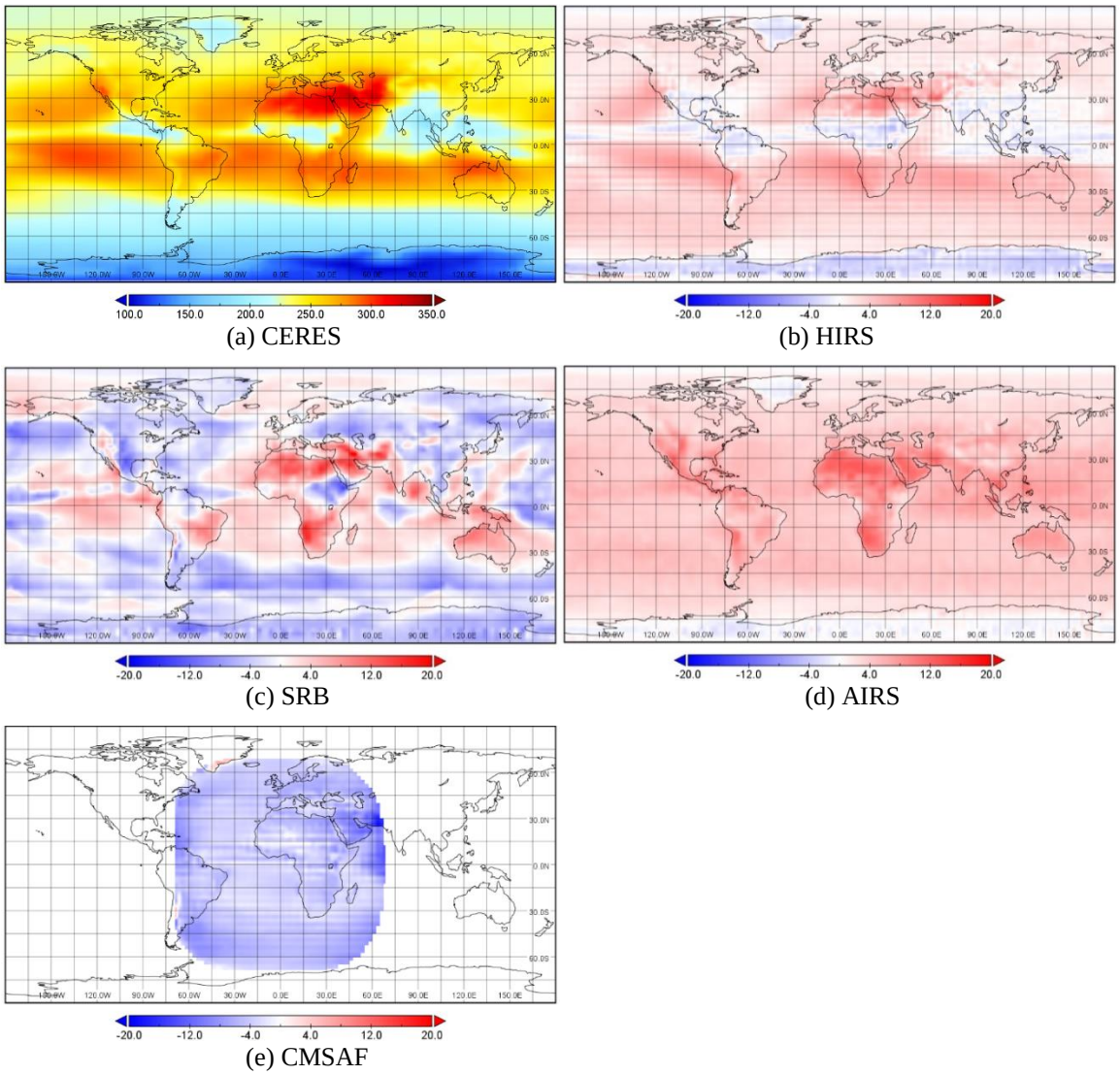

(a) CERES (b) HIRS

(c) SRB (d) AIRS

(e) CMSAF

Figure 2-5 CERES EBAF monthly OLR climatology for JJA and the biases between other OLR products and CERES OLR from 2000 to 2016: a) CERES monthly OLR for DJF; b) HIRS minus CERES; c) SRB minus CERES; d) AIRS minus CERES; e) CMSAF minus CERES.

Table 2-3 Statistics of the comparison between five OLR products against CERES OLR using the monthly mean climatology during DJF and JJA, respectively

Satellite OLR products	R^2		Bias (W/m^2)		RMSD (W/m^2)	
	DJF	JJA	DJF	JJA	DJF	JJA
HIRS	0.94	0.96	-0.11	1.86	4.21	3.01
SRB	0.94	0.98	-2.35	-0.81	4.65	3.25
AIRS	0.96	0.96	3.00	3.45	3.77	4.12
CMSAF	0.94	0.94	-4.44	-4.47	4.88	5.17

Furthermore, Table 2-4 reports the OLR biases between CERES and the five examined products across different surface types. The first apparent conclusion is that, for all examined OLR products, the biases over oceans show almost no variation across seasons, while most of them display much larger seasonal differences over lands. Looking into sub-categories of lands, no significant seasonal variation is observed over vegetated and desert surface either. However, large difference is found on snow/ice surface. Considering that the Greenland and Antarctica are the two primary places where the permanent snow/ice presents, such a difference is attributed to the apparent difference of OLR values over the two lands which is dominated by the surface temperature. These trends are observed for all global OLR products (i.e., HIRS, GEWEX-SRB, and AIRS) especially for HIRS which results in bias of -8.96 W/m^2 against CERES in DJF but only -1.93 W/m^2 in JJA. For AIRS which is the only one with higher estimates than those of CERES overall, the positive biases over desert land are as high as 8 W/m^2 and around 4 W/m^2 over vegetated surfaces. CM-SAF, the regional product, shows very slight spatial and seasonal variations of the biases against CERES, with 4~5 W/m^2 over all types of surface in both winter and summer seasons.

Table 2-4 Biases between the five OLR products against CERES OLR over different surface types during DJF and JJA, respectively. Unit: W/m^2.

Satellite OLR products		Vegetation	Desert/Barren land	Snow/Ice	Land Overall	Ocean
HIRS	DJF	-0.71	5.56	-8.96	-2.95	-0.51
	JJA	1.92	4.84	-1.93	0.35	0.60
GEWEX-SRB	DJF	-3.40	1.09	-4.64	-3.43	-3.59
	JJA	-0.93	6.12	-4.22	-1.43	-2.45
AIRS	DJF	3.14	7.73	-1.68	1.91	1.80
	JJA	3.98	8.52	-0.29	3.02	1.90
CM-SAF	DJF	-4.69	-3.86		-4.28	-4.41

	JJA	-4.23	-5.04	-4.91	-4.23

2.3.1.2 OLR time series comparison

Comparisons of OLR climatologies (section 2.3.1.1) are manifested in the state of multi-year mean OLR and its global spatial pattern. To recover OLR inter-annual variation and investigate the anomaly periods, long-term time-series comparisons were also conducted. For each month since the start of the satellite era (1979), the equal-area spatially-averaged monthly OLR was calculated using the latitudinal-weighted method, and the generated OLR time-serial curves of all the examined OLR products and CERES were plotted (see in Figure 2-6a and Figure 2-7a). Because of different spatial coverage, Figure 2-6 excludes CM-SAF and global-averaged values are shown, while Figure 2-7 includes all products and the displayed values are averaged over the CM-SAF covered regions. Taking CERES as the reference data, the time-series of OLR differences are also plotted in Figure 2-6b and Figure 2-7b, respectively. HIRS OLR is slightly larger than CERES with obvious seasonal cycles, and the peaks and valleys of its bias curve are consistent with CERES OLR values, suggesting that large biases comes with large OLR estimates, and vice versa. In contrast, GEWEX-SRB OLR is slightly lower than CERES with seasonal variations as well. AIRS and CM-SAF have similar magnitude of difference against CERES (~ 5 W/m^2) while the former one overestimates and the latter underestimates. Seasonal variations are much less notable and somewhat irregular for these two products. After removing the seasonal cycle, the correlation coefficients between CERES OLR and those examined products were recalculated and are provided in Table 2-5. The *R* values indicate that AIRS has the strongest statistical relationship with CERES

estimates, while CM-SAF has the weakest. Regarding this issue, in section 2.3.1.4, detailed analysis of the OLR monthly/seasonal anomaly and its application in capturing ENSO cycles is described.

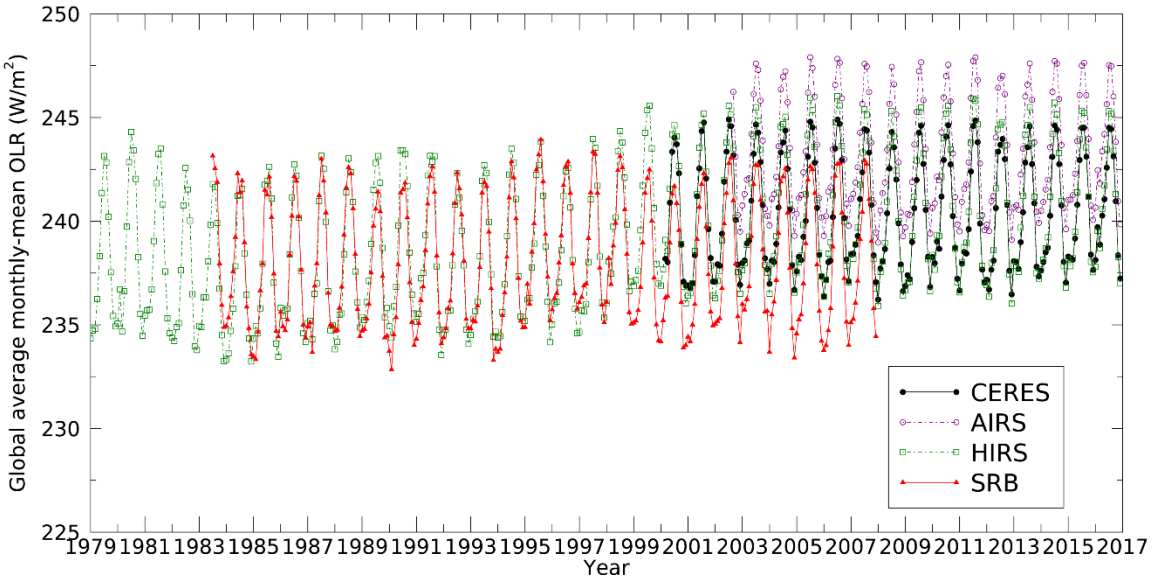

(a)

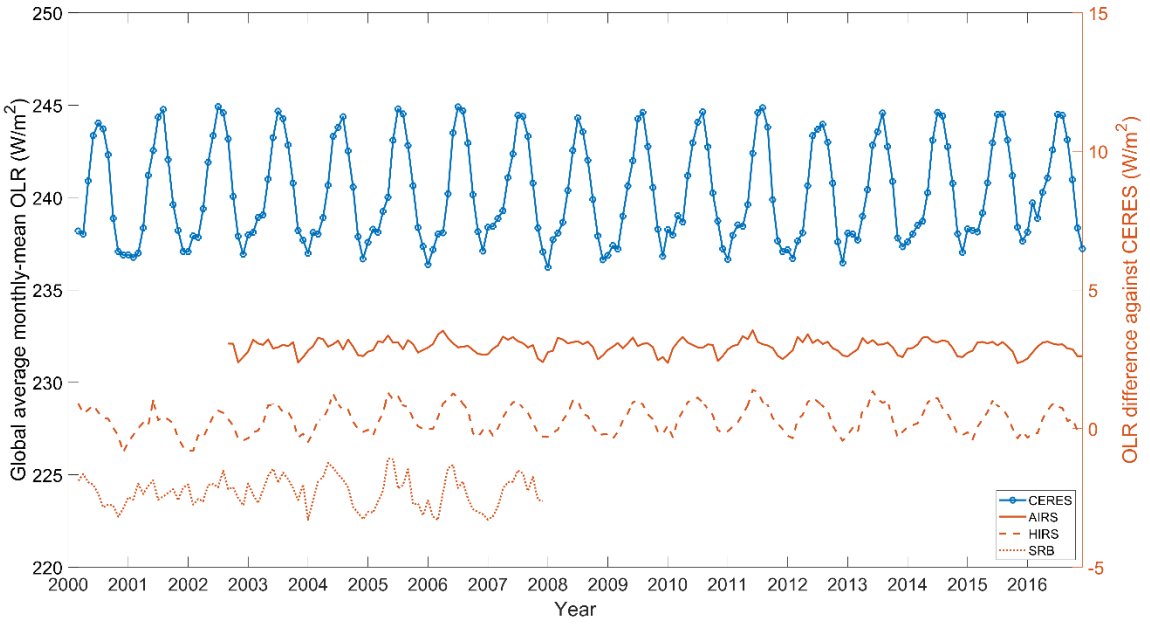

(b)

Figure 2-6 a) Long-term time-series of global average OLR from CERES and other five satellite OLR products from 1979 to 2016; and b) the biases against CERES OLR from 2000 to 2016

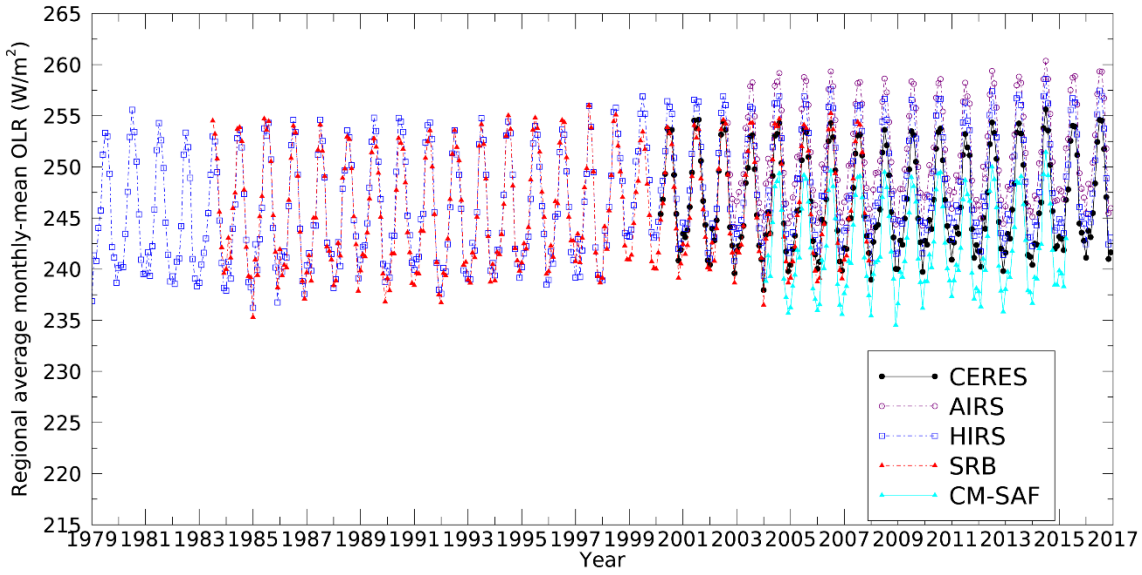

(a)

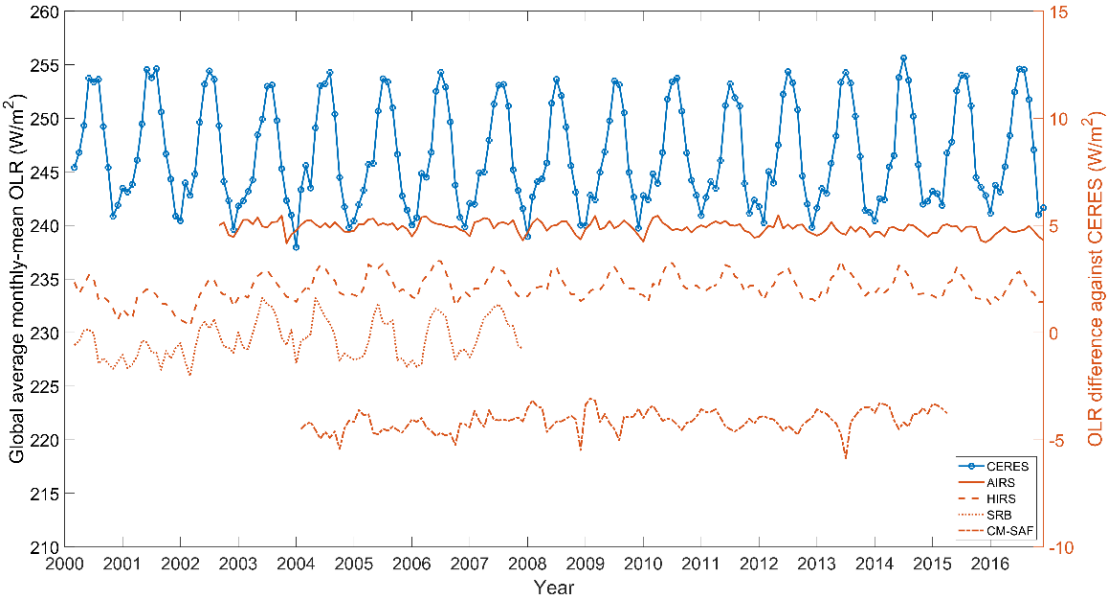

(b)

Figure 2-7 a) Long-term time-series of regional average OLR from CERES and other five satellite OLR products from 1979 to 2016; and b) the biases against CERES OLR from 2000 to 2016

Table 2-5 Correlation coefficients of the spatially-average OLR time-series between CERES and the five examined OLR products after removing the seasonal cycles.

	HIRS	SRB	AIRS	CMSAF
Global	0.65	0.61	0.57	
CM-SAF Regional	0.72	0.61	0.58	0.45

2.3.1.3 OLR characterizing the tropical expansion

Following the method stated in section 2.2.3, Figure 2-8 shows the zonally averaged temporal evolution of the HIRS OLR for DJF and JJA in the both hemispheres. The 250W/m^2 OLR contour is the line between light blue and yellow colors. For both hemispheres, the poleward extension of the 250W/m^2 contours are very obvious in both DJF and JJA seasons. In a quantitative way, the 250W/m^2 OLR contours were extracted from Figure 2-8 and were plotted against time in Figure 2-9. Obviously, both the northern and southern edge of the tropical band exhibits a systematic poleward trend from 1979 to 2016. For NH, the linear trend in the location of the northern edge is about 2.2° in DJF and 3.1° in JJA, respectively, with a statistical significance above the 99% confidence level (student t-test value is 8.485 in DJF and 5.769 in JJA; F-test value is 72.382 in DJF and 33.403 in JJA). For southern hemisphere (SH), it is about 2.8° in DJF and 2.1° in JJA with a statistical significance above the 99% confidence level (student t-test value is 6.489 in DJF and 6.401 in JJA; F-test value is 42.217 in DJF and 40.891 in JJA) as well. In total, the global tropical expansion could be determined as 5.3° in DJF and 4.9° (2.17° minus 0.38°) in JJA.

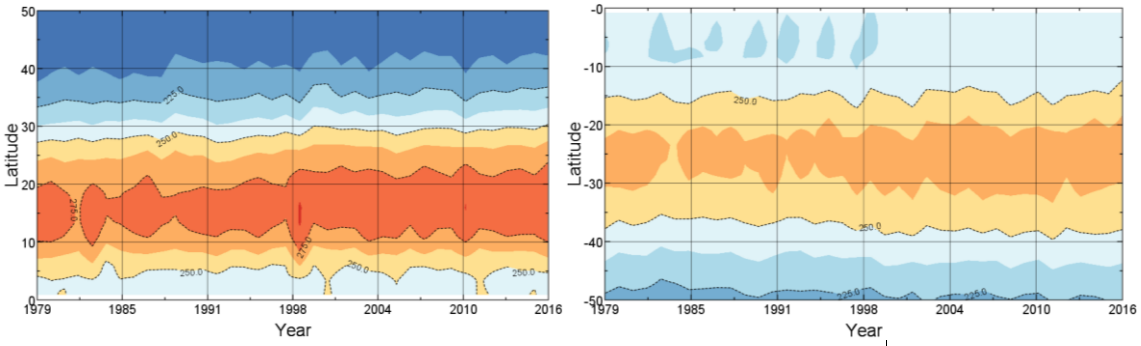

(a) (b)

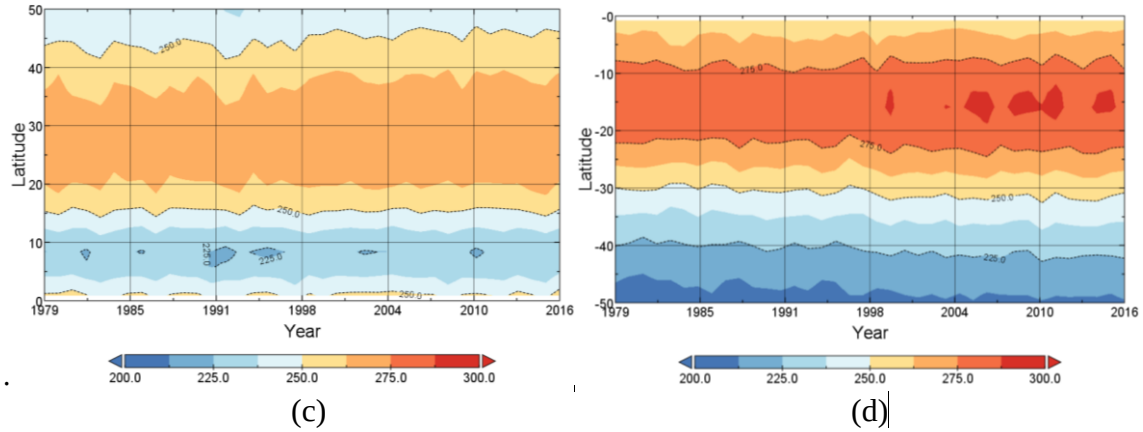

Figure 2-8 Time evolution of zonal-mean seasonal OLR from HIRS covering the period from 1979 to 2016. The OLR unit is W/m^2, and color interval is 12.5 W/m^2. The 250 W/m^2 OLR contour is the line between light blue and yellow colors. a) DJF in NH; b) DJF in SH; c) JJA in NH, and d) JJA in SH.

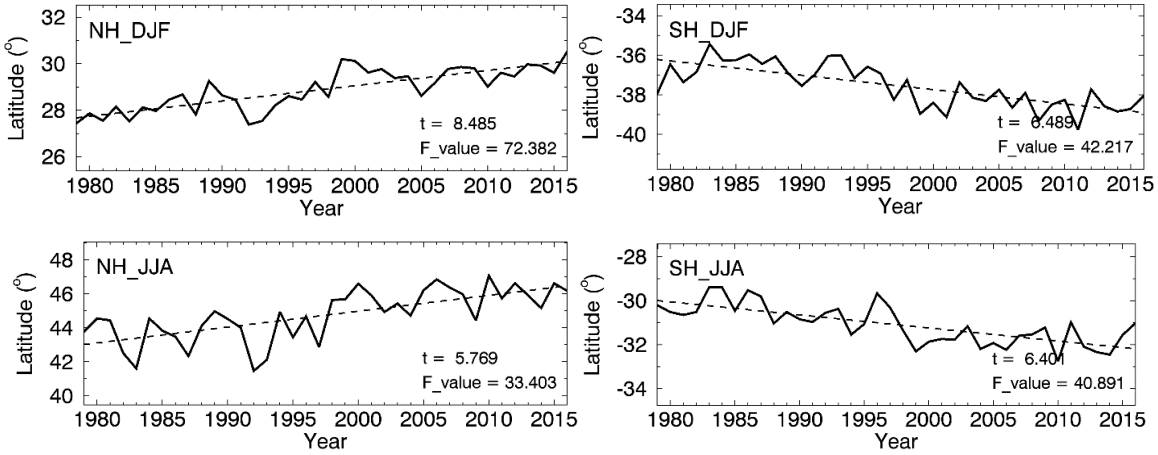

Figure 2-9 Time series of the poleward latitudes at which the seasonal and zonal mean OLR is equal to 250 W/m^2. Time period covers from 1979 to 2016. Left panel: NH; right panel: SH. Top panel: DJF; Bottom panel: JJA. Straight dashed-lines show linear trend plots.

Furthermore, the tropical expansion decadal rate was calculated in all the four seasons for NH, SH, and globe, respectively (Figure 2-10). It is found that the NH poleward expansion is quite obvious all satellite OLR products, with an obvious seasonality in JJA showing the largest expansion rate (Figure 2-10a). For SH, CERES and AIRS displays contradictions to other products, suggesting a slight tropical shrinking trend (Figure 2-10b). Since these two OLR products only cover the time period after 2000, it is a suggestion that the tropical expansion in SH slowed down and even slightly overturned in MAM and JJA

seasons compared to the period from 1980s to 2000. Nonetheless, as the total effect, tropical expansion is still identified by all products in all seasons (Figure 2-10c).

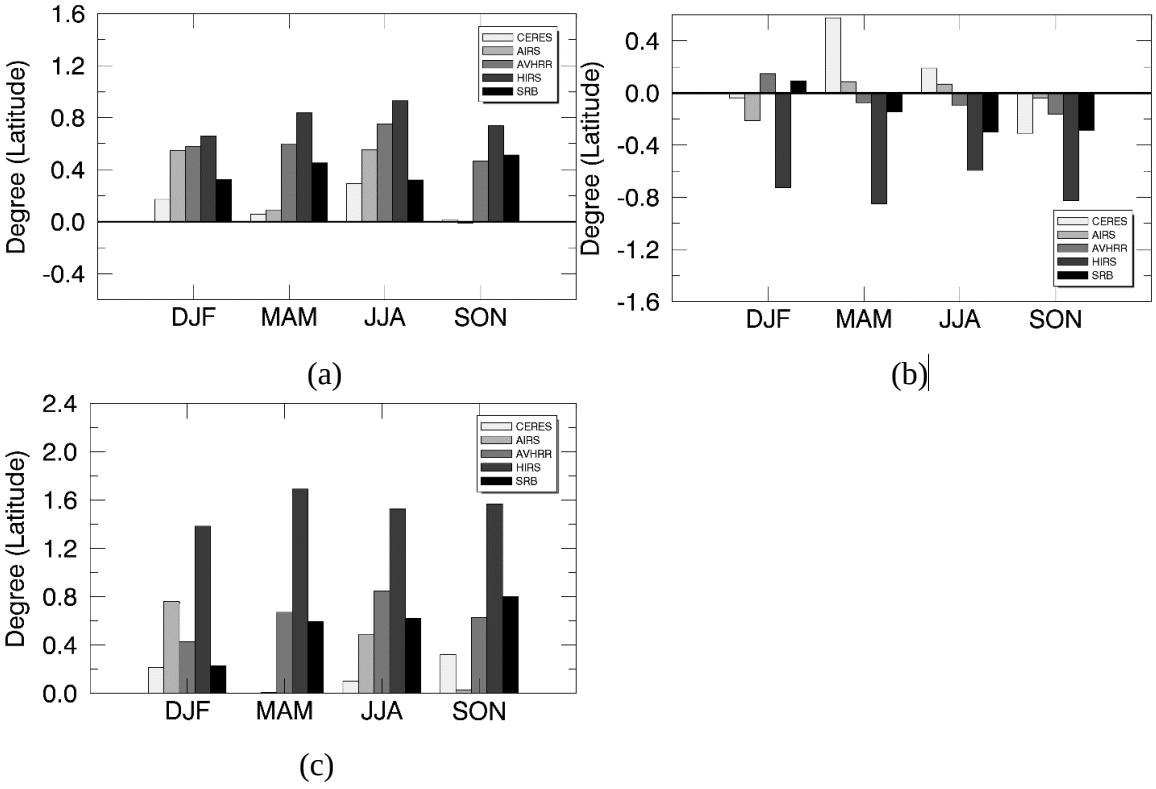

Figure 2-10 Poleward expansion of the 250 W/m^2 contour from satellite OLR products in four seasons. a) NH; b) SH; and c) total poleward expansion.

2.3.1.4 Evaluating the satellite OLR products in response of ENSO

Based on the ONI_{OLR} stated in section 2.2.4, Figure 2-11 and Figure 2-12 exhibit such an index of the peak period of a well-known El Niño (December, 2015) and La Niña event (December, 2010), respectively. As seen in Figure 2-11, for all the OLR products, the ONI_{OLR} displays extremely negative values (< -25 W/m^2) in the Niño 3.4 region. During El Niño, the Pacific Walker circulation is significantly modulated, leading to enhanced atmospheric convection and hence more cloud cover in the central and eastern equatorial Pacific lowering the OLR. In addition, more convective activity in this region induces higher and colder cloud tops, further resulting in a decrease in OLR. During La Niña, the

opposite occurs and OLR increases. This speculation is also supported by Figure 2-12 which shows that the ONI_{OLR} is highly positive in the Niño 4 region. Moreover, visual interpretation on Figure 2-11 and Figure 2-12 tells that the selected Niño regions don't perfectly match the OLR anomalies. OLR negative (positive) anomaly extends westward out of the Niño3.4 (Niño4) region, suggesting that the most appropriate regions to identify ENSO using satellite-retrieved OLR are slightly different from that using traditional SST index.

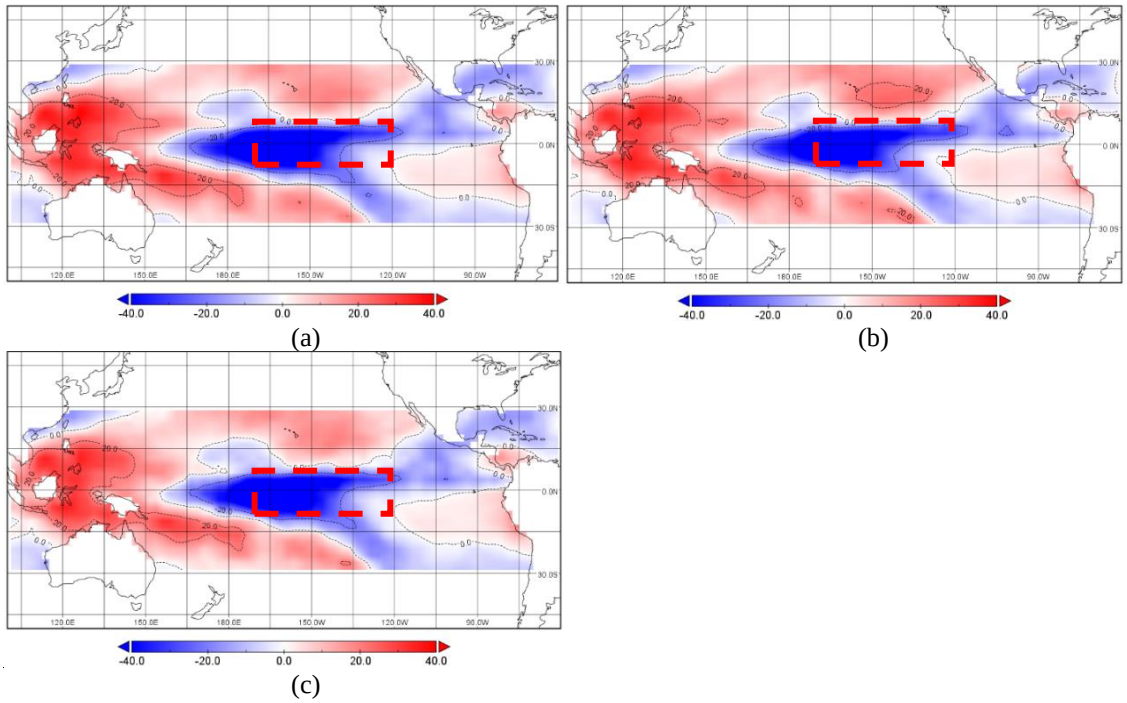

(a) (b)

(c)

Figure 2-11 Three-month running mean of OLR anomalies of a peak El Niño period (December 2015) within the central Pacific region (30°N–30°S, 100°E–60°W). OLR data are from a) CERES, b) HIRS, c) AIRS, respectively. The red boxes mark the Niño 3.4 region. Unit: W/m^2.

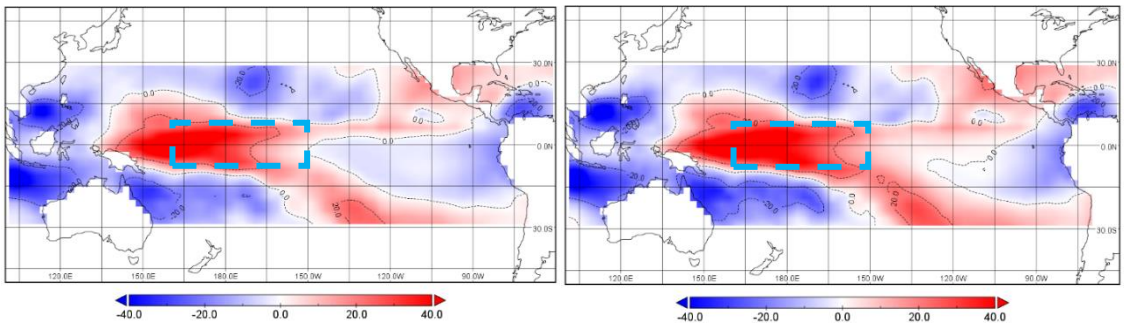

(a) (b)

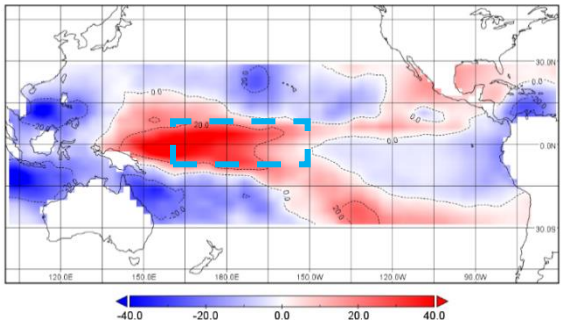

(c)

Figure 2-12 Three-month running mean of OLR anomalies of a peak La Niña period (December 2010) within the central Pacific region (30°N–30°S, 100°E–60°W). OLR data are from a) CERES, b) HIRS, c) AIRS, respectively. The blue boxes mark the Niño 4 region. Unit: W/m^2.

Although the magnitude of the response varies, all the OLR products are able to capture the selected El Niño and La Niña events. To explore their capability in capturing ENSO cycles in long-time series, correlation analysis between ONI_{SST} and ONI_{OLR} was also conducted. Figure 3-23 plots the variations of ONI_{SST} in the Niño 3.4 (Figure 3-23a) and Niño 4 (Figure 3-23b) regions from 1979 to 2016. With the threshold of +0.5°C (-0.5°C) employed, the El Niño (La Niña) cycles can be clearly identified. Similarly, the time-series of ONI_{OLR} from the satellite-retrieved OLR products (taking HIRS as an example) were also calculated for the two Niño regions and are shown in Figure 2-13a and Figure 2-13b. It is evident that the temporal changes of ONI_{SST} and ONI_{OLR} are strongly and negatively correlated (R = -0.77 and -0.80 in Niño 3.4 and Niño 4, respectively). More details are illustrated in Figure 2-13c and Figure 2-13d, by separating the [ONI_{SST}, ONI_{OLR}] pairs into four zones corresponding to the four quadrants in the Cartesian coordinate system. In Niño 3.4 (Figure 2-13c), the negative correlation of data in quadrant IV (R_w = -0.80) is much stronger than that of quadrant II (R_c = -0.42). Considering that a positive ONI_{SST} indicates the occurrence of El Niño, the results clearly indicate that ONI_{OLR} can capture El Niño fairly well in Niño 3.4, but performs much worse in capturing La Niña. In addition, the data located in quadrant I denote the months determined as El Niño or pre-El Niño by

ONI_{SST} but missed by ONI_{OLR}. Because ONI_{SST} is considered as the reference in the comparison, these points can be counted for an indication of the omission error of ONI_{OLR}. Then, quadrant III contributes to the omission error following the same analogy. In Niño 4 (Figure 2-13d), although ONI_{OLR} correlates to El Niño more so than to La Niña, the absolute value of R_c increases to 0.61, which is higher than that in Niño 3.4 (0.44). In fact, these results support the claim that Niño 4 is better in capturing La Nina than Niño 3.4 as previously stated. Table 2-6 summarizes the statistics of all OLR products. In general, ONI_{OLR} has a much greater capability of capturing El Niño than it does of capturing La Niña, and among the five OLR products, HIRS performs the best in capturing both El Niño and La Niña.

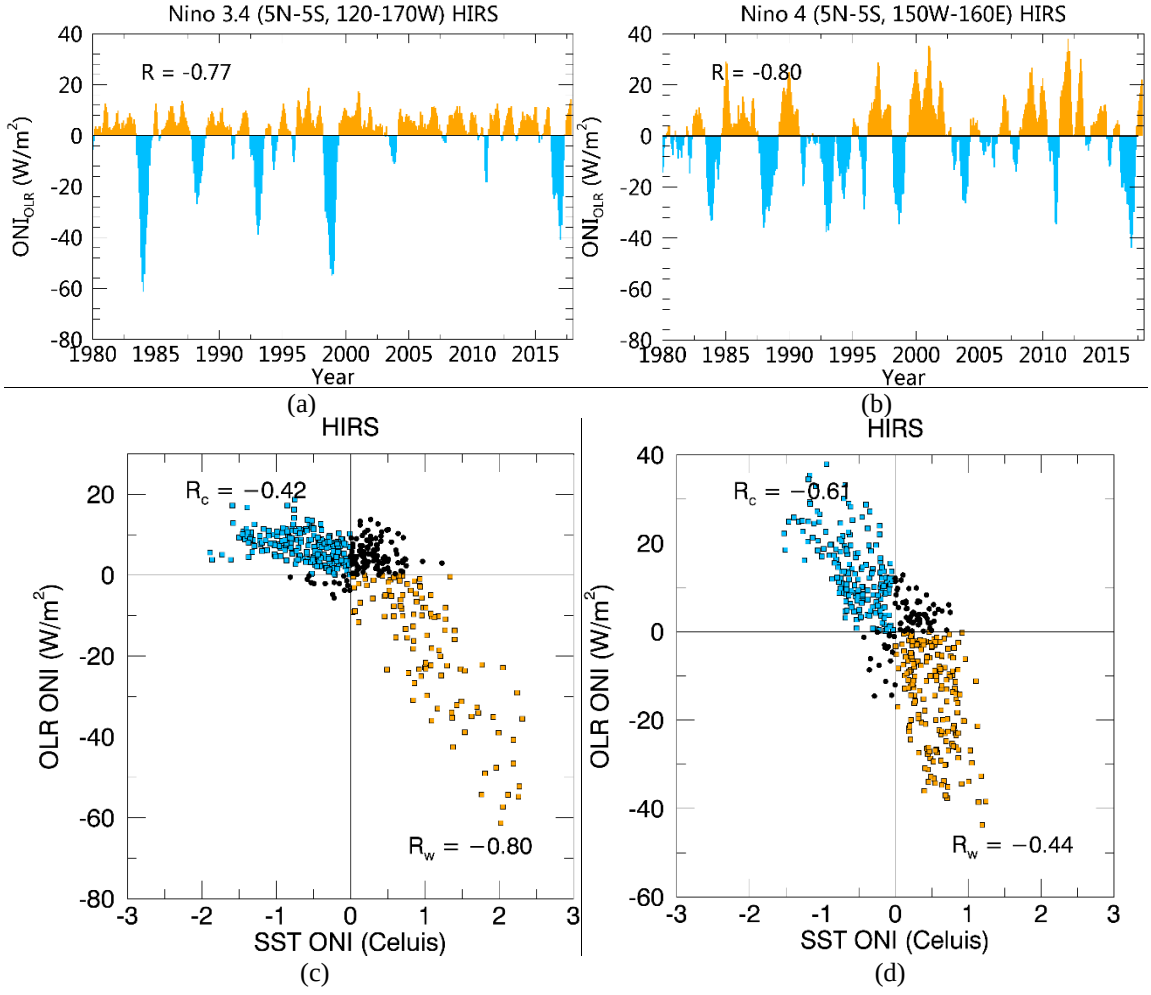

Figure 2-13 Long-time series (1979–2016) of the spatially averaged ONI_{OLR} for the a) Niño 3.4 and b) Niño 4 regions from the HIRS retrieved product. Relationship between ONI_{OLR} and ONI_{SST} is shown in c) and d) for the Niño 3 and Niño 4 regions, respectively.

Table 2-6 Statistics of the long-time series comparison between ONI_{OLR} calculated from the five OLR products and ONI_{SST} in the Niño 3.4 and Niño 4 regions, respectively.

	Niño 3.4			Niño 4		
	R (Overall)	R (El Niño)	Omi. Err	R (Overall)	R (La Niña)	Omi. Err
CERES	-0.74	-0.85	18.33%	-0.85	-0.57	7.26%
HIRS	-0.77	-0.80	17.45%	-0.80	-0.61	5.83%
SRB	-0.77	-0.82	20.34%	-0.80	-0.58	6.60%
AIRS	-0.76	-0.86	21.36%	-0.85	-0.60	8.31%

2.3.2 Reanalysis OLR

2.3.2.1 OLR climatology

Figure 2-14a and Figure 2-15a present the CERES EBAF monthly OLR climatologies for the DJF and JJA, respectively, for a 16-year period (2001–2016). CERES OLR values display obvious latitude-dependent distributions owing to the surface and atmospheric temperature, and the NH emits much more longwave radiation during the JJA than it does during the DJF. At the same latitude, OLR varies with surface type and altitude, as seen comparing the Amazon Forest and Middle Africa in Figure 2-14a, and the Sahara Desert and Tibetan Plateau in Figure 2-15a. Maps of OLR differences among the seven reanalysis OLR and those of CERES are also plotted accordingly (Figure 2-14b–h and Figure 2-15b–h). Statistics of the three metrics (correlation coefficient [R], bias, and root-mean-squared-deviation [RMSD]) are reported in Table 2-7. Note that for those datasets that only partially cover the CERES time span (2001–2016), the overlapping periods between them (refer to Table 2-2) were extracted for comparison. It is apparent that all selected reanalysis OLR products are higher than that of the CERES monthly OLR except

for those of the NCEP-NCAR which show a slight negative bias. In addition, although CERES OLR values have a different spatial pattern between DJF and JJA, the OLR difference maps show similar trends between the two seasons.

JRA-25 has the largest bias (~ 14 W/m^2) and RMSD (~ 16 W/m^2) among all the reanalysis datasets. Two vegetation-dominated regions, the Amazon Forest and Middle Africa, contribute most to the positive biases. From Figure 2-14a and Figure 2-15a, it can be seen that these two regions show obviously lower OLR than their surroundings, suggesting that JRA-25 OLR fails to present differences between vegetated areas and the ocean surface. JRA-55 adjusted the longwave radiation scheme and improved the forecasting model (Kobayashi et al., 2015), which is likely why the JRA-55 OLR agrees better with that of CERES than does JRA-25 (bias: ~11 W/m^2, RMSD: ~13 W/m^2). However, for TOA longwave flux, an uncertainty more than 10 W/m^2 is still too large to be compatible within climatic models. ERA-Interim achieves much better agreement with CERES than the two JRA reanalyses, with a bias of approximately 6 W/m^2 and an RMSD of approximately 7 W/m^2, which might be attributed to the upgrades of the 4D-Var forecast model and RRTM radiative model. MERRA appears to be better still especially during the JJA (bias: 2.63 W/m^2), while the RMSDs of MERRA are even greater than those of ERA-Interim. Figure 2-15e provides a clue of this seeming contradiction: Middle Africa, the Equatorial Pacific Ocean, and the Tibetan Plateau contribute a relatively large deviation up to 20 W/m^2, but the Caribbean Sea, Northern Indian Ocean, and Western Equatorial Pacific Ocean balance the mean bias by displaying smaller OLR as compared to that of CERES up to -20 W/m^2. In addition, high-latitude areas show almost no OLR differences, and the mean bias of MERRA during the JJA is as low as 2.63 W/m^2. NCEP-NCAR is the only

reanalysis dataset achieving negative bias, though very slightly, to CERES during both seasons (bias: -0.56 W/m^2 in DJF and -0.94 W/m^2 in JJA). However, similar to those of MERRA, the RMSDs of NCEP-NCAR are relatively high (8.77 W/m^2 for DJF and 9.60 W/m^2 for JJA), suggesting its OLR differences also have relatively large spatial variations, which is supported by Figure 2-14f and Figure 2-15f. Similar situations are also found for NCEP-DOE. NCEP-CFSR, as the newest NCEP reanalysis dataset, shows the best agreement with CERES in general, with the lowest RMSDs (< 7.4 W/m^2) and relatively small biases (< 4 W/m^2) during both seasons. Although the biases and RMSDs vary with different datasets and seasons, the correlation coefficients of all of them are close to one, implying that all the reanalysis OLR products are able to capture well the OLR spatial contrast overall.

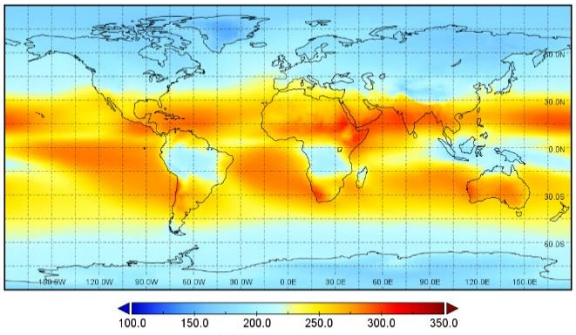

(a) CERES

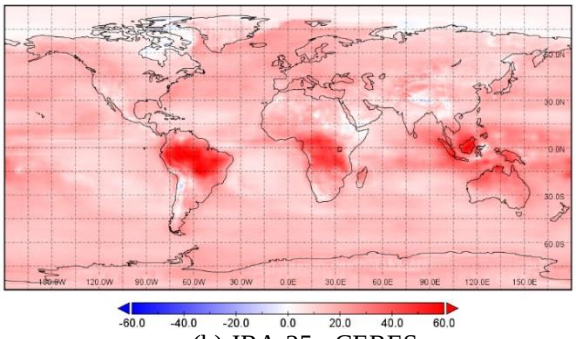

(b) JRA-25 - CERES

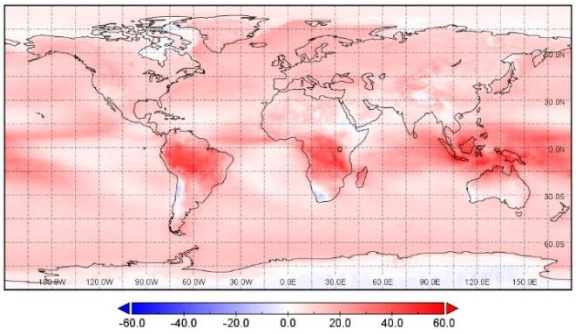

(c) JRA-55 - CERES

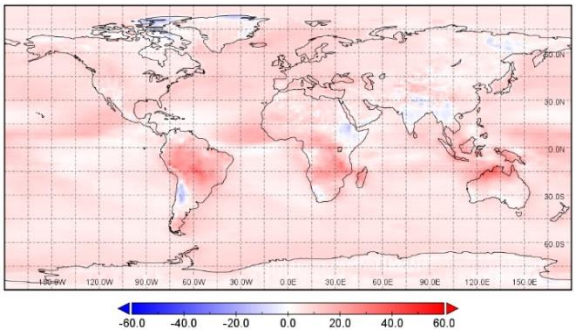

(d) ERA-Interim - CERES

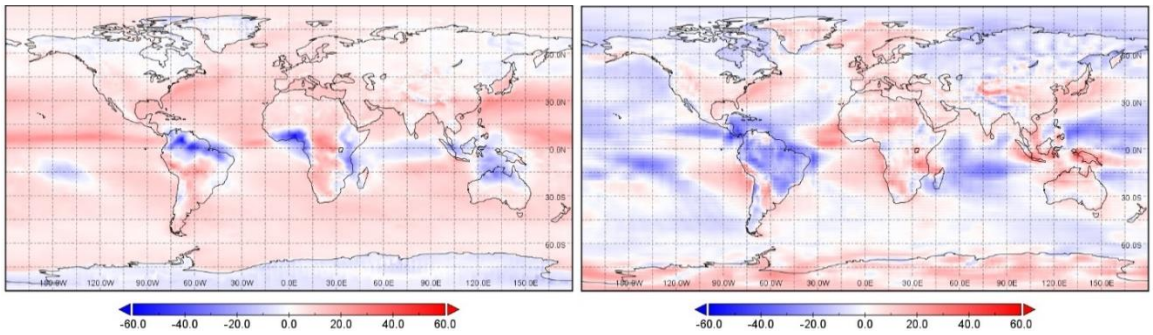

(e) MERRA - CERES (f) NCEP-NCAR - CERES

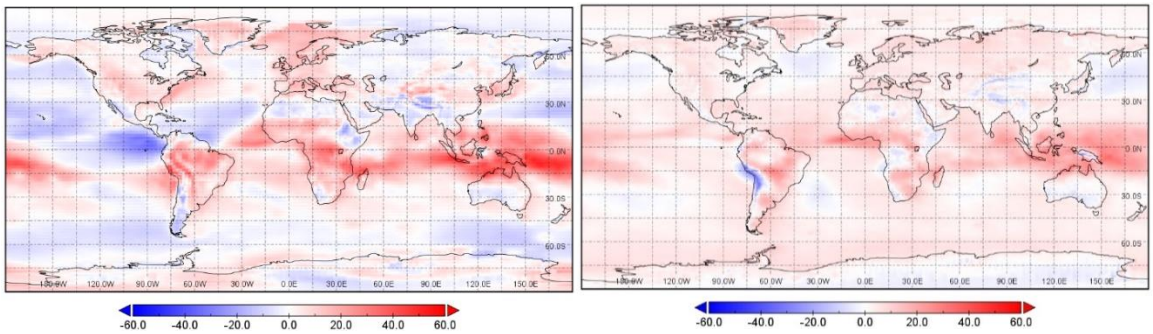

(g) NCEP-DOE - CERES (h) NCEP-CFSR - CERES

Figure 2-14 CERES EBAF monthly OLR climatology for DJF and the biases between the reanalysis OLR products and CERES OLR from 2000 to 2016: a) CERES monthly OLR for DJF; b) JRA-25 minus CERES; c) JRA-55 minus CERES; d) ERA-Interim minus CERES; e) MERRA minus CERES; f) NCEP-NCAR minus CERES; g) NCEP-DOE minus CERES; h) NCEP-CFSR minus CERES.

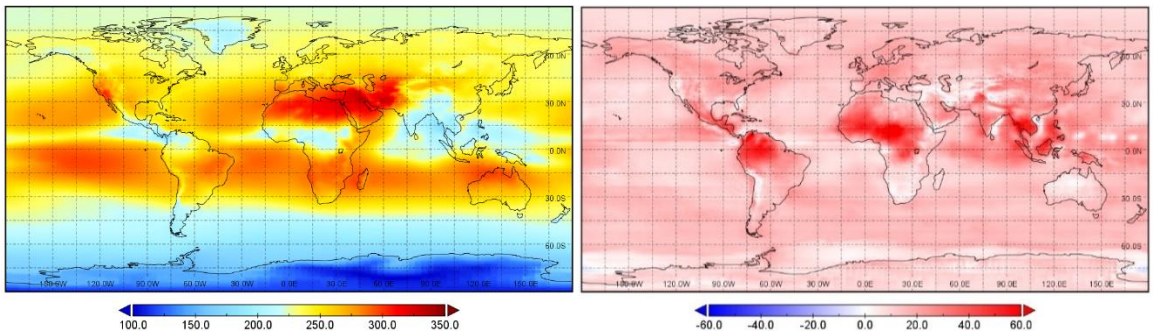

(a) CERES (b) JRA-25 - CERES

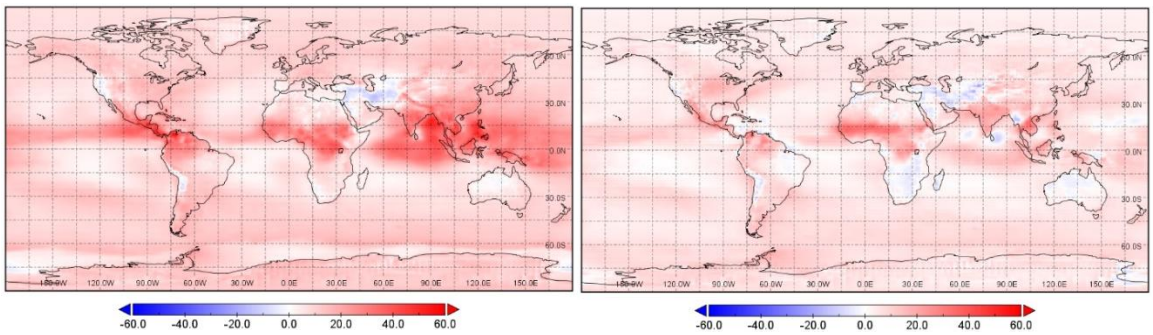

(c) JRA-55 - CERES (d) ERA-Interim - CERES

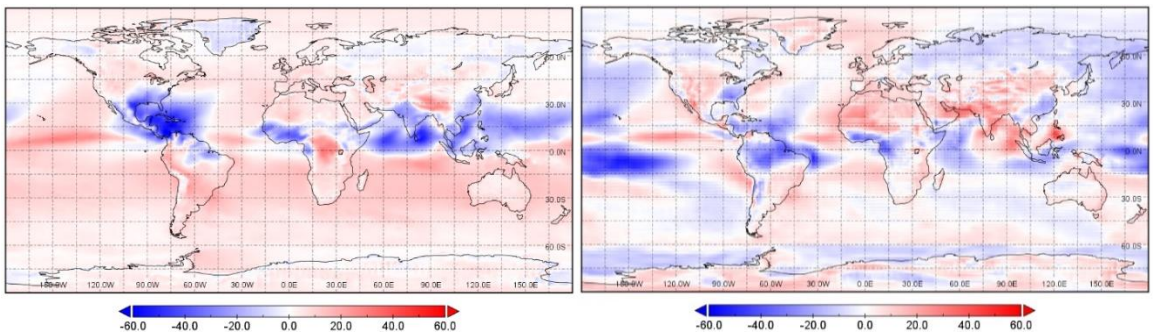

(e) MERRA - CERES (f) NCEP-NCAR - CERES

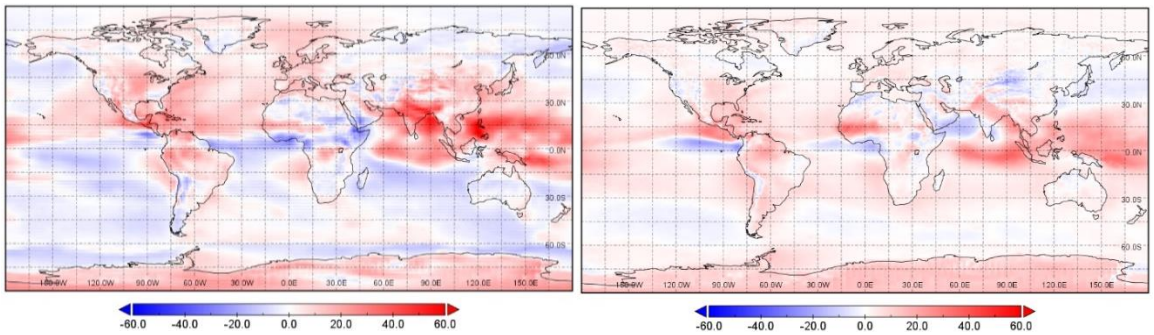

(g) NCEP-DOE - CERES (h) NCEP-CFSR - CERES

Figure 2-15. CERES EBAF monthly OLR climatology for JJA and the biases between the reanalysis OLR products and CERES OLR from 2000 to 2016: a) CERES monthly OLR for JJA; b) JRA-25 minus CERES; c) JRA-55 minus CERES; d) ERA-Interim minus CERES; e) MERRA minus CERES; f) NCEP-NCAR minus CERES; g) NCEP-DOE minus CERES; h) NCEP-CFSR minus CERES.

Table 2-7 Statistics of the global comparison between reanalysis OLR products against CERES OLR using the monthly mean climatology during DJF and JJA, respectively.

Reanalysis Data	*R*		Bias (W/m^2)		RMSD (W/m^2)	
	DJF	JJA	DJF	JJA	DJF	JJA
JRA-25	0.98	0.99	14.47	14.16	16.34	16.04
JRA-55	0.98	0.99	10.67	11.10	13.12	13.08
ERA-Interim	0.99	1.00	6.33	5.91	7.49	7.26
MERRA	0.99	0.98	4.12	2.63	7.76	9.34
NCEP-NCAR	0.97	0.98	-0.56	-0.94	8.77	9.60
NCEP-DOE	0.97	0.98	2.60	3.41	9.73	10.40
NCEP-CFSR	0.99	0.99	3.91	3.99	6.42	7.34

Visual interpretation of Figure 2-14 and Figure 2-15 imply that the OLR differences among reanalysis datasets and CERES are latitude-dependent, and Figure 2-16 confirms that in a quantitative way. In general, all reanalysis OLR values exhibit larger uncertainties

in tropical areas than in middle- and high-latitude areas. The NCEP-NCAR estimate of OLR is slightly smaller than that of CERES in nearly all latitudinal zones, showing a peak negative bias in tropical areas especially during the JJA. MERRA shows a slightly larger OLR than that of CERES in general, but the bias drastically decreases to zero (during DJF) and even to a significantly negative bias (~13 W/m^2 during JJA) in equatorial areas. In contrast, all the other reanalysis datasets display peak positive biases in tropical areas, and these gradually decrease toward medium- and high-latitude areas. Moreover, by comparing Figure 2-16a and Figure 2-16b, it can be seen that the peak biases are around 0° during DJF shifting northward to ~15°N during JJA, coinciding with the move of the high OLR areas between the two seasons inferred from Figure 2-14a and Figure 2-15a. This further indicates that the reanalyses models perform better at a lower OLR level than at a higher OLR level.

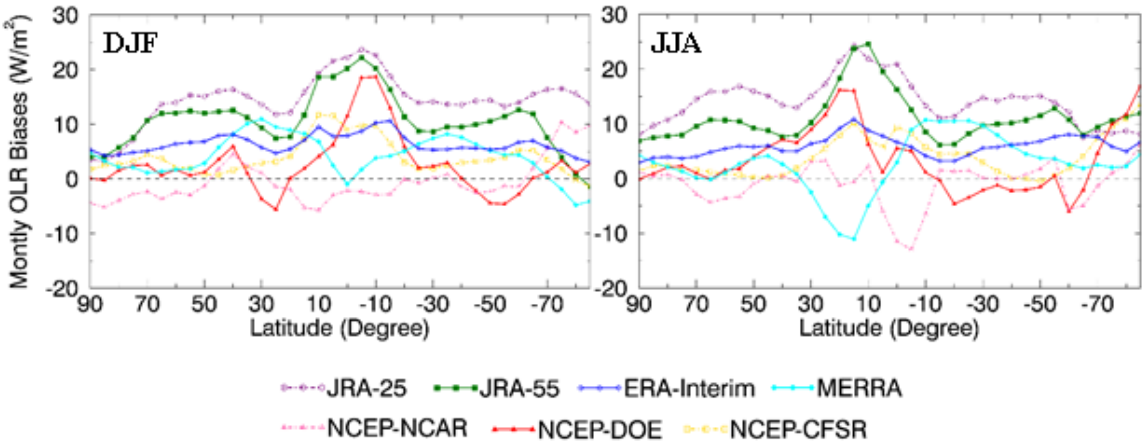

Figure 2-16. Monthly mean OLR biases of seven reanalysis datasets against CERES as a function of latitude during DJF and JJA, respectively. Statistics are the averaged biases within each 5° latitudinal zone based on the underlying data of Figure 1 and Figure 2.

Furthermore, Table 2-8 reports the OLR biases between CERES and the reanalysis datasets across different surface types. For JRA-25 and JRA-55 that have the largest overall biases, land contributes more to the positive biases than does ocean, and vegetation has

larger biases than those of the other two land covers in general. The situations are just the opposite for MERRA, which achieves fairly good agreement with CERES over-land (< 2 W/m^2) but poor agreement over ocean. ERA-Interim exhibits the most consistent spatial pattern, with OLR biases concentrated from 3 W/m^2 to 7 W/m^2 over all surfaces. For NCEP-NCAR, the only underestimating CERES OLR, it is obvious that the negative overall bias originates from vegetation and ocean surfaces. The overall biases of land are balanced to be slightly positive by the relatively large overestimation from barren land and snow/ice surfaces. With the upgrades in models and observation data, NCEP-NCAR, NCEP-DOE and NCEP-CFSR have significantly improved OLR estimation over barren land (biases < 1.6 W/m^2) and over snow/ice during DJF (biases < 2.5 W/m^2). However, it is interesting that NCEP-DOE and NCEP-CFSR perform much worse over snow/ice surfaces during the JJA (biases > 10 W/m^2). Reviewing Figure 2-14g–h and Figure 2-15g–h, it is clear that Antarctica, which is dominated by snow and ice, displays a much higher positive bias during JJA as compared to DJF, suggesting that the improved longwave radiation models of NCEP-DOE and NCEP-CFSR may not able to handle the polar regions at night very well.

Table 2-8. Biases between reanalysis OLR products against CERES OLR over different surface types during DJF and JJA, respectively. Unit: W/m^2.

Reanalysis Datasets		Vegetation	Desert/ Barren land	Snow/Ice	Land Overall	Ocean
JRA-25	DJF	17.38	11.65	14.07	15.80	13.82
	JJA	19.12	20.07	9.40	15.98	13.28
JRA-55	DJF	14.03	7.61	2.06	9.53	11.21
	JJA	12.90	6.19	11.07	11.73	10.80
ERA-Interim	DJF	7.14	5.27	3.44	5.76	6.60
	JJA	6.74	5.64	5.80	6.34	5.71
MERRA	DJF	1.61	5.67	-3.65	0.21	6.00

NCEP-NCAR	JJA	0.96	3.50	2.20	1.59	3.13
	DJF	-1.07	4.96	7.84	2.39	-1.97
	JJA	-1.80	8.97	3.95	1.00	-1.88
NCEP-DOE	DJF	4.87	1.58	2.17	3.70	2.07
	JJA	3.79	1.34	11.09	6.00	2.17
NCEP-CFSR	DJF	4.63	0.78	0.46	2.93	4.38
	JJA	3.06	1.04	10.20	5.25	3.38

2.3.2.2 OLR time series comparison

Comparisons of OLR climatologies (section 2.3.2.1) are manifested in the state of multi-year mean OLR and its global spatial pattern. To recover OLR inter-annual variation, long-term time-series comparisons were also conducted. For each month since the start of the satellite era (1979), the global-average monthly OLR was calculated using the latitudinal-weighted method, and the generated OLR time-serial curves of all the selected reanalysis datasets and CERES were plotted as seen in Figure 2-17. Taking CERES as the reference data, scatter plots and statistics were completed and are reported in Figure 2-18. Similar to the aforementioned results, JRA-25 and JRA-55 estimate larger OLR as compared to that of CERES, up to 15.62 W/m^2 and 12.36 W/m^2, respectively. ERA-Interim, MERAA, NCEP-DOE, and NCEP-CFSR show similar agreement with CERES, within a range of 3 W/m^2 to 7 W/m^2. NCEP-NCAR achieves the highest accuracy (absolute deviation = 0.94 W/m^2) and lowest uncertainty (RMSD = 1.16 W/m^2). On the other hand, it was observed that the temporal correlation between CERES and all the reanalysis datasets is very high (MERAA = 0.88, others > 0.9). This is reasonable because the correlation coefficient profits from the strong OLR seasonal dependencies if monthly data are investigated. After removing the seasonal cycle, the correlation coefficients were recalculated and are provided in Figure 2-18 (in the bracket). The modified *R* indicates that

JRA-25 has the highest correlation to CERES, while NCEP-CFSR has the lowest correlation. Regarding this issue, in section 2.3.2.4, detailed analysis of the OLR monthly anomaly and its application in capturing ENSO cycles is described.

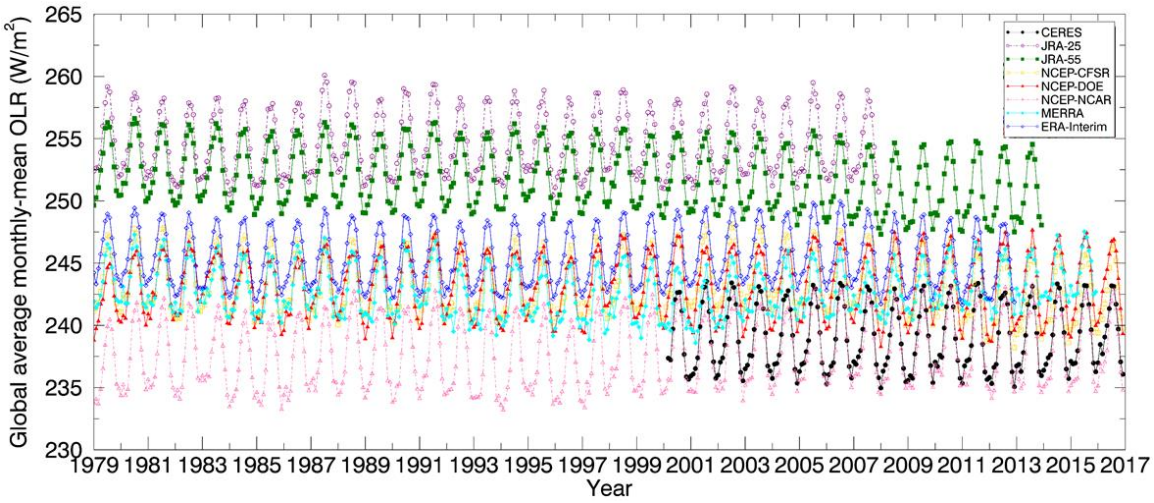

Figure 2-17 Long-term time-series of global average OLR from CERES and seven reanalysis OLR products

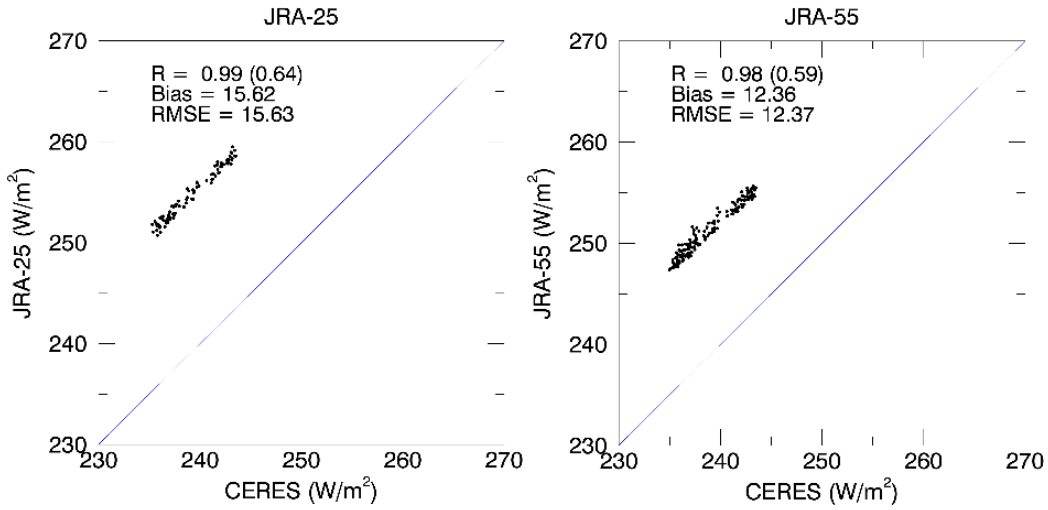

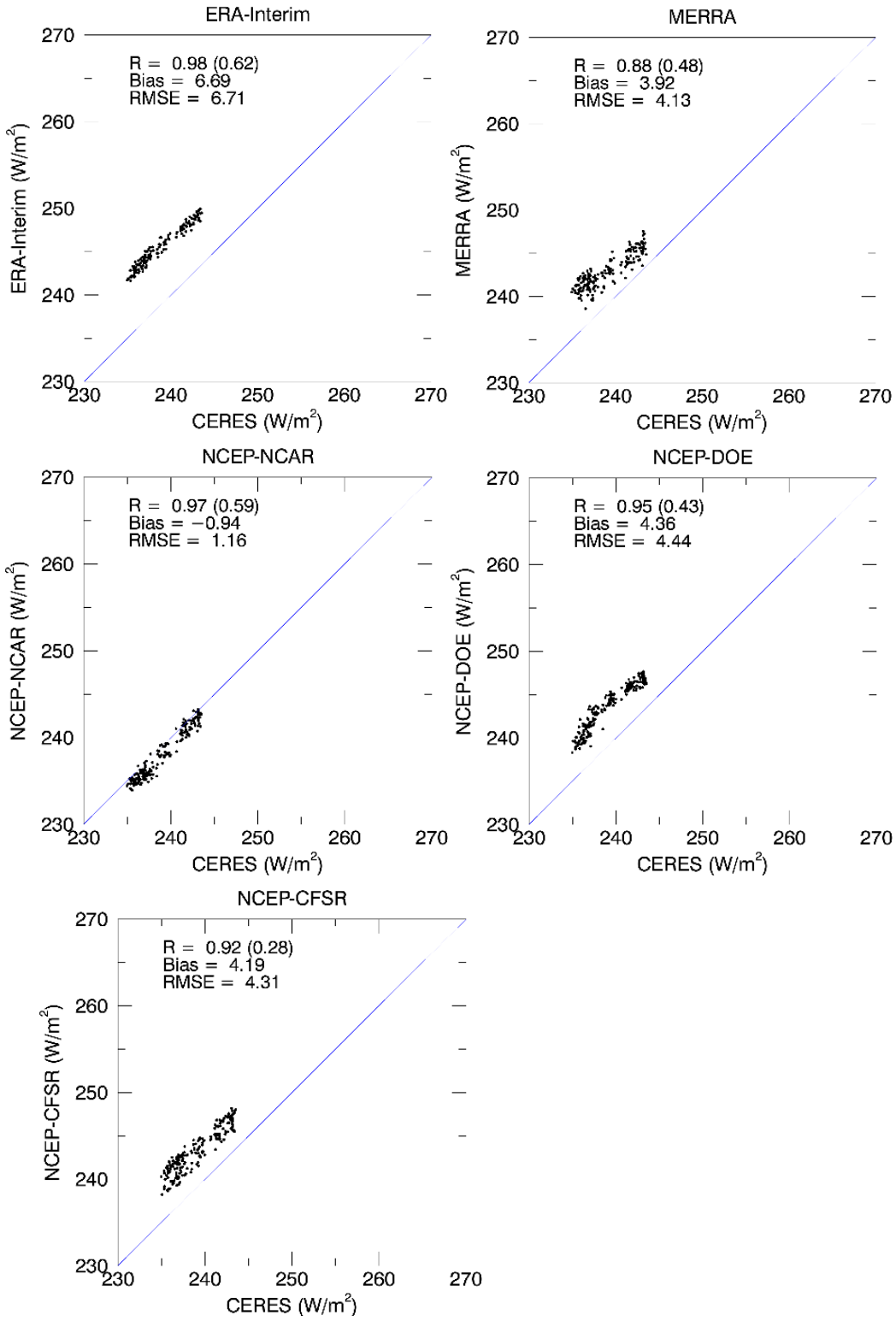

Figure 2-18 Comparison of long-term time-series of global average monthly OLR between CERES and seven reanalysis OLR products.

2.3.2.3 OLR characterizing the tropical expansion

Similar to that perform for satellite OLR retrievals in section 2.3.1.3, this section tested whether these reanalysis OLR datasets can well monitor the tropical expansion. Taking NCEP-NCAR data as an example, Figure 2-19 shows the zonally averaged temporal evolution of the OLR during DJF and JJA in both hemispheres. The 250-W/m^2 OLR contour is the line between the light blue and yellow colors. Visual examination approximately shows that the poleward extension of the northern Hadley circulation branch appears to be a systematic robust feature of the analyses during both the DJF (Figure 2-19a) and JJA (Figure 2-19c) seasons. However, there seems to be no obvious poleward extension of the southern Hadley circulation branches during both seasons (Figure 2-19c and Figure 2-19d). In a quantitative manner, the 250-W/m^2 OLR contours were extracted from Figure 2-19 and plotted against time in Figure 2-20. Obviously, the northern edge of the tropical band exhibits a systematic poleward trend from 1979 to 2016. The linear trend in the location of the northern edge is approximately 1.44° during DJF and 2.17° during JJA, respectively, with a statistical significance above the 99% confidence level (the student t-test value was 3.420 for DJF and 3.899 for JJA and the F-test value was 11.802 for DJF and 15.273 for JJA). For the SH, no significant expansion was found during DJF (|t-value| = 0.273, F-value = 0.070), while a slight tropical contraction (0.38°) was found during JJA with a statistical significance above the 90% confidence level (|t-value| = 2.054, F-value = 4.249). In total, the global tropical expansion could be determined as 1.44° during DJF and 1.79° (2.17° minus 0.38°) during JJA.

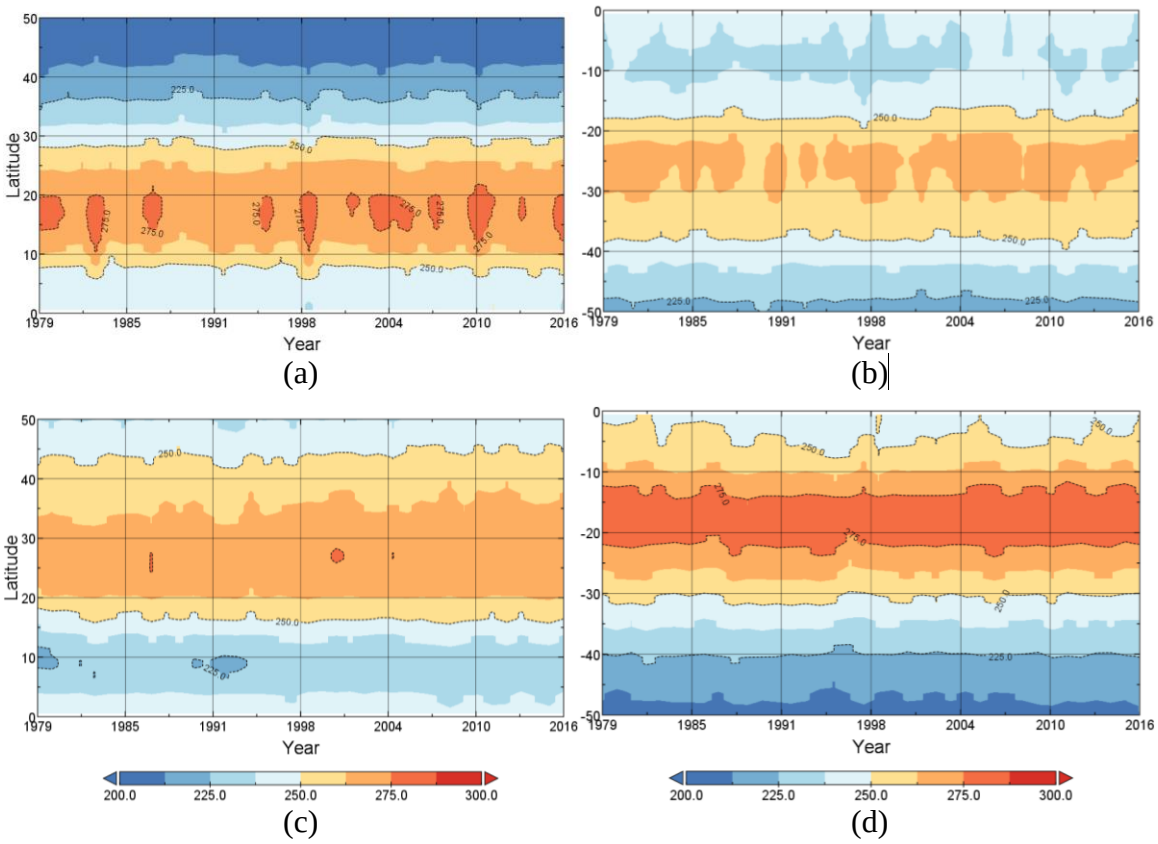

Figure 2-19 Time evolution of zonal-mean seasonal OLR from the NCEP-NCAR dataset covering the period from 1979 to 2016. The OLR unit is W/m^2 and the color interval is 12.5 W/m^2. The 250-W/m^2 OLR contour is the line between the light blue and yellow colors. a) DJF in the NH; b) DJF in the SH; c) JJA in the NH, and d) JJA in the SH.

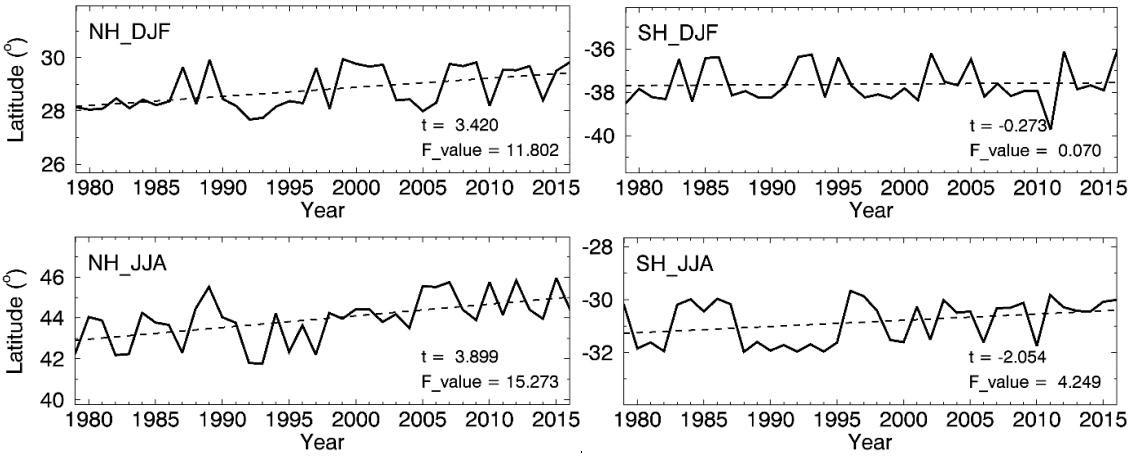

Figure 2-20 Time series of the poleward latitudes in which the seasonal and zonal mean OLR is equal to 250 W/m^2. The time period covers from 1979 to 2016. Left panel: NH; right panel: SH. Top panel: DJF; Bottom panel: JJA. Straight dashed-lines show linear trend plots.

Furthermore, the tropical expansion decadal rate was calculated for all four seasons for the NH, SH, and globe, respectively (Figure 2-21). It was found that the NH poleward

expansion is robust and systematic among all reanalysis datasets, with an obvious seasonality during JJA showing the highest expansion rate (Figure 2-21a). For the SH, most of the datasets did not show an expansionary trend with a statistical significance above 90%, although the calculation provided a slight tropical contractual trend (Figure 2-21b). Regarding the total effect, tropical expansion was still identified by all datasets during JJA, and by most of them during fall (Figure 2-21c).

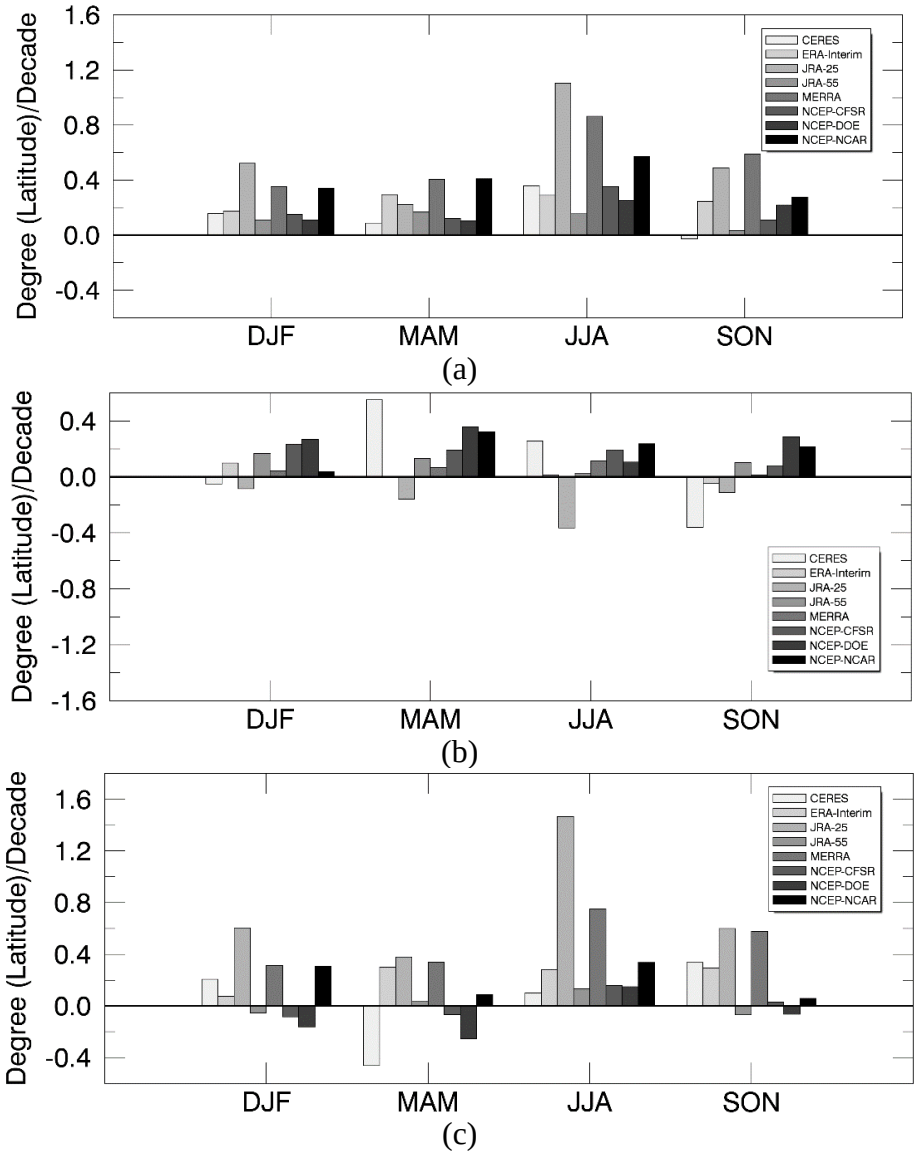

Figure 2-21 Poleward expansion of the 250-W/m^2 contour from the seven reanalysis OLR and CERES OLR datasets for the four seasons. a) NH; b) SH; and c) total poleward expansion.

2.3.2.4 Evaluating the reanalysis OLR products in response of ENSO

Similar to that of satellite OLR retrievals performed in section 2.3.1.4, this section tested whether the inter-annual variations of the reanalysis monthly OLR values can closely reflect El Niño and La Niña based on the Niño 3.4 and Niño 4 regions, respectively. Figure 2-22 and Figure 2-23 exhibit the ONI_{OLR} of the peak period of a typical El Niño (December, 1997) (Trenberth, 1997b) and La Niña event (December, 1988) (Inoue and Sugimura, 1992), respectively. As seen in Figure 2-22, for all reanalysis datasets, the ONI_{OLR} displays extremely negative values (< -30 W/m^2) in the Niño 3.4 region. During El Niño, the Pacific Walker circulation is significantly modulated, leading to enhanced atmospheric convection and hence more cloud cover in the central and eastern equatorial Pacific lowering the OLR. In addition, more convective activity in this region induces higher and colder cloud tops, further resulting in a decrease in OLR. During La Niña, the opposite occurs and OLR increases. This speculation is also supported by Figure 2-23 which shows that the ONI_{OLR} is highly positive in the Niño 4 region.

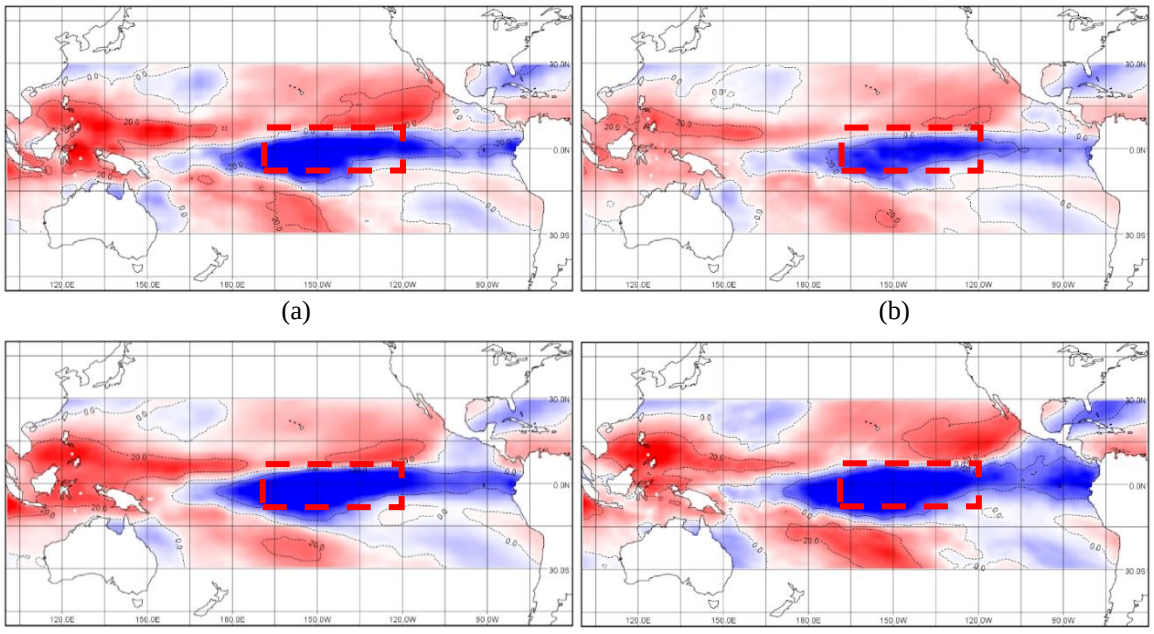

(a) (b)

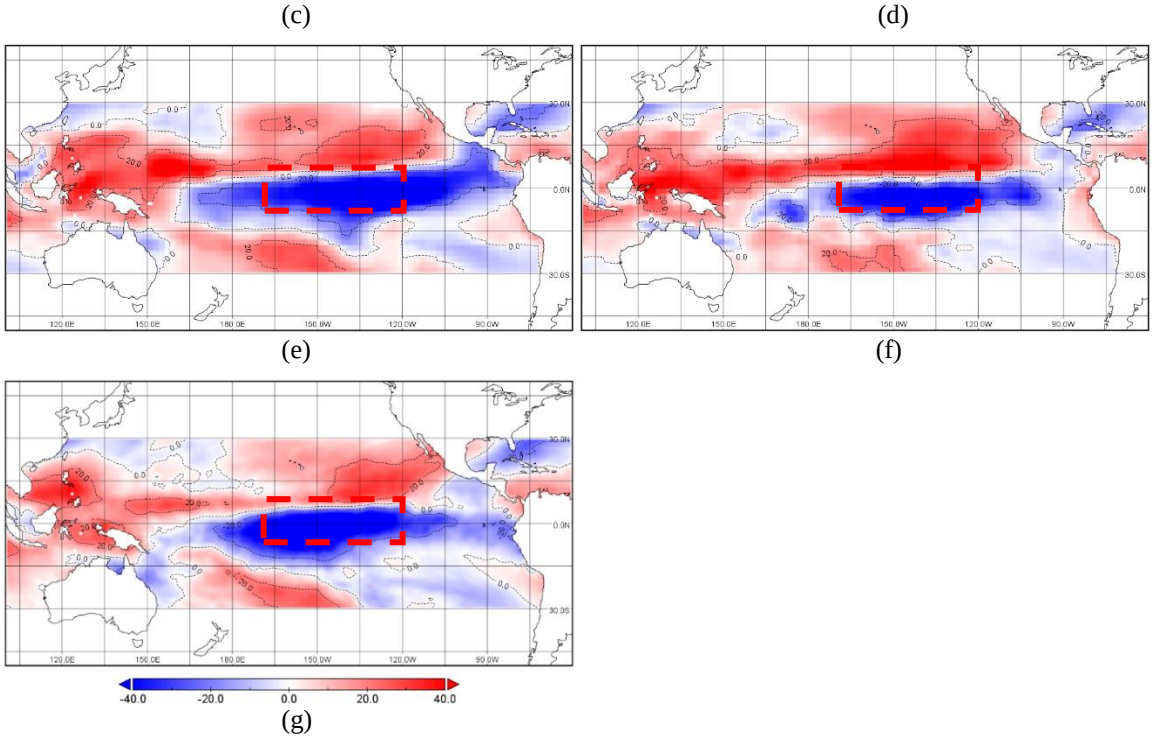

Figure 2-22 Three-month running mean of OLR anomalies of a peak El Niño period (December 1997) within the central Pacific region (30°N–30°S, 100°E–60°W). OLR data are from a) JRA-25, b) JRA-55, c) ERA-Interim, d) MERRA, e) NCEP-NCAR, f) NCEP-DOE, g) NCEP-CFSR, respectively. The red boxes mark the Niño 3.4 region. Unit: W/m^2.

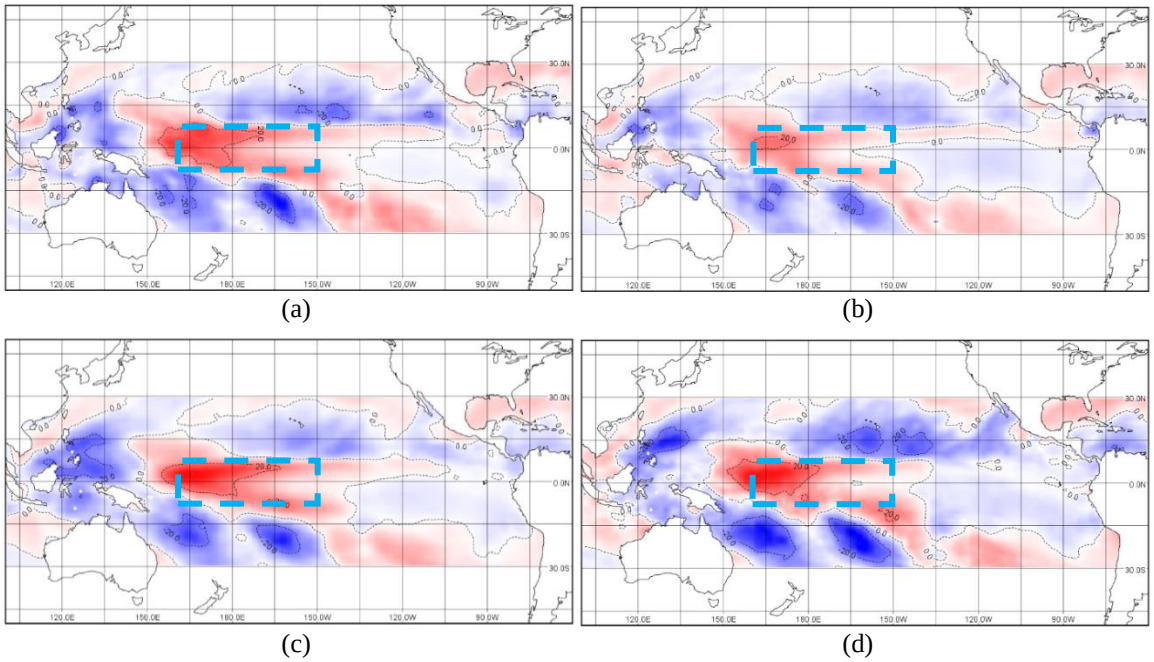

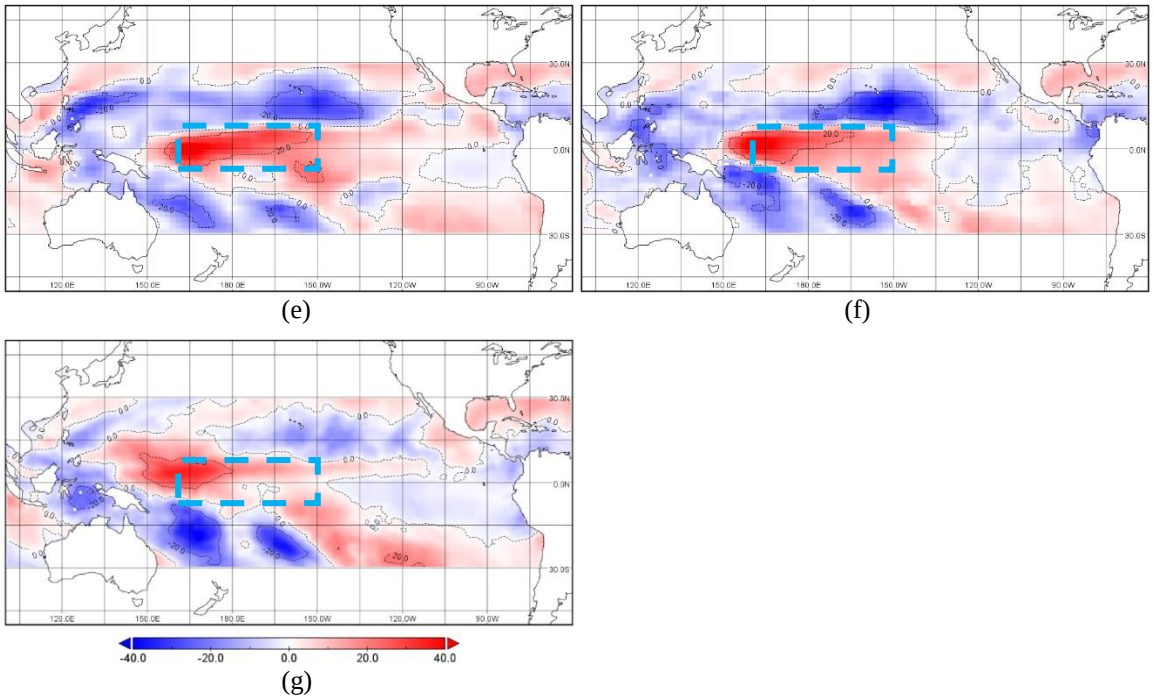

Figure 2-23 Three-month running mean of OLR anomalies of a peak La Niña period (December 1988) within the central Pacific region (30°N–30°S, 100E°–60°W). OLR data are from a) JRA-25, b) JRA-55, c) ERA-Interim, d) MERRA, e) NCEP-NCAR, f) NCEP-DOE, g) NCEP-CFSR, respectively. The blue boxes mark the Niño 4 region. Unit: W/m^2.

It is apparent that, though the magnitude of the response varies, all reanalysis OLR datasets can capture the selected El Niño and La Niña events. To explore their capability in capturing ENSO cycles in long-time series, correlation analysis between ONI_{SST} and ONI_{OLR} was also conducted. Figure 3-23 plots the variations of ONI_{SST} in the Niño 3.4 (Figure 3-23a) and Niño 4 (Figure 3-23b) regions from 1979 to 2016. With the threshold of +0.5°C (-0.5°C) employed, the El Niño (La Niña) cycles can be clearly identified. Similarly, the time-series of ONI_{OLR} from the reanalysis dataset (taking NCEP-NCAR as an example) were also calculated for the two Niño regions and are shown in Figure 2-24a and Figure 2-24b. It is evident that the temporal changes of ONI_{SST} and ONI_{OLR} are strongly and negatively correlated (R = -0.87 in Niño 3.4; R = -0.83 in Niño 4). More details are illustrated in Figure 2-24c and Figure 2-24d, by separating the [ONI_{SST}, ONI_{OLR}] pairs into

four zones corresponding to the four quadrants in the Cartesian coordinate system. In Niño 3.4 (Figure 2-24c), the negative correlation of data in quadrant IV (R_w = -0.9) is much stronger than that of quadrant II (R_c = -0.43). Considering that a positive ONI_{SST} indicates the occurrence of El Niño, the results clearly indicate that ONI_{OLR} can capture El Niño fairly well in Niño 3.4, but performs much worse in capturing La Niña. In addition, the data located in quadrant I denote the months determined as El Niño or pre-El Niño by ONI_{SST} but missed by ONI_{OLR}. Because ONI_{SST} is considered as the reference in the comparison, these points can be counted for an indication of the omission error of ONI_{OLR}. Then, quadrant III contributes to the omission error following the same analogy. In Niño 4 (Figure 2-24d), although ONI_{OLR} correlates to El Niño more so than to La Niña, the absolute value of R_c increases to 0.59, which is higher than that in Niño 3.4 (0.43). In fact, these results support the claim that Niño 4 is better in capturing La Nina than Niño 3.4 as previously stated. Table 2-9 summarizes the statistics of all reanalysis datasets. In general, ONI_{OLR} has a much greater capability of capturing El Niño than it does of capturing La Niña, and among the seven reanalysis datasets, NCEP-NCAR performs the best in capturing both El Niño and La Niña.

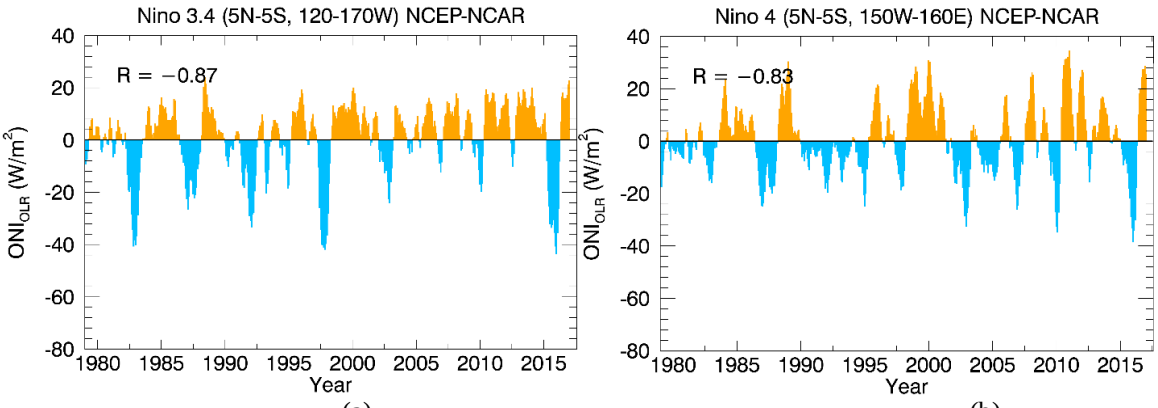

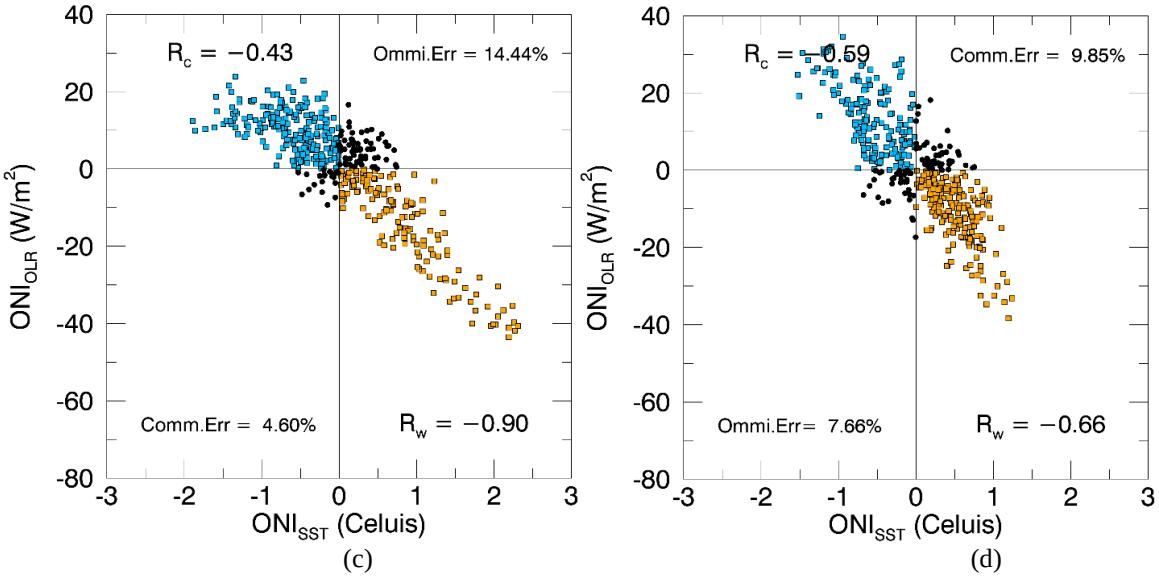

Figure 2-24 Long-time series (1979–2016) of the spatially averaged ONI_{OLR} for the a) Niño 3.4 and b) Niño 4 regions from the NCEP-NCAR reanalysis dataset. Relationship between ONI_{OLR} and ONI_{SST} is shown in c) and d) for the Niño 3 and Niño 4 regions, respectively.

Table 2-9 Statistics of the long-time series comparison between ONI_{OLR} calculated from the seven reanalysis datasets and ONI_{SST} in the Niño 3.4 and Niño 4 regions, respectively.

	Niño 3.4			Niño 4		
	R (Overall)	R (El Niño)	Ommi.Err	R (Overall)	R (La Niña)	Ommi.Err
JRA-25	-0.71	-0.87	24.07%	-0.68	-0.49	9.17%
JRA-55	-0.64	-0.79	23.04%	-0.74	-0.51	6.65%
ERA-Interim	-0.68	-0.77	24.94%	-0.73	-0.57	5.38%
MERRA	-0.66	-0.78	25.84%	-0.75	-0.52	3.6%
NCEP-NCAR	-0.87	-0.90	14.44%	-0.83	-0.59	7.66%
NCEP-DOE	-0.76	-0.84	17.29%	-0.69	-0.41	10.07%
NCEP-CFSR	-0.70	-0.81	20.57%	-0.72	-0.42	5.91%

2.4 Conclusions and discussions

This Chapter conducted comprehensive inter-comparisons and evaluations on multiple satellite and reanalysis OLR products. The objective is to quantify the inconsistences and uncertainties existing among them due to different retrieval approaches, different spatial resolutions and coverages, and so on. Four satellite-retrieved OLR

products (HIRS, GEWEX-SRB, AIRS, CM-SAF) and seven reanalysis OLR datasets (JRA-25, JRA-55, ERA-Interim, MERRA, NCEP-CAR, NCEP-DOE, and NCEP-CFSR) were inter-compared and evaluated in aspects of discrepancies from CERES EBAF monthly OLR products, spatial distribution, seasonal variation, and their capability of monitoring tropical expansion and capturing the ENSO cycles. Findings can be summarized as follows:

For satellite OLR, 1) Climatology comparison demonstrate that all the four examined OLR products are highly correlated with the CERES EBAF OLR product (R^2>0.94), indicating that those products are able to capture the OLR spatial contrast; 2) The HIRS OLR product has the best agreement with CERES in general, with absolute bias = -1.11 W/m^2 (1.86 W/m^2) and RMSD =4.21 W/m^2 (3.01 W/m^2) in DJF and JJA seasons, respectively, and almost no dependence on surface types or latitudes; 3) the biases of these OLR products against CERES show almost no variation across seasons over oceans but much larger seasonal differences over lands mainly contributed by the surface temperature differences on polar regions across seasons; 4) All the OLR products can effectively monitor the systematic poleward tropical expansion in the north hemisphere during 1979 to 2016, with the largest decadal expansion rate in JJA, and HIRS and SRB can also well characterize the tropical expansion in the SH. Globally, all products can quantify the tropical expansion; 5) All OLR products exhibited significantly negative monthly anomalies during an El Niño event, and the opposite during a La Niña event. This is attributed to the enhancement of atmospheric convection that leads to more cloud cover and higher and cooler cloud top temperatures during El Niño, and vice versa during La Niña. Long-time series comparisons between an OLR-composed index (i.e., three-months

running mean OLR anomalies) and the SST based ONI suggested that satellite-retrieved OLRs were competent at identifying ENSO cycles. HIRS outperformed the others, with correlation coefficients of -0.81 for both El Niño La Niña.

For reanalysis OLR, 1) Both climatology and long-term series comparisons indicate that the JRA-25 and JRA-55 OLR products are greater than CERES OLR by up to ~15 W/m^2 and ~12 W/m^2, respectively. For TOA longwave radiation, such biases are too large to be compatible within climatic models. NCEP-NCAR achieved the highest agreement with CERES OLR overall, showing very slight disagreement (~-1 W/m^2). However, the relatively large RMSD (~9 W/m^2) obtained in the global OLR climatology comparison implies that the OLR difference between NCEP-NCAR and CERES has a relatively large spatial variation. 2) In general, OLR biases from all the reanalysis datasets display latitudinal dependencies in the case of either negative or positive biases: tropical areas (at a higher OLR level) have larger absolute differences while middle- and high-latitude areas (at a lower OLR level) agree better with CERES. 3) Global OLR climatology comparisons report that the correlation coefficients between CERES OLR and reanalysis OLR are very high, suggesting that all the reanalysis OLR products can capture the OLR spatial contrast as well as CERES. 4) All reanalysis OLR values monitored systematic poleward tropical expansion in the NH during 1979 to 2016, with JJA season showing the largest decadal expansion rate; while almost no significant expansionary trend could be detected in the SH. 5) All reanalysis OLR values showed significantly negative monthly anomalies during an El Niño event, and the opposite during a La Niña event. Long-time series comparisons between an OLR-composed index and the SST-based ONI suggested that reanalysis OLR

values were competent at identifying ENSO cycles. NCEP-NCAR outperformed the others, with correlation coefficients of -0.9 for El Niño and -0.59 for La Niña.

The OLR values from JRA-25 and JRA-55 are larger than that from CERES by more than 10 W/m^2, which is unacceptable for climatic studies. The longwave radiation schemes employed in these two projects may need to be revisited. Moreover, further efforts are required for global OLR studies, in terms of collecting more highly accurate satellite OLR products for validation, and evaluating both satellite retrieval and reanalysis OLR using more extreme climatic events such as hurricanes as well as forest fires, extensive urbanization, etc. Because OLR presented capabilities in capturing ENSO cycles, we will investigate its potential to provide accurate prediction of ENSO in a future study.

Chapter 3 Algorithm development for OLR estimation from multi-spectral satellite data

In Chapter 2, inconsistencies and uncertainties are clearly observed among those existing OLR products. In this chapter, an algorithm framework will be developed to explore if the higher spatial resolution and multi-spectral satellite data can yield more accurate OLR estimates. Since the remote sensing era, OLR is obtained from satellite instruments in the form of either broadband or narrowband (bandwidth within 1 μm) radiometers (Park et al., 2015). Broadband radiometers provide direct/nearly direct observations of the emission of OLR by measuring radiances over the whole thermal spectral range. Two typical broadband radiometers are ERBE from 1985–1999 and the CERES from 2000 to the present day. The primary instantaneous OLR retrieval from CERES is based on the ADM model (Loeb et al., 2003b), which constructs the relationship between OLR and radiances received at different satellite zenith angels under various surface and atmospheric conditions. With respect to narrowband radiometers, the basic idea is to establish the quantitative relationships between OLR and narrowband radiances with extensive training samples. Two typical OLR products from the narrowband sensors are the HIRS OLR (Lee and Ellingson, 2013; Lee et al., 2007) from NOAA CDR program and Atmospheric Infrared Sounder (AIRS) OLR developed in Sun et al. (2010). Similar approach was also employed to produce OLR datasets for the GOES Sounder (Ba et al., 2003), GOES Imager (Lee et al., 2004), and GOES-R ABI (Lee et al., 2010). As the most widely used multi-spectral data in the past nineteen years, MODIS has no operational OLR product so far, thus it is necessary to dig out the potential of MODIS on the more robust OLR estimation. In addition, AVHRR is another popular resource that covers a long period

beyond 35 years. However, current AVHRR OLR products archived in NOAA (Liebmann and Smith, 1996b) has a too coarse resolution (2.5°) to meet the requirements of some medium/high resolution (down to 1 km) numerical weather prediction models in recent years (Christensen et al., 1998; Guan et al., 2000; Soci et al., 2006). Thanks to the NOAA Land Long-term Data Record (LTDR) program, we have a good opportunity to generate a long-term record of AVHRR OLR datasets with a resolution of 0.05° and with higher data quality.

This chapter will first develop the algorithm framework for estimating OLR from multi-spectral satellite data based on RT simulation. MODIS and AVHRR data are used to demonstrate the algorithm effectiveness, and CERES OLR products are collected as reference data to evaluate the algorithm performance and the generated OLR data.

3.1 Datasets

3.1.1 MODIS TOA radiance

MODIS provides the opportunity to estimate OLR by utilizing multi-channel spectral information at 1 km spatial resolution. The sensor has 16 thermal infrared (TIR) channels ranging from 3.660 to 14.385 μm (Barnes et al., 1998) (see Table 3-1). The spectral response function (SRF) of the sensor can be seen in Figure 3-1. The two MODIS sensors can potentially provide at least four daily observations over most locations on the Earth's surface with more observations available at high latitudes. The MODIS local overpass times are 10:30 am and 10:30 pm (*Terra*) versus 1:30 pm and 1:30 am (*Aqua*). The higher spatial and spectral resolution of the MODIS data may enable more accurate

derivation of OLR owing to that it provides more detailed information about the atmosphere and land surface than the sensors with a coarser resolution.

Table 3-1 MODIS thermal infrared channels

Channel	Bandwidth (μm)	Primary use
20	3.660–3.840	Surface temperature
21	3.929–3.989	
22	3.929–3.989	
23	4.020–4.080	
24	4.433–4.498	Temperature profile
25	4.482–4.549	
27	6.535–6.895	Moisture profile
28	7.175–7.475	
29	8.400–8.700	
30	9.580–9.880	Ozone
31	10.780–11.280	Surface temperature
32	11.770–12.270	
33	13.185–13.485	Temperature profile
34	13.485–13.785	
35	13.785–14.085	
36	14.085–14.385	

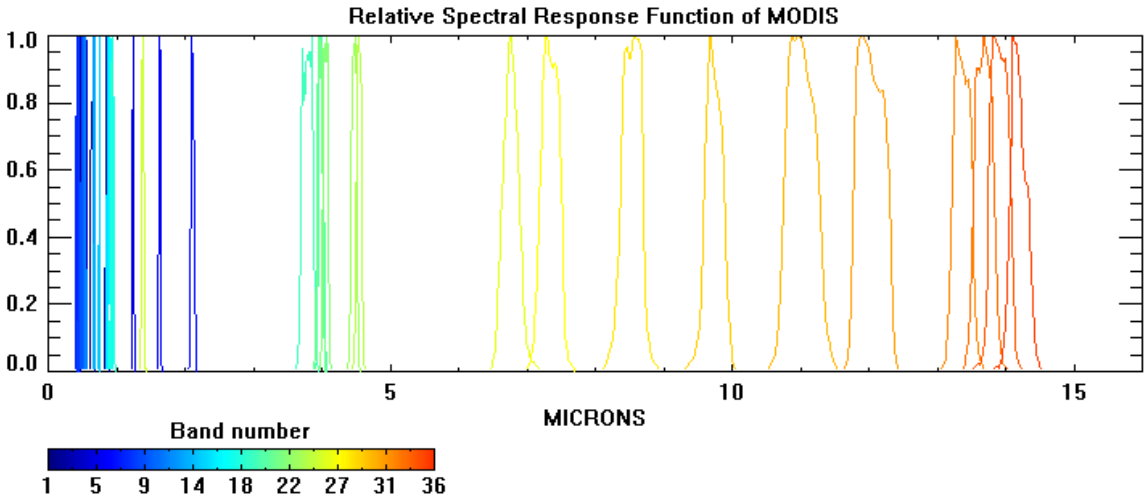

Figure 3-1 The relative spectral response function of MODIS

3.1.2 AVHRR TOA radiance

The AVHRR is a cross-track scanning system onboard the NOAA family of polar-orbiting platforms (POES) with five spectral bands with a resolution of 1.1 km. The latter three channels sample the thermal radiation emitted by the planet, that is, ~3.7 μm, 11 μm, and 12 μm, respectively (the last channel is unavailable on NOAA-6, NOAA-8, and NOAA-10), on afternoon NOAA satellites. The AVHRR has proven to be useful for several other applications and particularly relevant to study climate change and environmental degradation because of the comparatively long records of data already accumulated. It is able to obtain long-term OLR data, which will be unique resources for investigations of the Earth energy balance up to 35 years. In this chapter, the AVHRR TOA radiance (AVH02C1) was obtained from the most recent version (V4) of the NOAA LTDR (http://ltdr.nascom.nasa.gov/) project. The LTDR project has produced a consistent dataset based on Global Area Coverage (GAC) data from the AVHRR sensors at a spatial resolution of 0.05° from 1981 to the present (Pedelty et al., 2007). Due to the lack of on-board calibration system and inconsistencies of the inter-calibration among successive NOAA satellites series, LTDR has applied the invariant target calibration based on radiative transfer model (Franch et al., 2017; Vermote and Kaufman, 1995; Vermote and Saleous, 2006) and demonstrated a calibration accuracy within 1% compared to MODIS (Vermote and Saleous, 2006). In addition, to account for the orbital drift issue, LTDR employed a clock correction approach (Evans et al., 2010) for geolocation correction and the results achieved an geolocation accuracy better than two pixels (Song et al., 2018). In this study, the brightness temperature of the three thermal channels (Table 3-2) included in AVH02C1 was used for the estimation of the OLR. The SRF of AVHRR (onboard NOAA-

7 for example) is shown in Figure 3-2. All data of the LTDR are from the afternoon constellation satellites NOAA-07, NOAA-09, NOAA-11, NOAA-14, NOAA-16, NOAA-18, and NOAA-19. Based on the cloud mask information included in AVH02C1, clear-sky and cloudy-sky models can be applied to real AVHRR images, respectively.

Table 3-2 AVHRR thermal infrared channels

Channel	Bandwidth (μm)
BT_CH3	3.55–3.93
BT_CH4	10.3–11.3
BT_CH5	11.5–12.5

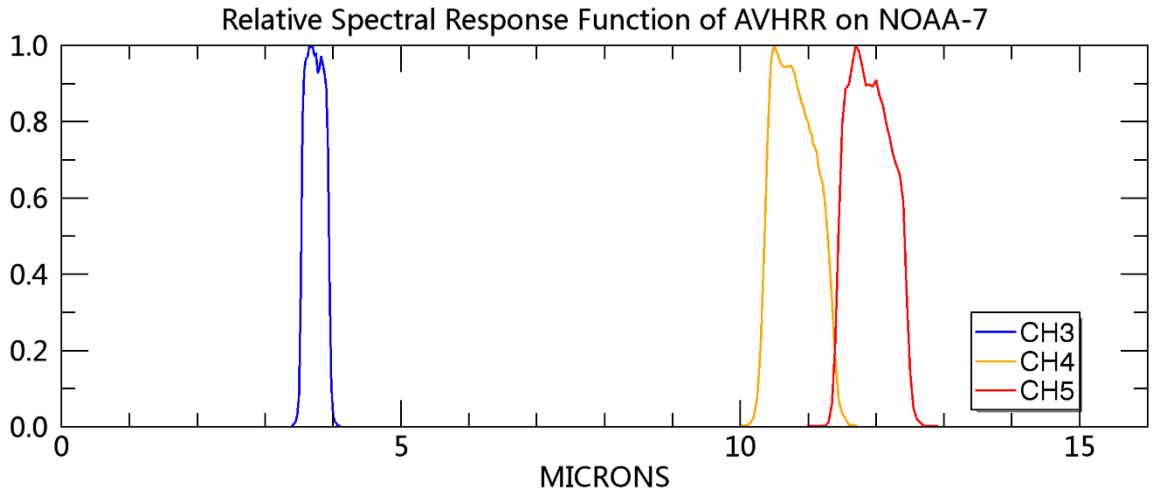

Figure 3-2 The relative spectral response function of AVHRR on NOAA-7 platform

3.1.3 CERES OLR product

In section 2.1.1.1, the basic characteristics of CERES OLR products have been introduced. In this chapter, three types of CERES OLR products were also utilized for different purposes: 1) CERES level-2 Single Scanner Footprint (SSF) OLR products were collected for comparison with the instantaneous OLR retrievals. The SSF datasets provide instantaneous CERES OLR estimates at 20 km resolution based on the ADM proposed by Loeb et al. (2005). 2) CERES SYN1deg products (Doelling et al., 2013) were collected to

construct the instantaneous-to-daily-mean conversion model for daily-mean OLR calculation. The SYN1deg uses 3-hourly geostationary radiances and cloud properties to model the diurnal variability between CERES observations. Edition 3A of this product combined the fluxes and cloud retrievals observed by *Terra* and *Aqua* CERES, providing 3-hourly regional means of the CERES GEO-enhanced temporally interpolated TOA fluxes (SYN1deg-3Hour) and daily mean TOA fluxes (SYN1deg-Day). In this study, the observed TOA fluxes from CERES and geostationary derived fluxes were used. 3) The newest edition of CERES OLR, Energy Balanced and Filled (EBAF) TOA monthly flux products, were collected as the reference data to validate the OLR calculation at monthly mean level. EBAF products conduct adjustment to both TOA shortwave flux and OLR to ensure that global mean net TOA flux for July 2005–June 2015 is consistent with the in situ value of 0.71 W/m^2 (Loeb et al., 2018).

3.1.4 HIRS OLR product

Basic characteristic of HIRS OLR product has been introduced in section 2.1.1.2. In this chapter, both daily and monthly mean HIRS OLR from 1979 to 2016 were collected from NOAA NCDC.

3.1.5 NOAA temporally interpolated AVHRR OLR product

Existing NOAA OLR products were also collected as another reference data for comparisons and evaluations. The NOAA Physical Science Division (PSD) (https://www.esrl.noaa.gov/psd/data/gridded/data.interp_OLR.html) provides long-term monthly OLR record at 2.5° × 2.5° resolution from 1974 to 2016 based on NOAA series satellites (Liebmann and Smith, 1996b). The radiances recorded with by the 10 μm window

channel, which is primarily sensitive to the temperature of the surface or cloud top, were converted to broadband fluxes based on theoretical model calculations (Abel and Gruber, 1979). The original OLR retrieval was further improved by filling gaps by temporal and spatial interpolation based on algorithms described in Liebmann and Smith (1996b). During the operational stage, the uninterpolated OLR data were obtained from the archive of the NOAA National Center for Atmospheric Research (NCAR; at present, directly from NOAA NESDIS) and then interpolated OLR was produced accordingly. As of March 1999, the pixel data were put into a 1° × 1° grid at NOAA's Climate Prediction Center (CPC) and then interpolated to the 2.5°×2.5° grid of the current datasets.

3.2 Methodology

3.2.1 Instantaneous OLR estimation

Instantaneous OLR is the primary estimate in this chapter and the basis of the daily mean OLR calculation. The OLR is the radiant energy emitted by the Earth–atmosphere system per unit area and thus the key step in estimating the OLR is to convert the observed TOA longwave radiance into the TOA longwave flux. For broadband observation data, as mentioned earlier, the typical method is to establish an ADM, which is a set of anisotropic factors (R) that determine the quantitative relationship between OLR and the observed TOA radiance at specific satellite viewing angles and surface–atmosphere conditions. In fact, ADM has been employed as the standard model to retrieve instantaneous OLR of CERES products (Loeb et al., 2005; Loeb et al., 2007; Loeb et al., 2003b). For multispectral observation data, an initial attempt has ever been carried out to calculate the spectral OLR using the ADM-like approach and then converted the narrowband flux into broadband OLR

through statistical approaches. However, the scene-type definition (Loeb et al., 2005) of ADM varies among different spectral bands and the estimation bias of each ADM and narrowband-to-broadband conversion model propagate and accumulate in the final OLR retrieval. Another feasible way is to directly link the OLR with observed TOA radiance through statistical modeling. This method involves two training datasets obtained from radiative transfer (RT) simulation: broadband OLR and TOA radiance simulated for each spectral channel. This idea is rooted in the direct estimation method and has been applied extensively to estimate a variety of land variables (Liang, 2003; Wang and Liang, 2016; Wang et al., 2013; Wang and Liang, 2009; Wang et al., 2009).

Figure 3-3 illustrates the procedures to obtain the look-up-table (LUT) of regression coefficients that quantitatively link the AVHRR TOA radiance to the instantaneous broadband OLR. The MODTRAN 5 model was used in this study to simulate the training datasets for the derivation of OLR regression models. This radiative transfer model has been widely used in the scientific community to calculate the transmission and emission of the atmosphere and surface in the optical to sub-mm wavelength range (Liang, 2003; Wang and Liang, 2016; Wang et al., 2013; Wang and Liang, 2009; Wang et al., 2009). It provides various standard atmospheric models and also allows user-defined atmospheric profiles (Berk et al., 2006). In the current study, two datasets were obtained from MODTRAN 5: the TOA broadband (4–100 μm) OLR and spectral radiance of the three AVHRR thermal channels based on their SRFs.

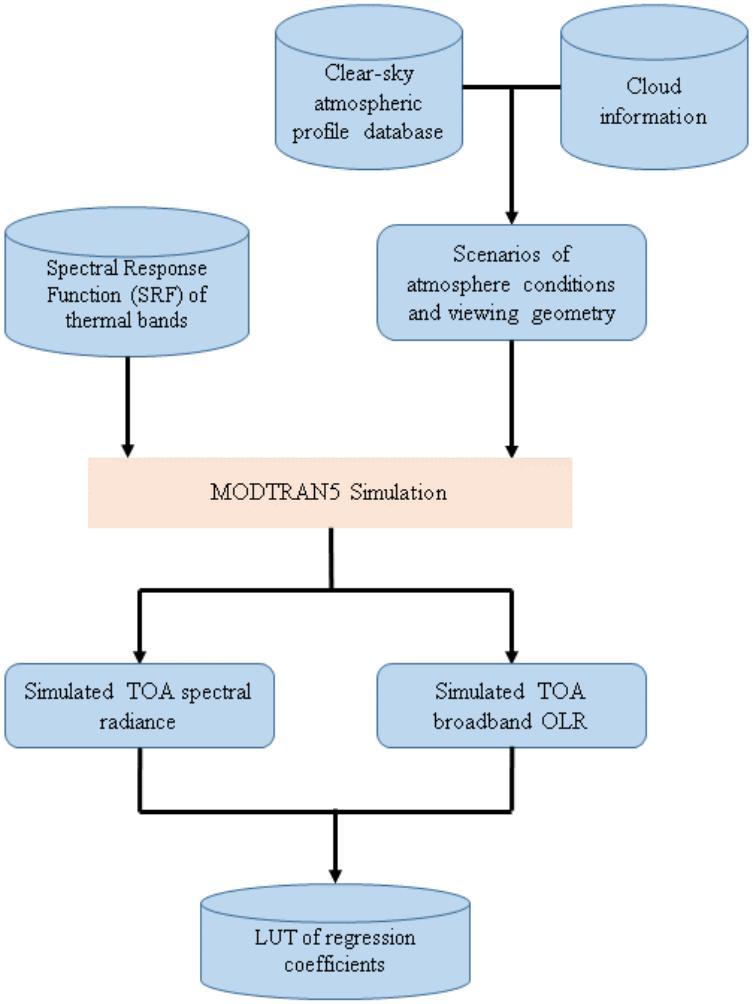

Figure 3-3 Procedures to generate the look-up-table (LUT) of regression coefficients between AVHRR TOA radiance and broadband OLR

For the purpose of the RT simulation, the atmosphere conditions and solar/viewing geometry are the key parameters to be set in advance. Under clear-sky conditions, the surface temperature and water vapor in the atmosphere are two dominants factors controlling the OLR, while cloud radiative and physical properties significantly contribute to OLR under cloudy-sky conditions. In addition, the TOA flux is the radiant energy emitted by the Earth–atmosphere per unit area based on which the relationship between the flux and observed radiance highly depends on the solar and viewing geometry. Accordingly, the MODTRAN5 simulations were performed in separate scenarios defined by different

combinations of sky conditions (clear and cloudy) and satellite view zenith angels (VZA; 0°–75° with 1° increments). It should be noted that the OLR is irrelevant to solar illumination and thus only VZA was taken into account. For clear-sky conditions, the SeeBor V5.0 database (Borbas et al., 2005) was used in this study. The SeeBor is the clear-sky global training database for hyperspectral and multispectral atmospheric retrievals. More than 15000 global profiles are included in this database, which contains information about the temperature, moisture, and ozone at 101 pressure levels (ranging from 0.005hPa to 1100.00hPa) obtained from NOAA-88, ECMWF, TIGR-3, ozonesondes, and desert radiosondes. To ensure the physical consistency near the top of the troposphere, a preprocessing technique was implemented to extend the temperature, moisture, and ozone profiles above the level of existing data. Physically based characterizations of the surface skin temperature and surface emissivity were assigned to each profile in the dataset (Borbas et al., 2005). For the cloudy-sky conditions, additional cloud parameters were separately set based on the clear-sky profiles. The Level-2 MODIS Cloud Product (MOD06_L2 for *Terra* and MYD06_L2 for *Aqua*) was used for this purpose. This product combines infrared and visible techniques to determine both physical and radiative cloud properties. For OLR simulations specifically, five parameters, including the optical thickness of cloud layers, cloud drop effective radius, cloud top temperature, cloud top height, and cloud top effective emissivity, were used; a Lambertian surface was assumed.

Based on the broadband OLR and TOA spectral radiance simulations, statistical analysis was conducted to fit quantitative models to these two datasets. In this study, a multiple linear regression model (Equation 3-1) was utilized:

$$F_{OLR} = a_0 + \sum a_i L_i$$

Equation 3-1

where a_0 and a_i are regression coefficients and L_i is the AVHRR TOA radiance at the *i*th thermal channel ($W/m^2/\mu m/sr$).

3.2.2 Daily-mean OLR estimation

Due to the diurnal variation of the Earth surface temperature and atmospheric conditions, it is hard to capture the general TOA radiation budget for a whole day based on the instantaneous OLR retrieval. In the climate community, the temporally averaged flux is always required for global energy budget characterization and time series analysis on a large scale; therefore, this study also attempts to develop an algorithm for the estimation of the daily mean OLR. Based on the instantaneous retrieval, the daily mean OLR can be calculated if the quantitative relationship between the daily mean and instantaneous OLR is obtained. However, for the sensors onboard sun-synchronous polar-orbiting satellites, it is almost impossible to construct OLR diurnal curves with limited samples for most areas on Earth. Due to this fact, time series of CERES OLR products were collected as auxiliary data to aid the daily mean OLR estimation. Figure 3-4 illustrates the procedures to estimate daily mean OLR based on the instantaneous OLR retrieval and CERES OLR products. First, both the CERES 3-hourly OLR product (SYN1deg-3Hour) and CERES daily mean OLR product (SYN1deg-Day) with the same spatial resolution (1° × 1°) from 2000 to 2016 were collected. Local time (LT) of each grid in the CERES SYN1deg-3Hour product was firstly calculated based on the given Greenwich Mean Time (GMT) and the longitude of the target grid. For a specific time (0:00, 3:00, 6:00, …, 18:00, 21:00 local time zone) on a specific day of the year (*DOY*: 001, 002, … , 364, 365), seventeen pairs (one pair for one year from 2000 to 2016) of instantaneous CERES and daily mean OLR data could be

extracted. Linear fits of those pairs were then established based on the least-square method. Finally, these linear models were applied to the instantaneous OLR retrieval to estimate the daily mean OLR. Considering that eight models could be obtained on a single day, 2920 were fitted and archived based on each pixel. In the case that the spatial resolution of instantaneous OLR is different with the CERES 1-degree data, pixels located on the same grid of CERES 1-degree data share the same fitted model. Figure 3-5 presents examples of the fitting models mentioned above for four different surfaces. It is notable that linear models perform quite well in linking the instantaneous CERES OLR to daily mean OLR and can explain up to 97% of the variations between the two variables.

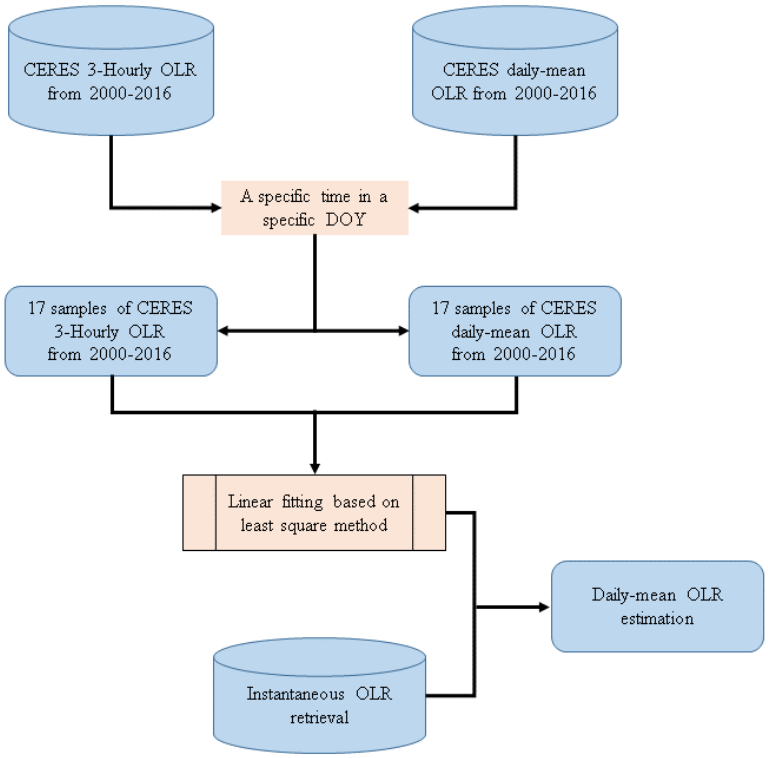

Figure 3-4 Procedures to estimate daily mean AVHRR OLR from instantaneous AVHRR OLR retrievals and CERES OLR products.

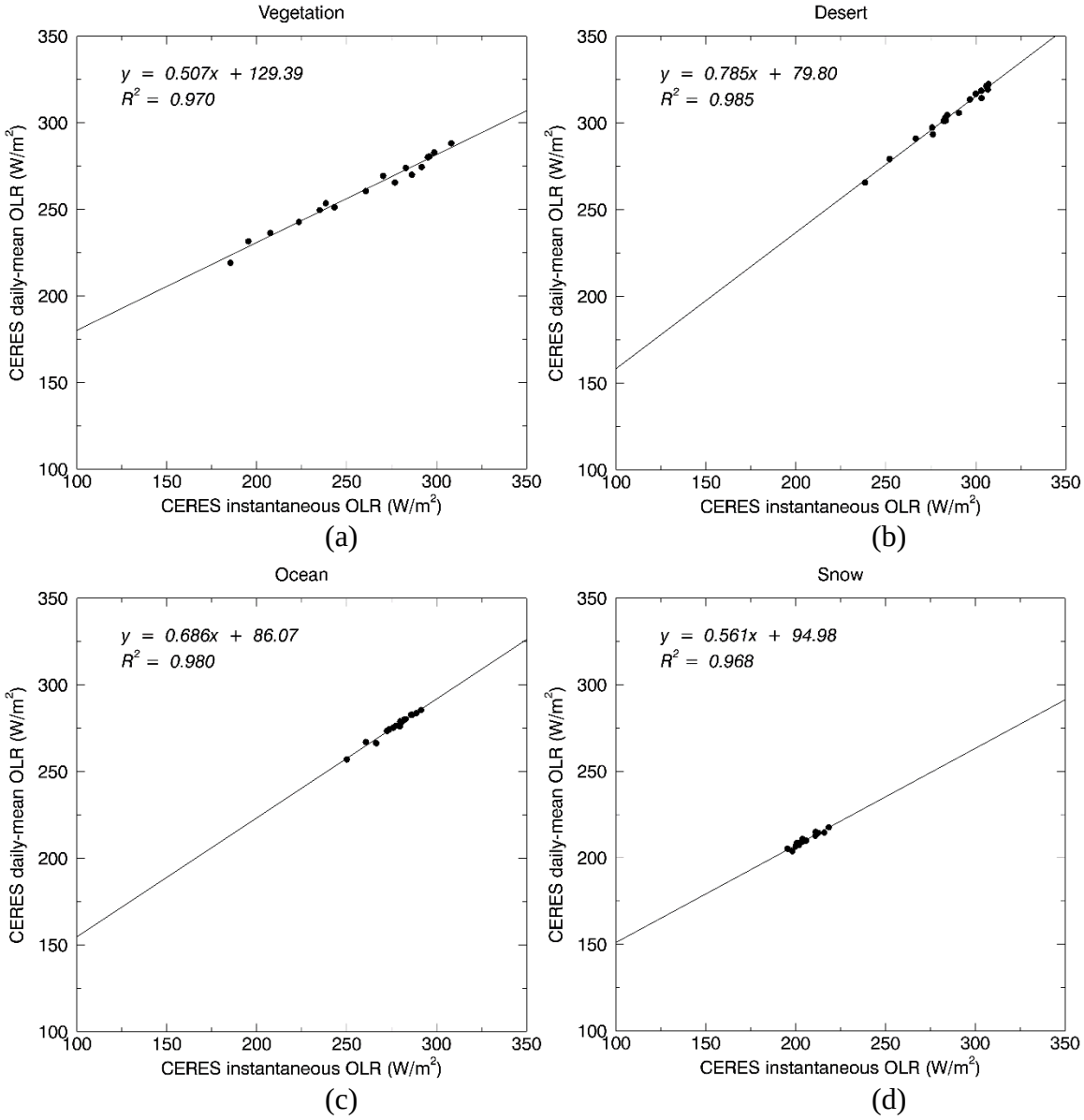

Figure 3-5 Linear fits between instantaneous CERES (12:00 local time) and daily mean OLR for pixels of a) vegetation, b) desert, c) ocean/water, and d) snow, respectively, for July 1 (DOY: 182)

3.3 Results and evaluation

3.3.1 Representative analysis of atmosphere profiles

For the radiative transfer-based approach, the representativeness of the atmosphere/cloud profiles is the key factor controlling the prediction ability of the models. In this study, ~15000 profiles of the SeeBor V5.0 database was included in the simulation.

Among those profiles, ~50% are located in oceans, followed by 35% for vegetated surfaces, 5% for barren/desert land, and 5% for snow/ice surfaces; the percentages are basically consistent with the proportions of geographical areas of those surface types on Earth. Figure 3-6 shows the details for two key parameters during the OLR simulation: surface temperature and emissivity. The global surface temperature ranges from 200 to 340 K for different surfaces and mainly clusters between 280 and 300 K; the emissivity spectra also show typical patterns for the corresponding surfaces. Consequently, the diversity of surface types, surface temperature, and emissivity involved in the simulation and training guaranteed the model performance. In addition, the viewing geometry is another key component during model establishment. Although finer VZA resolution in general leads to higher model fitting accuracy, the high computational burden is worth to be considered, especially in the operational stage. Therefore, the test was conducted in this study by varying the VZA interval from 15° to 0.5°; 1° is recommended based on the statistics in Table 3-3.

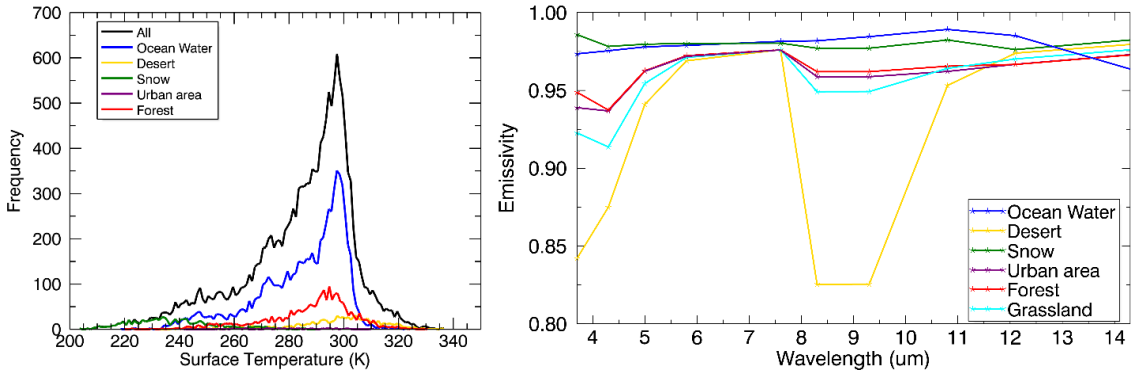

Figure 3-6 Surface temperature and emissivity of different surface types in the SeeBor V5.0 atmosphere profile database.

3.3.2 Model validation with simulated datasets

The instantaneous OLR from both MODIS and AVHRR was directly linked to TOA spectral radiances through linear models (Equation 3-1) that were fitted with the training data simulated from MODTRAN5. To evaluate the model fitting accuracy, comparisons were conducted between the simulated broadband OLR with that calculated from the fitted model. On one hand, a set of synthetic broadband OLR data could be directly output from the radiative transfer model and each one corresponded to a specific scenario defined by the combination of atmosphere profile and 75 VZA bins; on the other hand, MODTRAN5 also output synthetic spectral TOA radiances for each scenario and linear estimation models, along with the SRF of specific sensor, were applied to those TOA radiances to calculate the OLR. The computed OLR was then compared with the synthetic OLR to assess the prediction accuracy of the models. The OLR simulated from MODTRAN5 highly agreed with that calculated from the linear estimation model. In general, the estimation model is able to account for > 97% of the variation between the prediction and reference datasets for clear-sky conditions; the *RMSE* is as low as 0.1 W/m^2. The fitting accuracy under cloudy-sky conditions is slightly worse than that at clear-sky conditions. Moreover, to investigate the influence of the VZA resolution on the fitting accuracy, the model training procedures were repeated by setting different VZA intervals and then compared the model-predicted OLR with the simulated OLR in a similar way. Table 3-3 and Table 3-4 shows that R^2 decreases with the VZA interval for both clear- and cloudy-sky conditions from both MODIS and AVHRR sensors; the *RMSE* shows an opposite trend, suggesting that the linear estimation model performs better if a finer VZA resolution is used for the training process. However, an excessively dense VZA will lead

to a high computation burden, especially during the operational stage. To achieve a balance between accuracy and computation time, a VZA interval of 1° is recommended based on Table 3-3 and Table 3-4, considering that the accuracy improvement from 1° to 0.5° is rather small.

Table 3-3 Fitting accuracy of the instantaneous MODIS OLR estimation model for different VZA intervals

VZA interval	*Clear sky*		*Cloudy sky*	
	R^2	RMSE(W/m^2)	R^2	RMSE(W/m^2)
0.5°	0.99	0.10	0.96	0.11
1°	0.98	0.11	0.96	0.12
2°	0.98	0.11	0.96	0.12
5°	0.98	0.11	0.96	0.12
10°	0.97	0.12	0.95	0.13
15°	0.97	0.13	0.95	0.14

Table 3-4 Fitting accuracy of the instantaneous AVHRR OLR estimation model for different VZA intervals

VZA interval	*Clear sky*		*Cloudy sky*	
	R^2	RMSE (W/m^2)	R^2	RMSE (W/m^2)
0.5°	0.974	0.10	0.959	0.12
1°	0.972	0.10	0.956	0.13
2°	0.958	0.13	0.943	0.17
5°	0.931	0.15	0.922	0.19
10°	0.916	0.16	0.903	0.20
15°	0.900	0.18	0.887	0.22

Moreover, in order to justify the framework of RT simulation under cloudy condition, an independent experiment was conducted. The simulated data was employed associating with the HIRS SPF, and generated the coefficients for linking HIRS TOA spectral radiance to OLR. Then, four days of HIRS OLR under cloudy condition were

produced in Jan 1st, Apr 1st, Jul 1st, and Oct 1st, 2014 at the resolution of 1°. Such local HIRS OLR calculations were then compared against the existing HIRS daily OLR product (Lee and Ellingson, 2013; Lee et al., 2007), and results are shown in Figure 3-7. It is seen that the local calculation and the public product have quite good agreements with each other for all seasons (bias < 0.35 W/m^2, RMSE < 2.8 W/m^2), lending strong support to the hybrid model developed in this study for the OLR estimation.

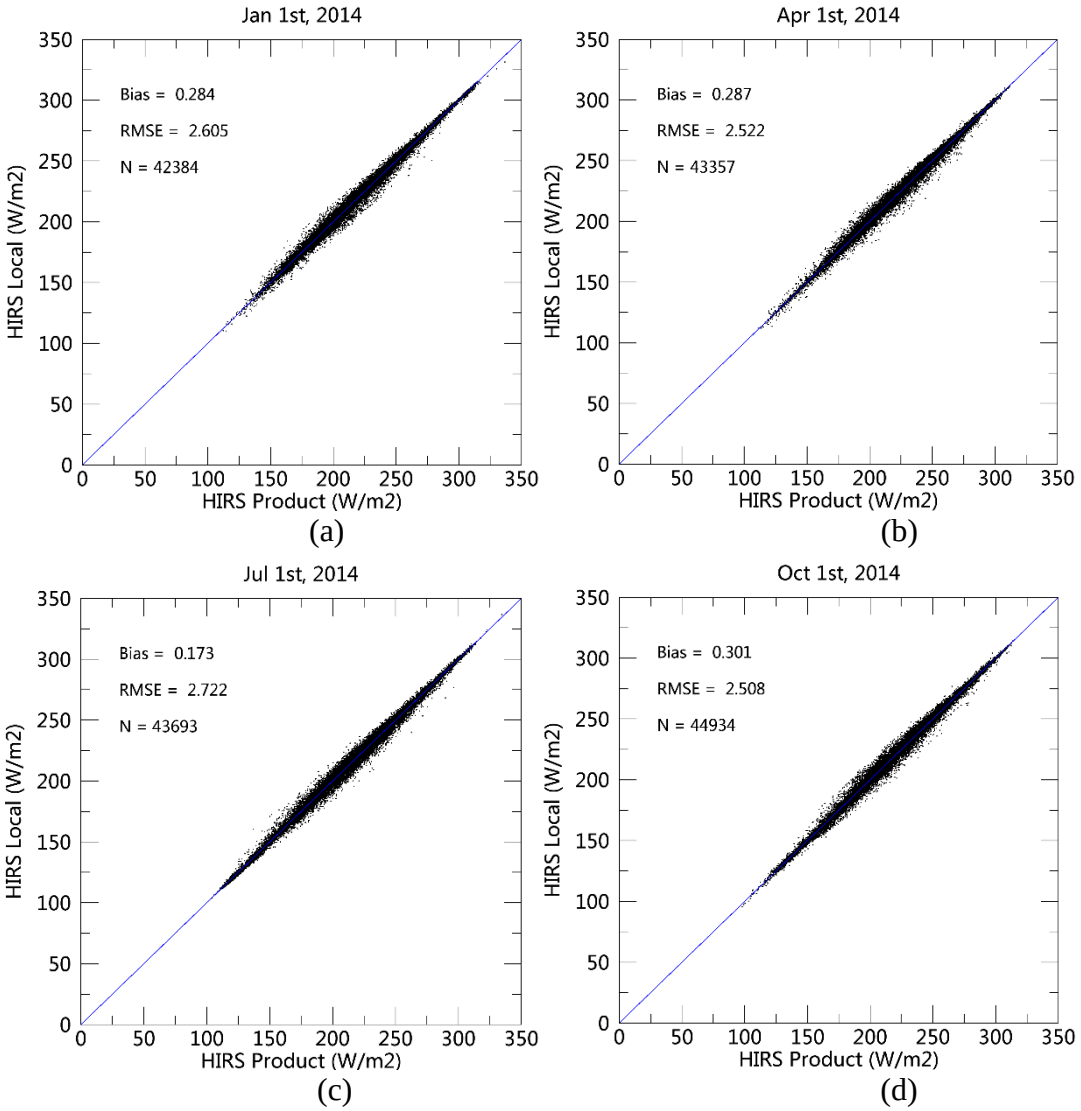

Figure 3-7 Comparisons between local calculated HIRS OLR and the published HIRS OLR product under cloudy condition in a) Jan 1st, b) Apr 1st, c) Jul 1st, and d) Oct 1st, in 2014, respectively.

3.3.3 Comparison with the existing OLR products

3.3.3.1 MODIS OLR

For the purpose of comparison, MODIS *Terra* and *Aqua* TOA radiance at 1-km resolution in the year 2013 and the co-located CERES instantaneous OLR were used. CERES SSF L2 datasets provide the CERES observed TOA fluxes, associated MODIS clouds and aerosol properties and GEOS-4 atmosphere at the instantaneous footprint level with 20-km spatial resolution at nadir. Accordingly, the MODIS 1-km retrievals were firstly aggregated within 20×20 window to match the CERES pixels. In addition, considering the similarity and difference in surface emissivity and surface skin temperature, comparisons are separately performed for four main land cover types, including desert, vegetated surface, snow cover, and water/ocean, respectively. Figure 3-10 and Figure 3-11 show the comparison results for these four land types under clear sky and all sky conditions, respectively. In general, the MODIS OLRs produced by the proposed linear OLR model are comparable with the CERES products for both sky conditions. Under clear-sky, MODIS prediction match CERES quite well, with *RMSE*s less than 3.5 W/m^2 and absolute biases less than 2 W/m^2; while under all-sky, the agreement with CERES slightly dropped but the *RMSE*s are still less than 9 W/m^2 and absolute biases less than 2 W/m^2. Among different surface types, snow covered surface achieves relatively higher agreement for both sky conditions between the two datasets likely due to its relatively stable thermal properties; the other three types display similar accuracies if the sky conditions are the same, but larger variation can be observed for all-sky condition than that of clear-sky condition.

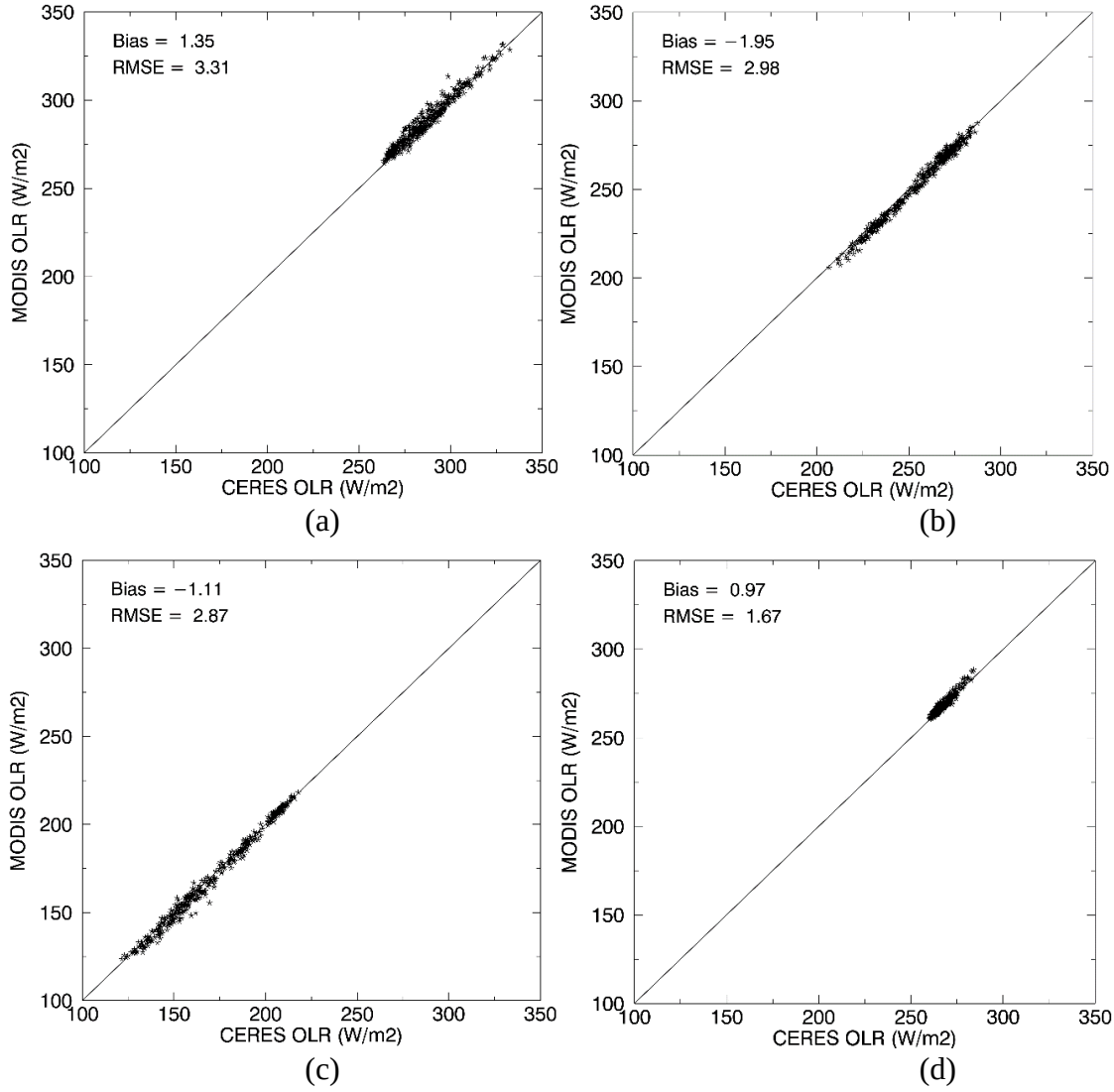

Figure 3-8 Comparisons between MODIS retrieved OLR and CERES OLR SSF product with 20-km resolution under clear-sky condition for a) desert; b) vegetated surface; c) snow cover; and d) water/ocean, respectively.

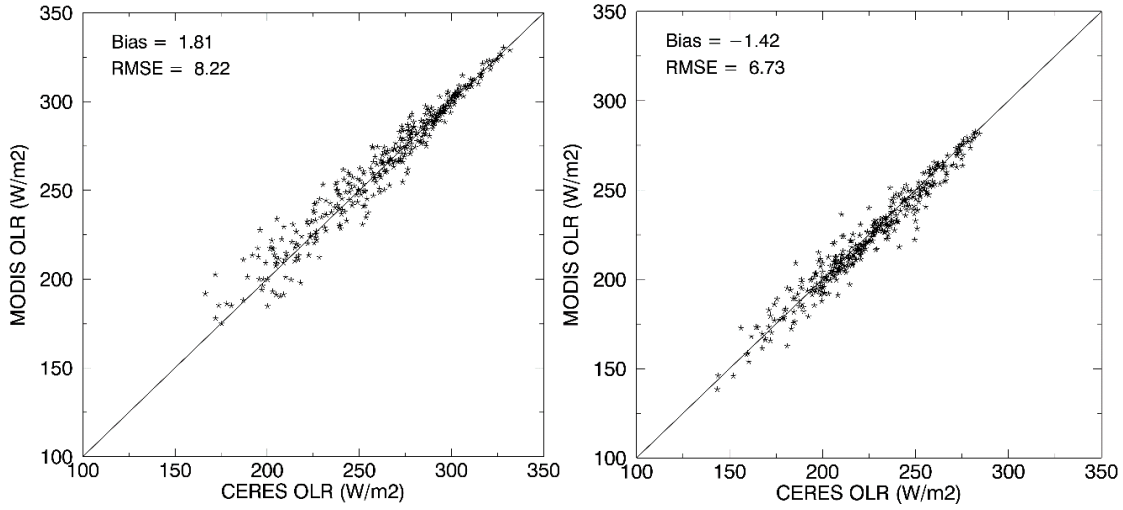

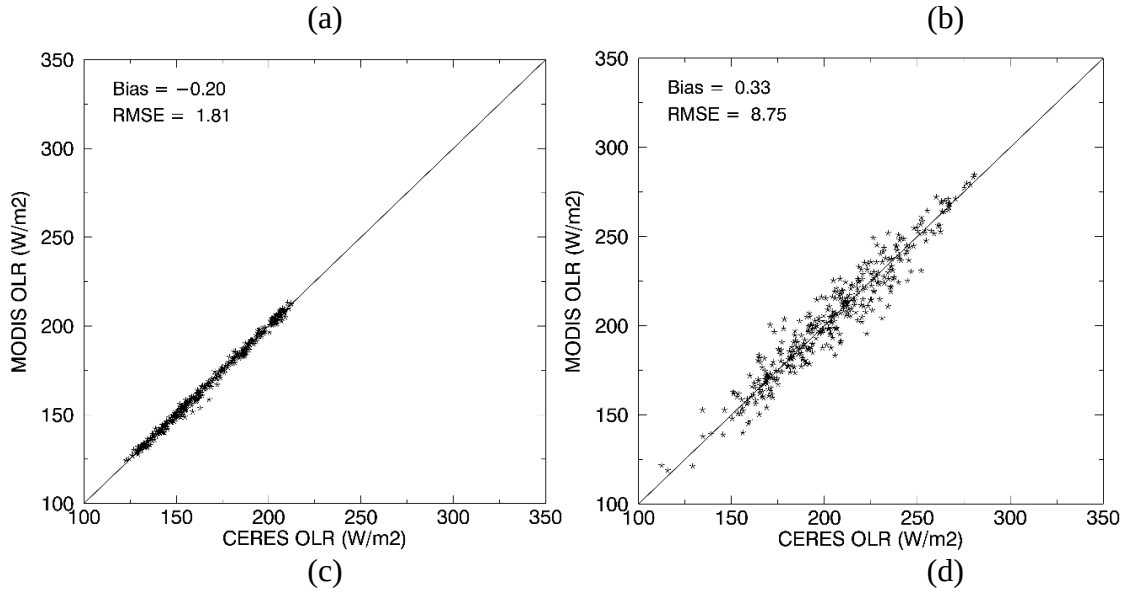

Figure 3-9 Comparisons between MODIS retrieved OLR and CERES OLR SSF product with 20-km resolution under all-sky condition for a) desert; b) vegetated surface; c) snow cover; and d) water/ocean, respectively.

Land surface temperature, as well as the cloud top temperature, are one of the main controlling factor of the OLR under clear and cloudy sky conditions, respectively. Thus, comparisons were also performed for different seasons (December–February (DJF), March–May (MAM), June–August (JJA), and September–November (SON)) between December 2012 and November 2013. Figure 3-10 and Figure 3-11 display the density scatter plots of the comparison results for those four seasons under clear and all sky conditions, respectively. It can be seen that for all seasons, MODIS OLRs agree with CERES OLR products at similar magnitude if the sky conditions are the same. In specific, under clear sky, the RMSEs are within the range of 2.5 W/m^2 to 3.5 W/m^2, and absolute biases are less than 0.15 W/m^2; while for all sky, RMSEs and biases are larger in all seasons, with values of about 6 W/m^2 and 0.2W/m^2, respectively. Results suggest that the proposed linear OLR model is robust for different periods throughout the year, and it achieves significant higher OLR estimation accuracy under clear sky condition that that of cloudy sky condition if the CERES OLR products are taken as the reference.

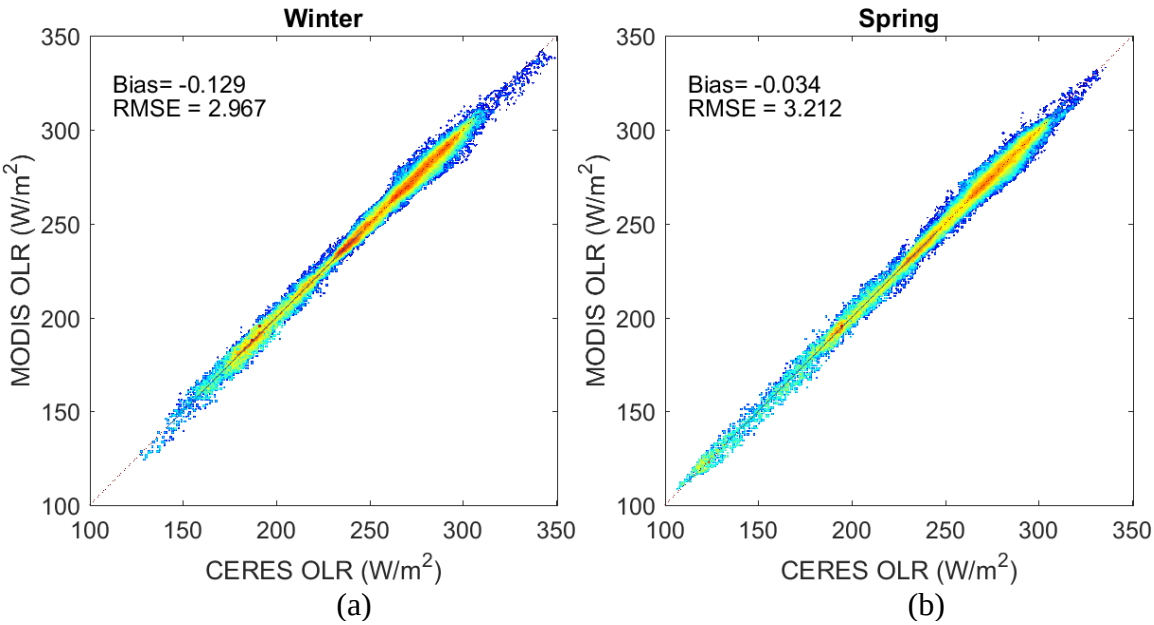

Figure 3-10 Comparisons between MODIS retrieved OLR and CERES OLR SSF product with 20-km resolution under clear-sky condition for a) DJF; b) MAM; c) JJA; and d) SON, respectively.

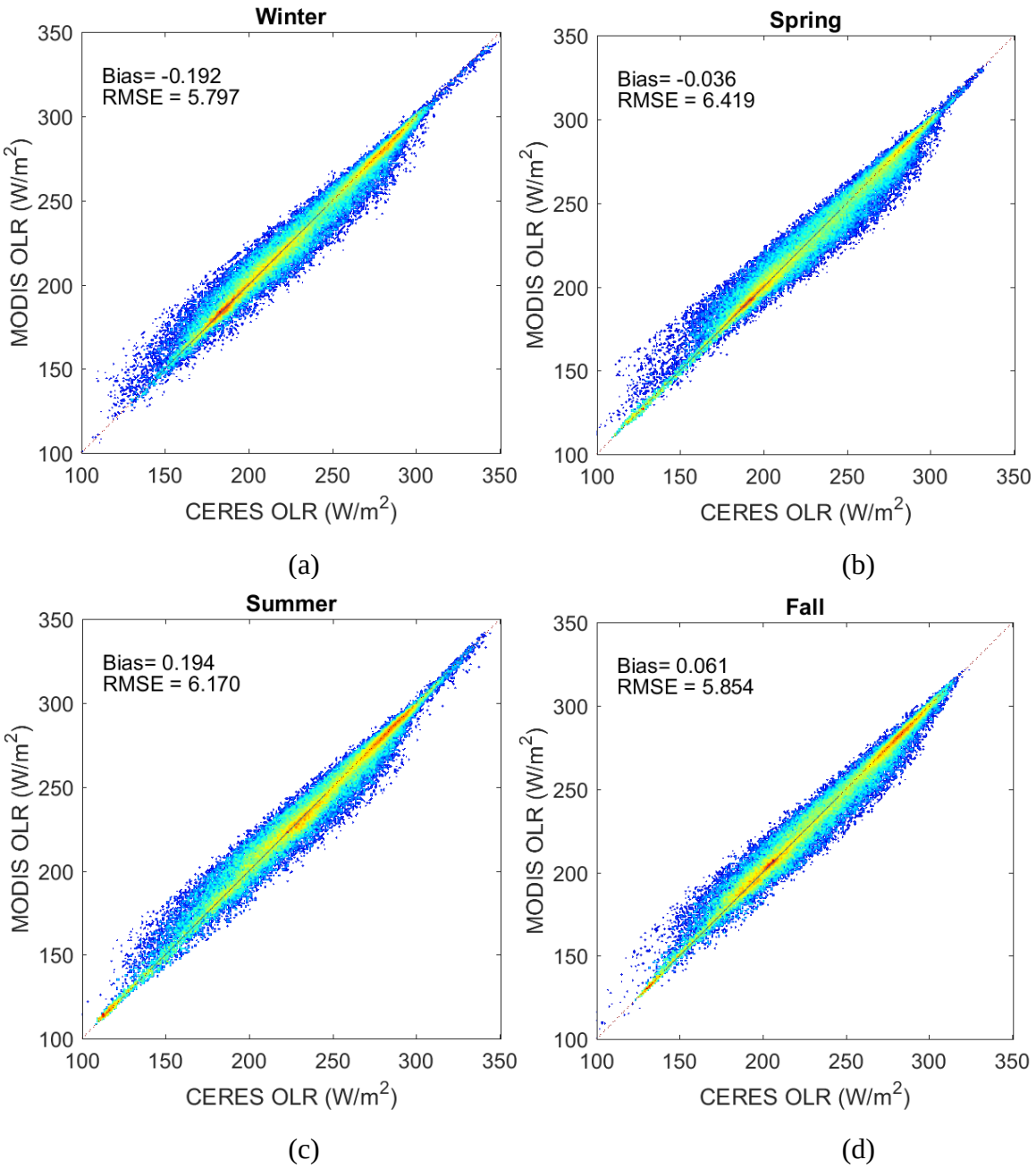

Figure 3-11 Comparisons between MODIS retrieved OLR and CERES OLR SSF product with 20-km resolution under all-sky condition for a) DJF; b) MAM; c) JJA; and d) SON, respectively.

Futhermore, CERES SSF1Deg dataset takes the instantaneous footprint level fluxes and cloud properties as input and output the instantaneous gridded fluxes. For the MODIS OLR retrieval, it was firstly aggreated to 1° grid scale, and then compared with the CERES 1° data. Here, the whole year 2013 OLR were calculated from both datasets for four surface

types mentioned above. Figure 3-12 reports the temporal comparison of the OLR from MODIS and CERES at 1° × 1° resolution by presenting their annual variations. It is obvious that both curves agree with each other quite well in general and both of them clearly depict the OLR seasonal variation. In details, the MODIS OLR shows slightly larger fluctuation than CERES attributed to its relatively higher spatial resolution before aggregation.

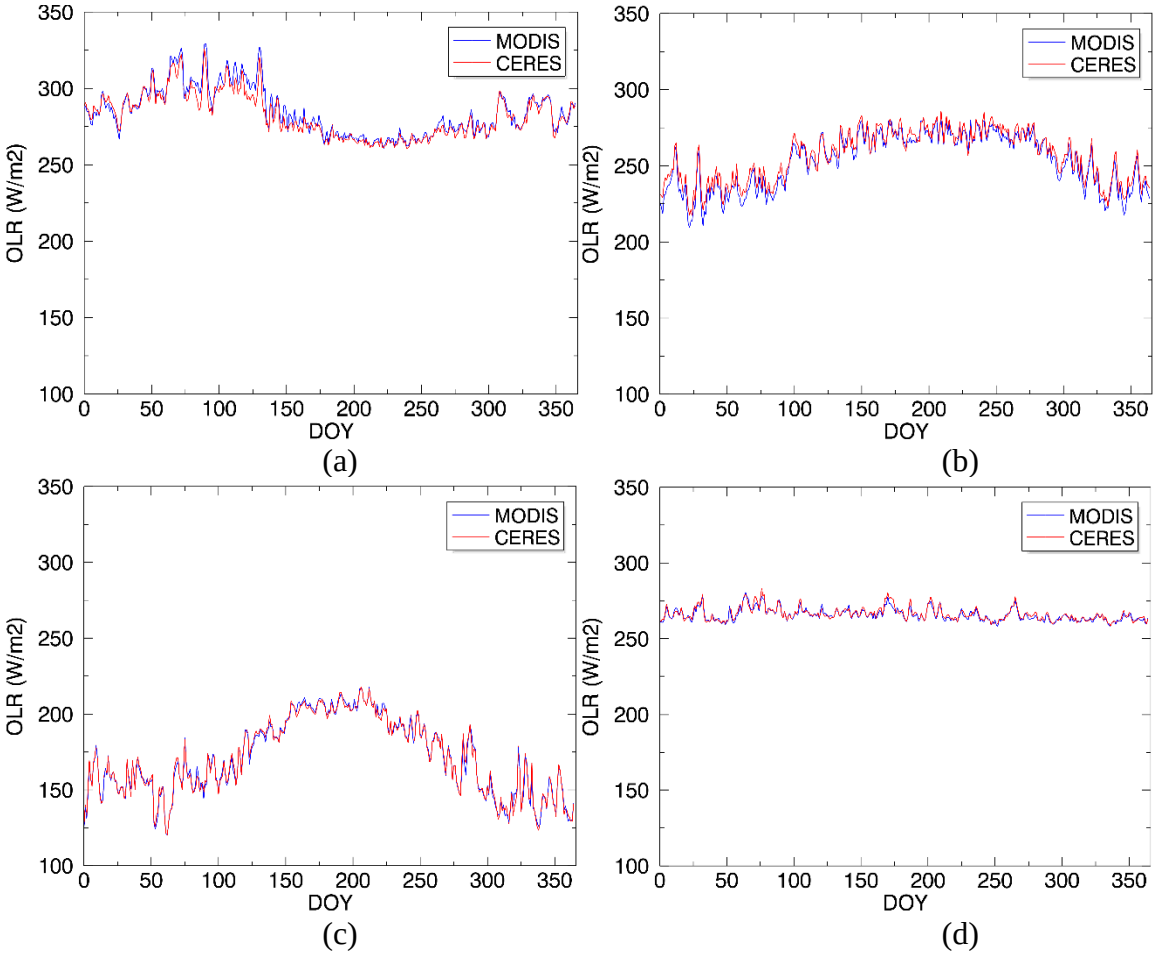

Figure 3-12 Comparisons of OLR variations in 2013 between MODIS and CERES over a) desert, b) vegetated surface, c) ice/snow, and d) water/ocean surfaces, respectively.

At the map level, Figure 3-13 illustrate the global all-sky OLR map comparison at 1° × 1° for the on the day of Jul 17th, 2013. Apparently, the OLR from both datasets have very similar spatial patterns, and they both displays highly latitude-dependent spatial pattern mainly due to the land surface and atmosphere temperatures. At high latitude

regions (> 60° and < -60°), Greenland and Antarctic show significantly lower OLR values (less than 220 W/m^2) than others on the earth. In addition, different land surface types present obvious different OLR levels even if they located at similar latitude zones, which is especially observed between the vegetated surfaces (Amazon Forest and the Middle Africa) and desert/barren-soil dominated surfaces (Sahara desert and Arab peninsula), matching the indication of quantitative comparison shown in Figure 3-9a and Figure 3-9b. Moreover, the elevation is also one of the controlling factors of OLR, which is demonstrated by the apparent OLR boundaries between Tibet Plateau and South Asia area or inland China observed in both MODIS and CERES maps. Quantitatively, the two maps have a bias of -0.57 W/m^2 (MODIS-CERES) and a *RMSE* of 6.7 W/m^2 (Figure 3-13c).

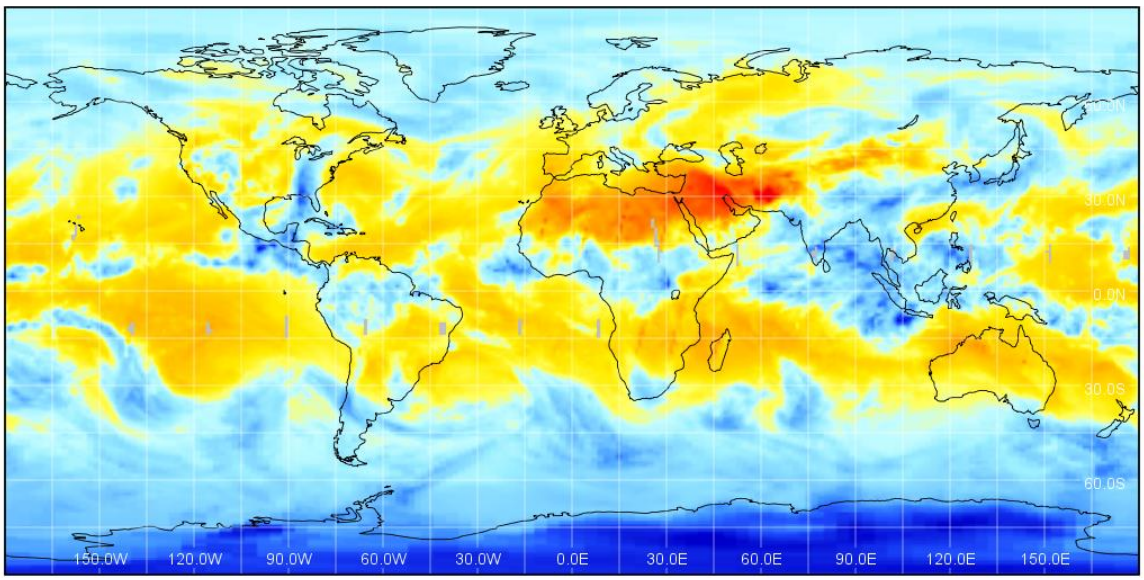

(a)

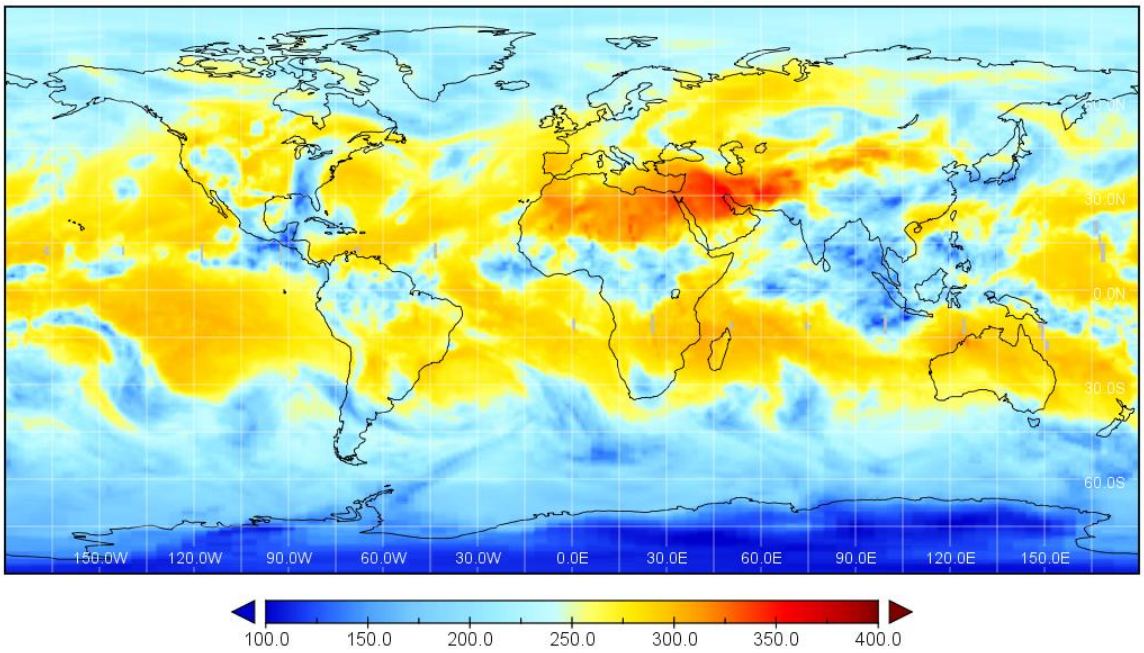

(b)

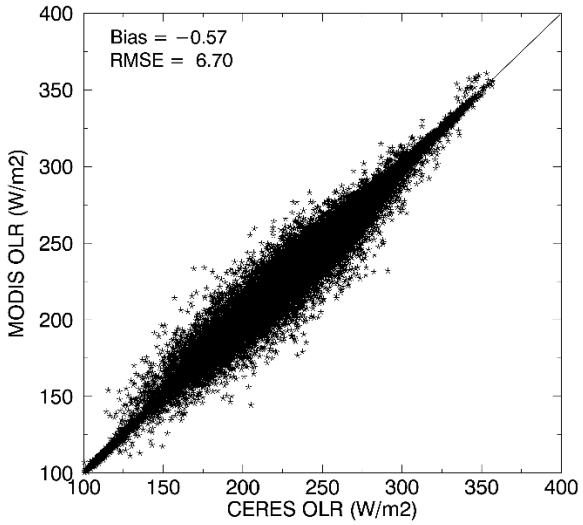

(c)

Figure 3-13 Global all-sky OLR map comparison between a) MODIS estimation and b) CERES products on Jul 17th, 2013. c) Scatter plot based on a) and b). Spatial resolution is 1° × 1°.

At a further larger scale, Figure 3-14 provides the zonal distributions of OLR estimated from MODIS and CERES based on the maps shown in Figure 3-13. Since the underlying data were extracted from JJA season of the North Hemisphere (NH), the South Hemisphere (SH) shows significantly smaller OLR than that of NH, especially for the

Antarctic area which is under the polar night period. From the OLR difference plot (Figure 3-13c), the biases are further reduced within ±2 W/m^2 in the zonal average process. The largest underestimation falls between 30°N to 70°N, which is reasonable considering that this region is dominated by medium-latitude continents that are naturally more complex in regarding to land surface components and atmospheric conditions.

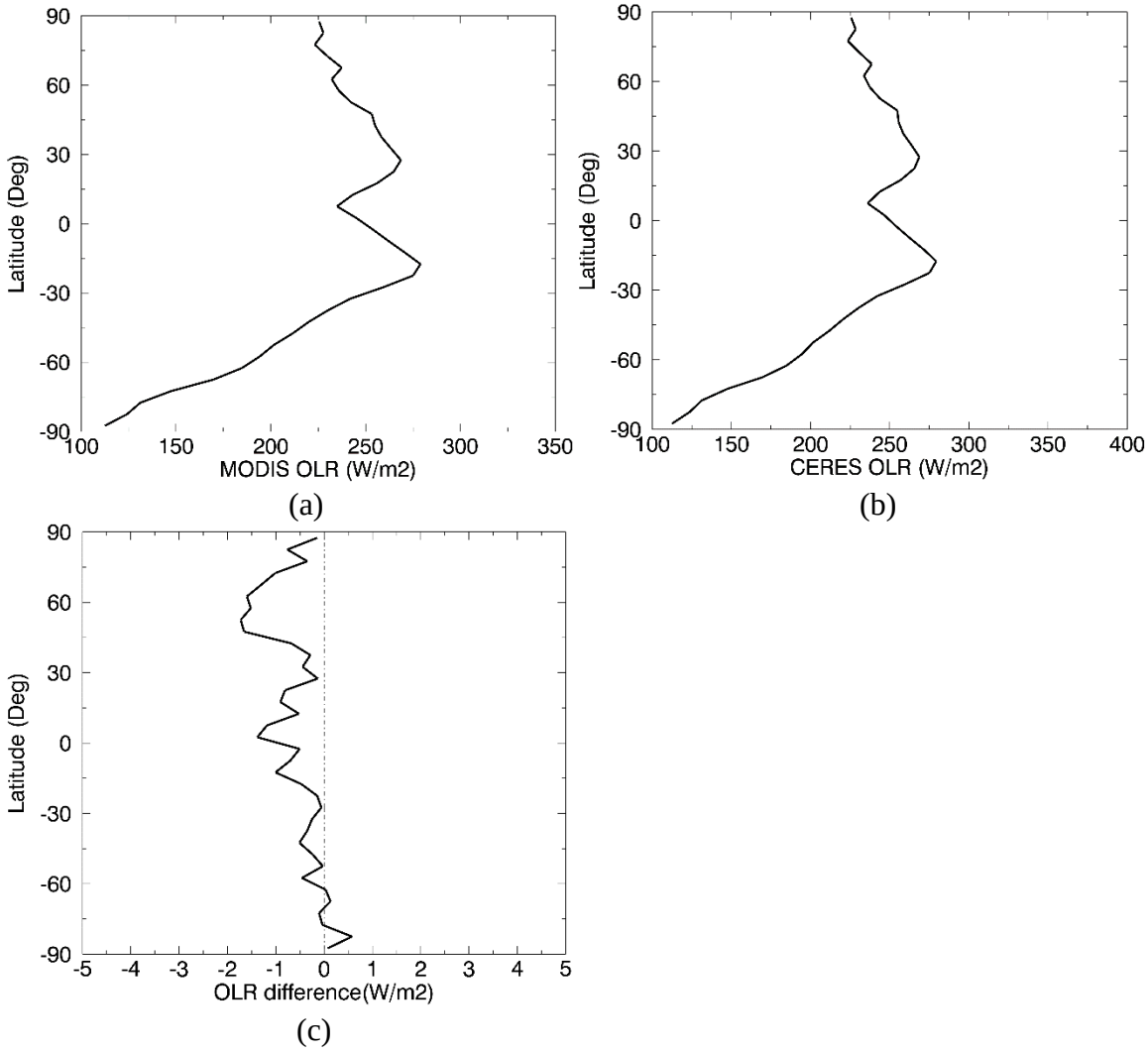

Figure 3-14 Zonal mean values of the maps shown in Figure 3-13 for a) MODIS OLR and b) CERES OLR, and c) OLR difference, respectively.

3.3.3.2 AVHRR OLR

In this section, both CERES and HIRS OLR products were collected as the reference to conduct comparisons with AVHRR OLR retrievals. CERES has been widely recognized as the most accurate TOA broadband flux measurements; while HIRS provides long-term record of OLR from 1979 to present which covers the entire range of AVHRR data. Comparisons were performed at three different spatial and temporal scales: 1) AVHRR instantaneous OLR estimates were compared with CERES SSF L2 instantaneous OLR product at spatial resolution of 20-km; 2) AVHRR daily-mean OLR calculations were compared with CERES SYN1deg OLR product at spatial resolution of 1°; 3) AVHRR monthly composited OLR were compared with CERES EBAF, HIRS, and NOAA interpolated AVHRR monthly OLR products at 2.5°.

3.3.3.2.1 Instantaneous OLR comparison at 20-km resolution

The instantaneous AVHRR observation of the TOA radiance (AVH02C1) was used to retrieve the instantaneous OLR with 0.05° resolution. The viewing geometry and cloud mask included in the data package was employed to distinguish clear and cloudy pixels and separate models were employed accordingly. The CERES SSF L2 OLR product at the instantaneous footprint level with 20 km spatial resolution was used as reference for the comparison. Figure 3-15 shows the validation results for four days in 2014 (January 1, April 1, July 1, October 1) as representatives for different seasons. In general, the instantaneous AVHRR OLR agrees with the CERES product for all four days (*RMSE* of 7 W/m^2 and bias of ±4 W/m^2). For the longwave flux at the TOA level, however, such biases are always considered to be a relatively large mismatch between two satellite retrievals,

especially for OLR. This is likely due to the different passing time of the NOAA satellite series and CERES *Terra* or *Aqua* platforms; the OLR always has drastic diurnal variations. Therefore, a daily mean OLR estimate is necessary; this is even more important for applications than for instantaneous retrievals.

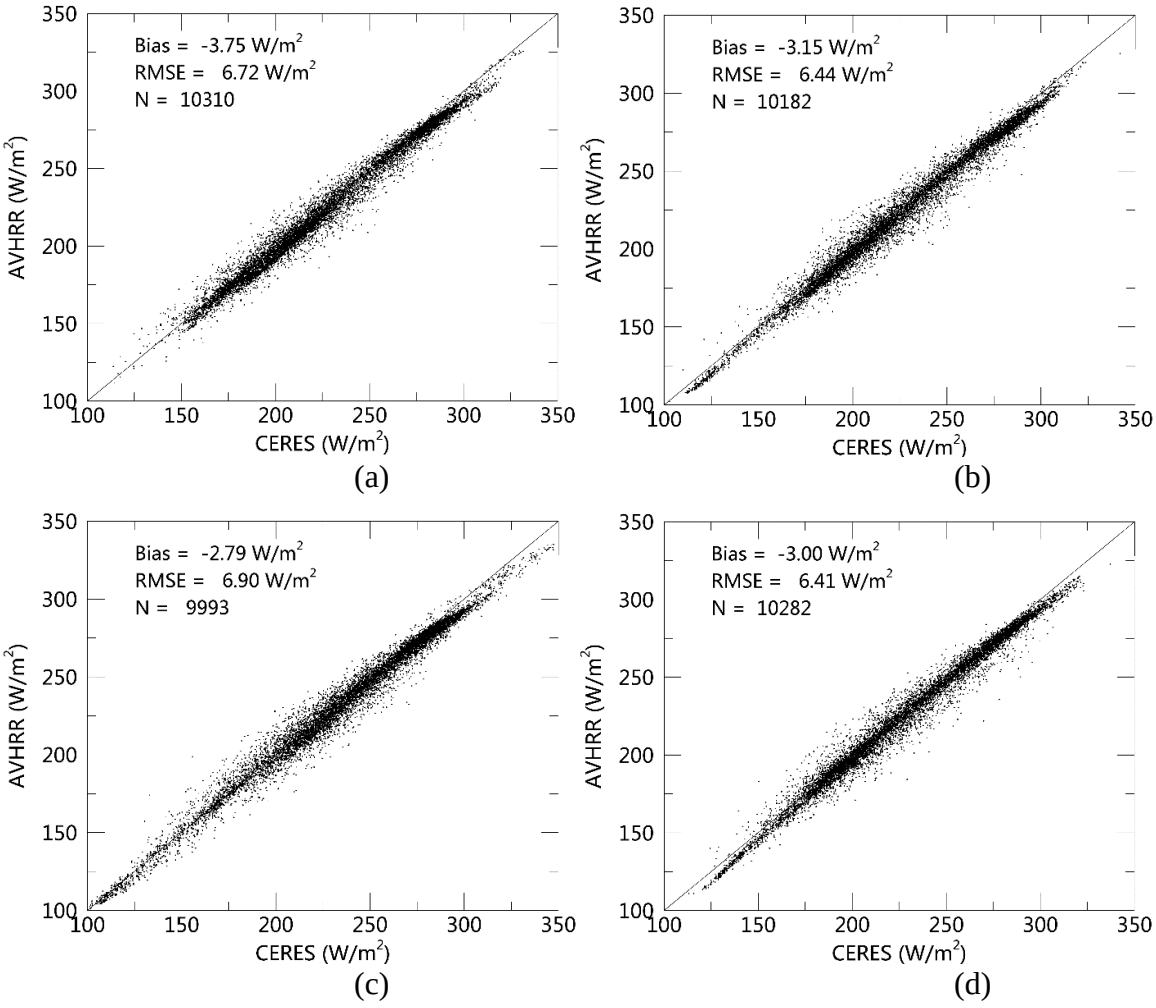

Figure 3-15 Comparison between the instantaneous AVHRR OLR retrieval and CERES OLR SSF product in the 2014 for a) DJF, b) MAM, c) JJA, and d) SON, respectively.

3.3.3.2.2 Daily mean OLR comparison at 1° resolution

The daily mean AVHRR OLR was estimated from the instantaneous retrieval based on the linear models developed in section 3.2.2. The collocated CERES daily mean OLR product (SYN1deg-Day) was used as the reference for the comparison. Due to the different

spatial resolution of the two datasets, the AVHRR estimations were firstly aggregated in a 20 × 20 pixel window to match the CERES grid size. Figure 3-16 shows the daily mean OLR comparisons for four representative land surface types: vegetation, desert, ocean, and permanent snow. For each surface, 200 sample grids were randomly extracted from the CERES images for each day from 2001 to 2015 for which both AVHRR and CERES data are available. The MODIS land cover type (MCD12C1) data was used to provide the IGBP land cover class for this purpose. In general, the daily mean AVHRR OLR agrees well with the CERES daily mean product for all surfaces (*RMSE* < 3.1 W/m^2; bias = ±1.1 W/m^2). In detail, very slight underestimation biases (> -0.4 W/m^2) are observed for vegetation and ocean surfaces, while the desert displays a relatively larger overestimation of 0.8 W/m^2 and snow cover shows an underestimation of up to -1.03 W/m^2. Compared with the instantaneous OLR, the daily mean OLR matches CERES better, as was expected based on the exclusion of diurnal OLR variation and the influence of different sensor scanning times of instantaneous retrievals.

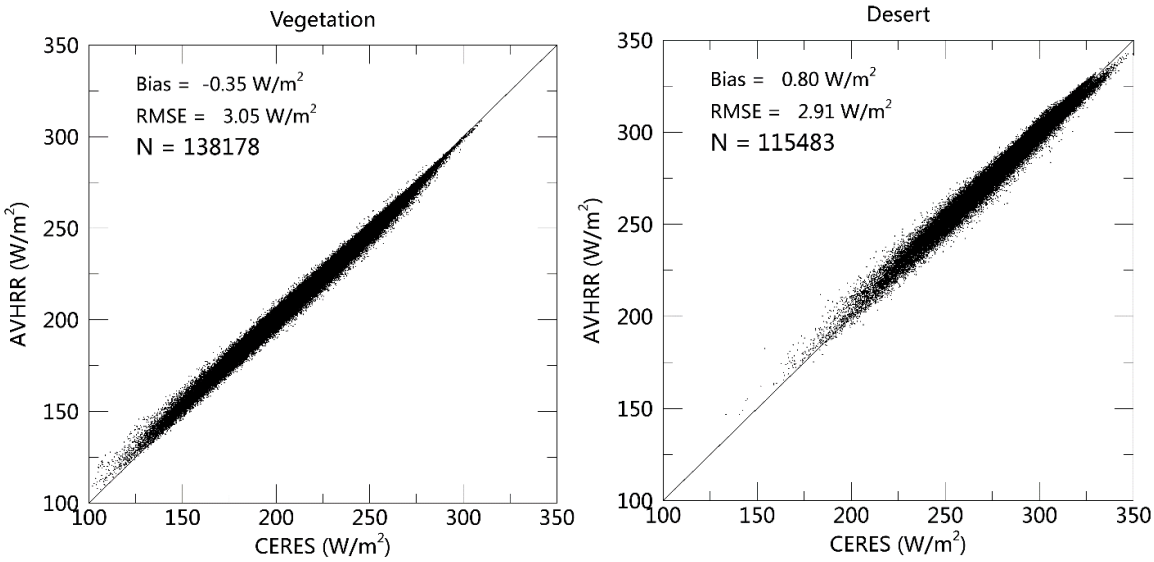

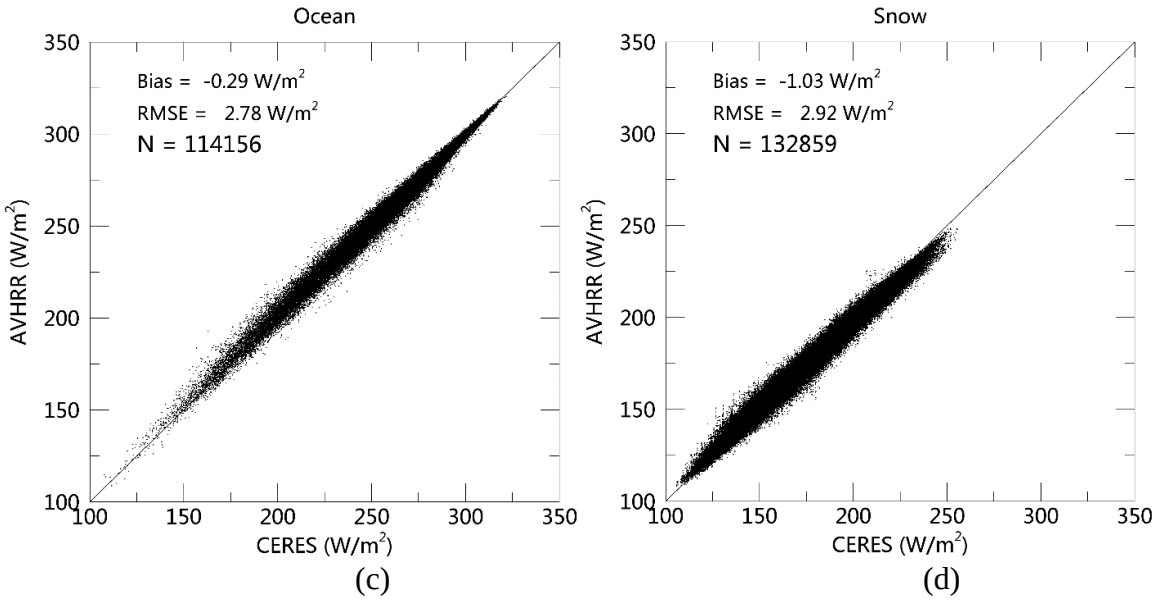

Figure 3-16 Comparison of the daily mean OLR retrieved from AVHRR data with the collocated CERES daily mean OLR product for a) vegetation, b) desert, c) water/ocean, and d) permanent snow surfaces, respectively

Furthermore, to investigate the spatial pattern of the daily mean OLR, the annual mean OLR global maps based on daily mean data for 2015 were compared. OLR global maps from AVHRR and the CERES SYN1deg-Day product and difference map between them are shown in Figure 3-17; the calculation of the latitude-based zonal mean with interval of 5° corresponding to Figure 3-17 is displayed in Figure 3-18. The daily mean AVHRR OLR agrees very well with that of CERES; they both display highly latitude-dependent spatial patterns that are mainly due to the land surface and atmosphere temperature. In high latitude areas (> 60° and < -60°), Greenland and the Antarctic show significantly lower OLR values (< 200 W/m^2) than other areas on Earth, while the oceans within these areas have much larger OLR than land. This is likely due to the facts that 1) oceans have much higher heat contents than land and 2) ocean currents have much more convection with temperate and tropical zones than the Greenland and Antarctic continents. Such discrepancies between oceans and land also exist at medium or low latitude; in

regions of the Pacific, Atlantic, and Indian oceans, the OLR is notably higher than that on land. In addition, different land surface types show significantly different OLR levels, even if they located at similar latitudes. This difference is especially evident between the vegetated surfaces (North America, Amazon Forest, Middle Africa) and desert/barren-soil dominated surfaces (Sahara desert, Arab peninsula, Australia), matching the quantitative comparison shown in Figure 3-16a and Figure 3-16b. Moreover, the elevation is also one of the controlling factors of OLR, which is demonstrated by apparent OLR boundaries between the Tibet Plateau and South Asia or China on both AVHRR and CERES maps. Based on the daily mean OLR difference maps (Figure 3-17c), the AVHRR overestimates OLR compared with CERES, mainly for desert or barren land surfaces such as the Sahara and Australia. The statistics in Figure 3-16b also support this fact. With respect to underestimation, the tropical oceans and Amazon Forest in Figure 3-17c also verify the statistics reported in Figure 3-16a and Figure 3-16c. However, contradictions were observed in Figure 3-16d and Figure 3-17c for the Greenland area, where the former shows an underestimation of up to 1.03 W/m^2, while the latter displays almost no difference. Nevertheless, the negative biases in Figure 3-16d are associated with higher OLR ranges (> 220 W/m^2), which should not be attributed to 2015 based on the OLR values (< 200 W/m^2) in Greenland (Figure 3-17a and b). Considering that the data in Figure 3-16 include fifteen years from 2001 to 2015, the overestimation of permanent snow surfaces is probably due to several warm winter years in the Northern Hemisphere (NH).

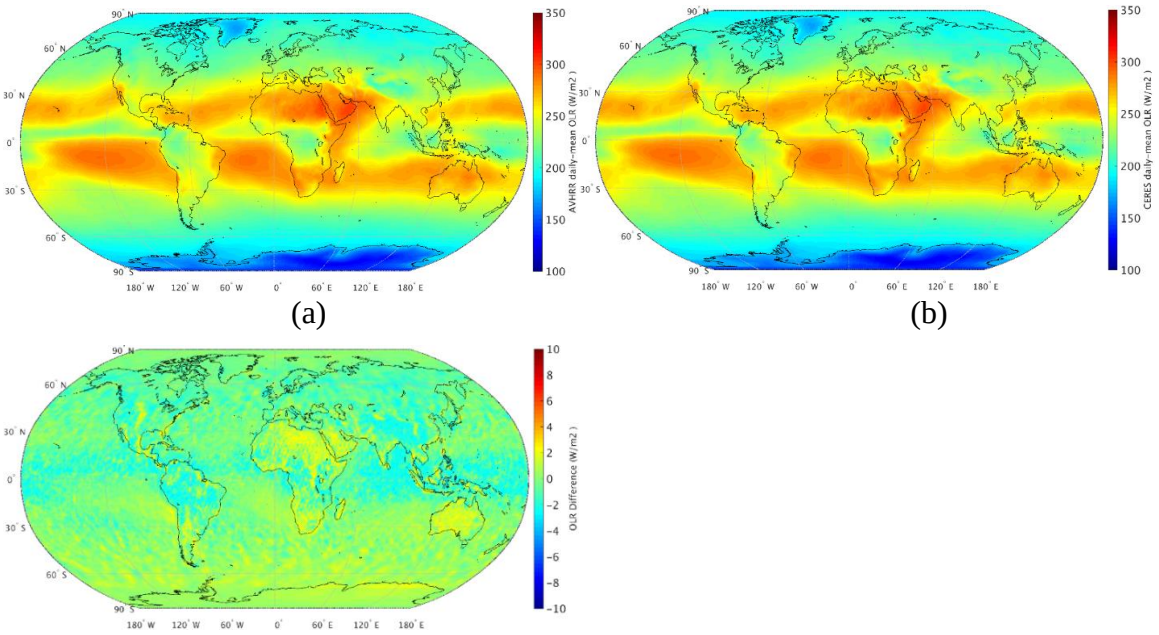

Figure 3-17 Annual mean OLR global map based on daily OLR data for 2015 from the a) AVHRR retrieval, b) CERES SYN1deg-Day product, and c) difference between those two datasets. The spatial resolution is 1°

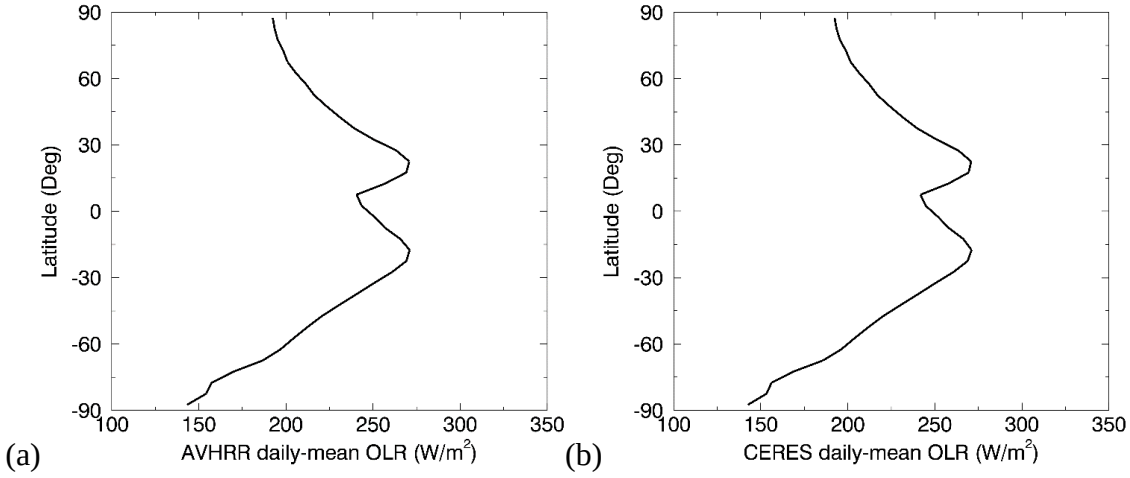

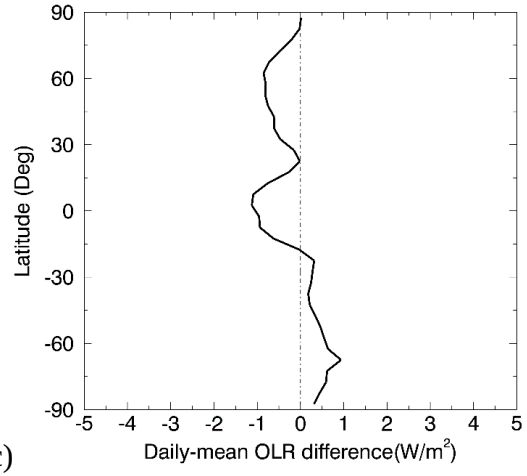

(c)

Figure 3-18 Annual zonal mean values of the maps shown in Figure 3-17 Error! Reference source not found. **for a) AVHRR, b) CERES, and c) difference between them, respectively.**

3.3.3.2.3 Monthly OLR comparison at 2.5° resolution

Monthly OLR comparisons were made among AVHRR monthly composited OLR based on daily-mean calculation, CERES EBAF monthly OLR product, HIRS monthly OLR product, and NOAA interpolated monthly OLR product. AVHRR and CERES EBAF OLRs were aggregated to 2.5° to match the resolutions of the latter two OLR products.

Multi-year mean (also known as climatology) OLR values reflect the mean states of the Earth's emitted radiation to space at a long-term scale, which plays as the foundation of investigation of the OLR anomaly that usually indicates extreme climate events such as El Niño. Figure 3-19 and Figure 3-20 display OLR climatology comparisons for DJF and JJA seasons, respectively. The base period for climatology comparison is from 2000 to 2016, the overlapped period among all the four OLR datasets. For both seasons, AVHRR achieves high agreements other three reference OLR datasets in general, and they have globally similar spatial patterns. In detail, AVHRR shows smaller values than those of both CERES and HIRS, while larger values compared to NOAA interpolated; according to Table 3-5, AVHRR slightly underestimates CERES and HIRS within 3 W/m^2 in both

seasons. It is obvious, although biases are close, that AVHRR is more consistent with CERES than with HIRS, by showing smaller *RMSE* with the former than the latter. This is attributed to the larger spatial variation of the OLR difference between AVHRR and HIRS, that is, larger positive bias is seen in high latitude areas dominated by ice and snow especially in Antarctica, while larger negative bias are present in low latitude regions especially over ocean surfaces. For NOAA interpolated, current AVHRR overestimates up to 2.13 W/m^2 and 2.07 W/m^2 for DJF and JJA, respectively; and with lower spatial variation of the difference, resulting in relatively lower RMSEs compared to those of CERES and HIRS. In addition, the opposite biases also indicate that NOAA interpolated OLR products have relatively large inconsistences with CERES and HIRS.

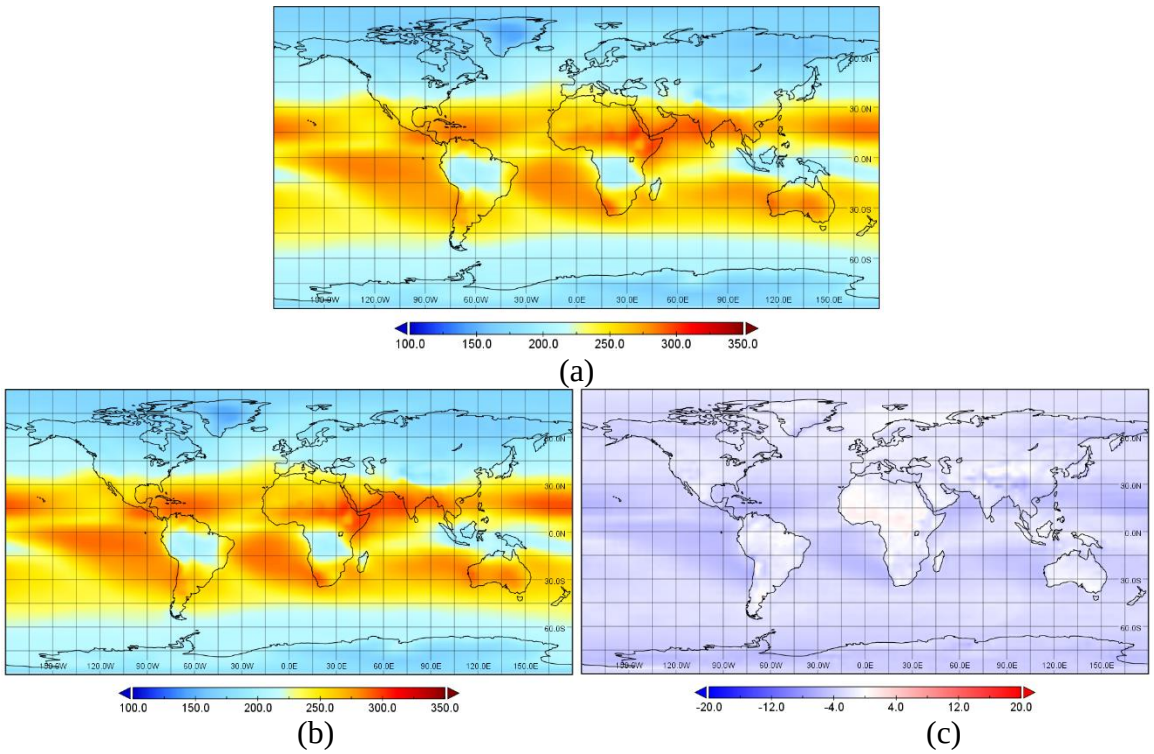

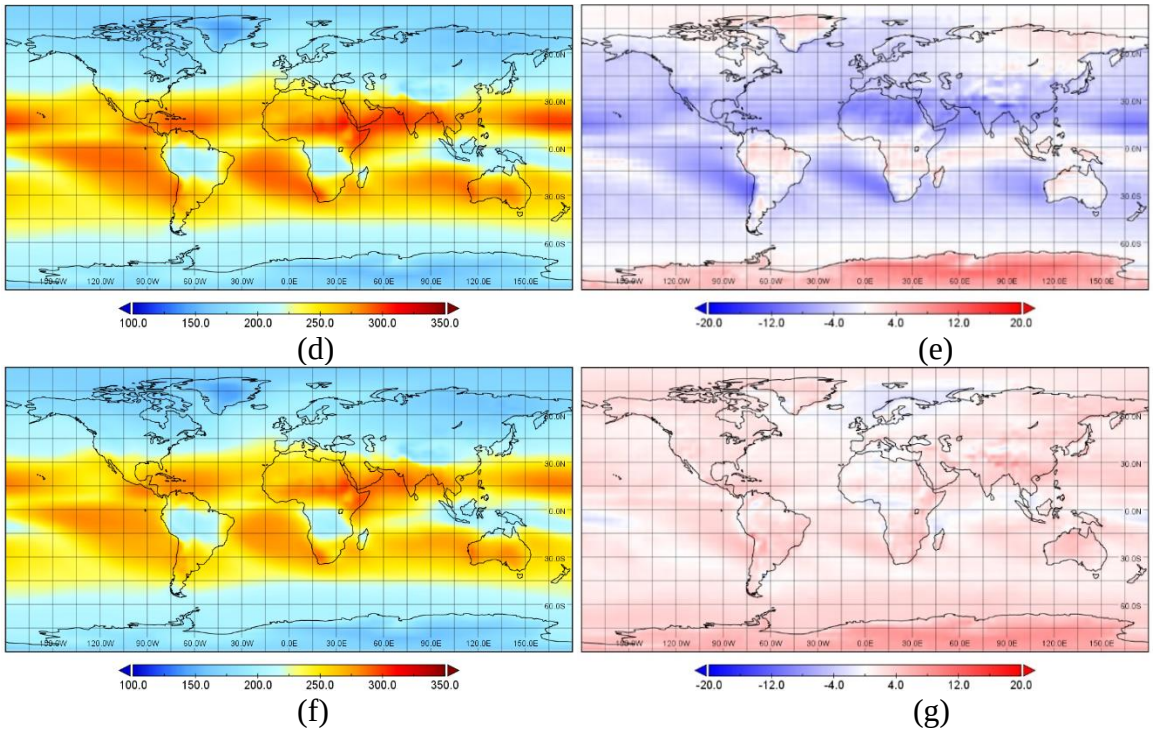

Figure 3-19 OLR climatology for DJF over 2000-2016 calculated from a) AVHRR, b) CERES, d) HIRS, f) NOAA interpolated, and the difference between c) AVHRR and CERES, d) AVHRR and HIRS, and g) AVHRR and NOAA interpolated.

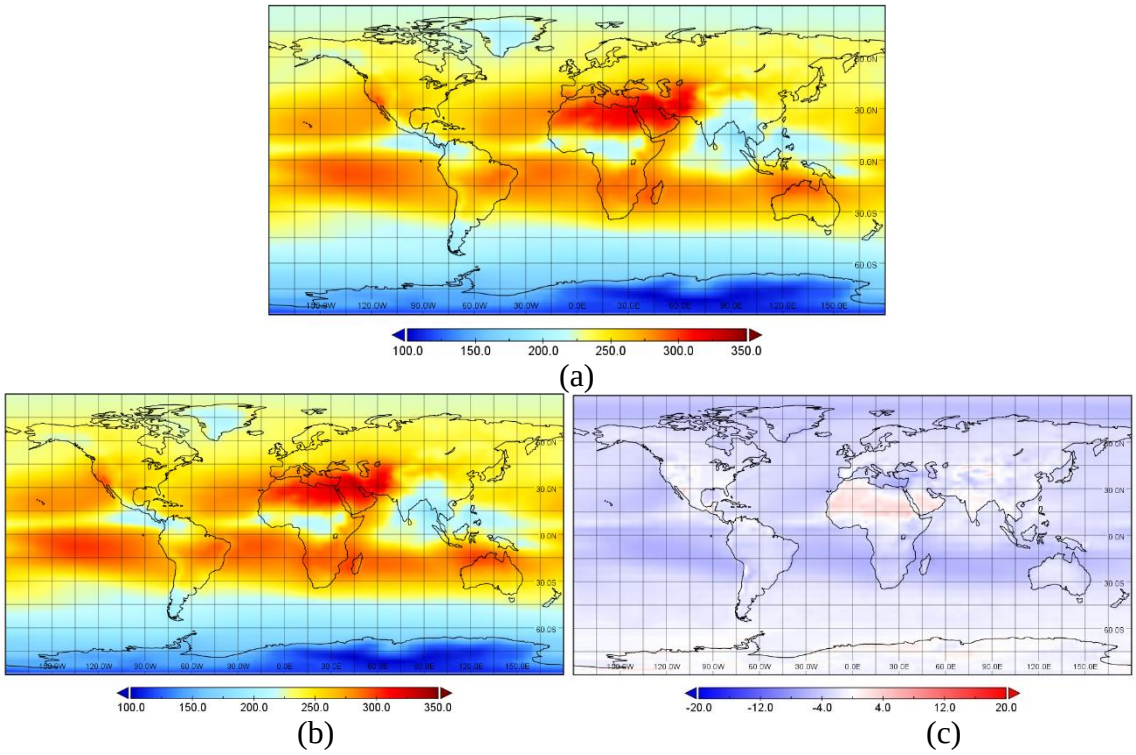

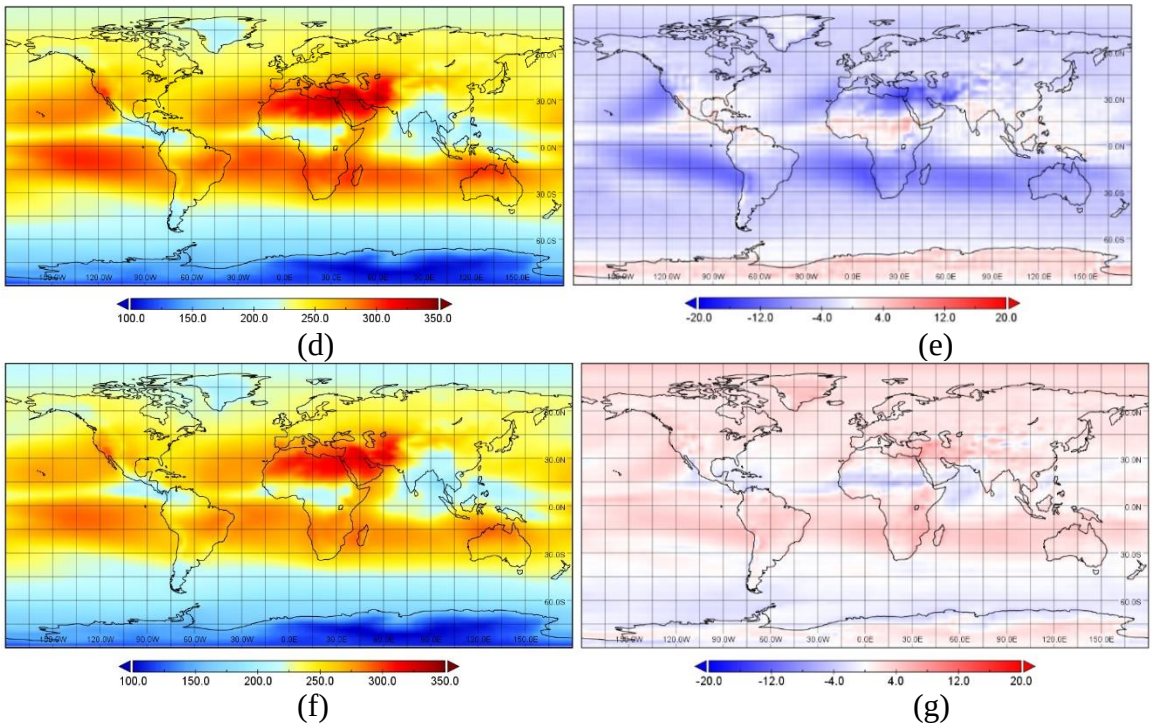

Figure 3-20 OLR climatology for JJA over 2000-2016 calculated from a) AVHRR, b) CERES, d) HIRS, f) NOAA interpolated, and the difference between c) AVHRR and CERES, d) AVHRR and HIRS, and g) AVHRR and NOAA interpolated.

Table 3-5 Statistics of the global mean OLR climatology comparisons among AVHRR, CERES, and HIRS corresponding to Figure 3-19 and Figure 3-20.

	DJF		JJA	
	Bias (W/m^2)	**RMSE (W/m^2)**	**Bias (W/m^2)**	**RMSE (W/m^2)**
CERES	-2.78	3.03	-2.35	2.90
HIRS	-1.50	3.90	-2.88	3.95
NOAA interpolated	2.13	2.79	2.07	2.05

Long-term timeseries comparisons were also performed to investigate the monthly variations of OLR. Figure 3-21 plots the four OLRs at monthly scale from 1981 to 2016 (CERES starts from 2000). The sinusoidal-like cycles of those curves reflect the seasonal variation of OLR mainly due to the difference in earth surface temperature among seasons. It is seen that the developed AVHRR OLR is generally consistent with HIRS in the entire period (Figure 3-21a), showing slightly smaller values than HIRS of about 2 W/m^2 , and

such bias displays almost no seasonal variation (Figure 3-21b). It also agrees well with CERES after 2000 at a similar magnitude of negative biases. However, obvious seasonal variations can be observed of such biases and the phase of the bias curves is just π away from that of the AVHRR OLR original curves (Figure 3-21b), suggesting that in NH winter season when snow dominates northern high latitude regions, relatively larger uncertainties exist between the AVHRR and CERES EBAF OLR estimates. Last, the NOAA interpolated OLR product shows apparent smaller values (about 2.5 W/m^2) than AVHRR, as well as HIRS and CERES EBAF, emphasizing again that a more stable and consistent OLR product from AVHRR data is needed.

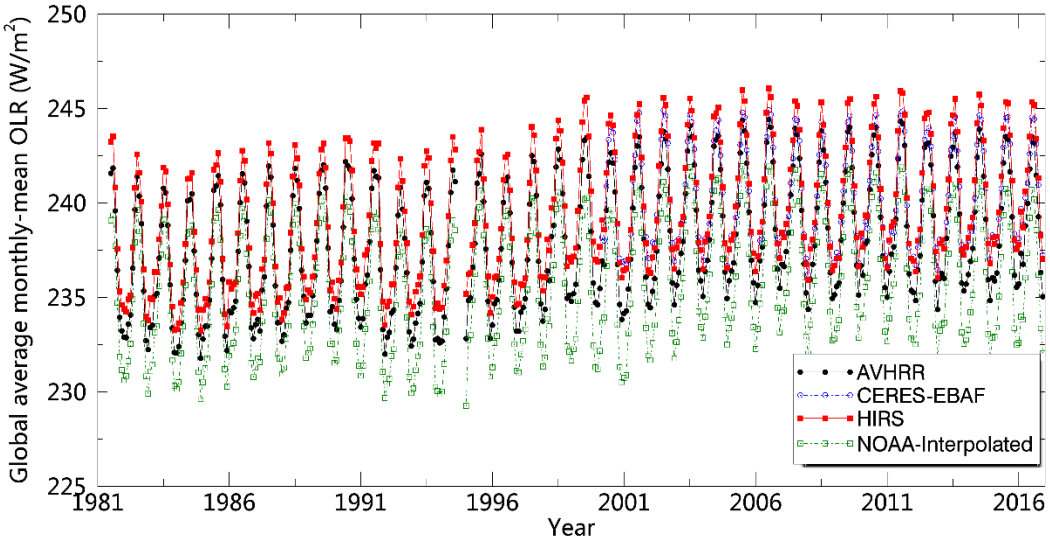

(a)

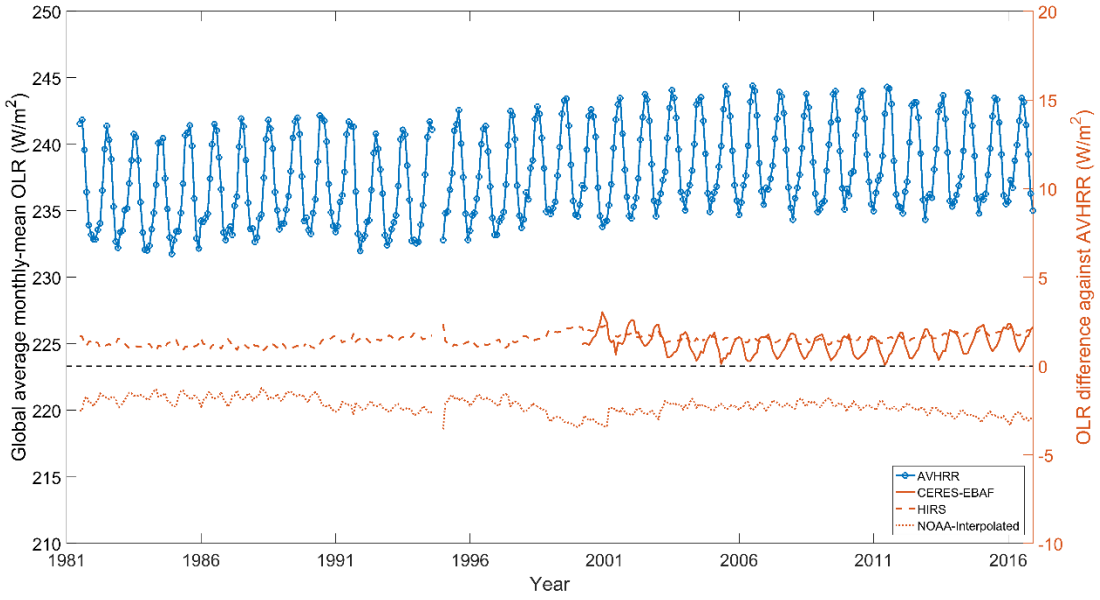

(b)

Figure 3-21 Long-term timeseries of global mean monthly OLR from 1981 to 2016

3.3.4 AVHRR OLR Response to ENSO

As stated in Chapter 1, OLR is a critical parameter associating with multiple climate issues. ENSO, a dominant climate phenomenon inducing extreme weather conditions worldwide (Mayer et al., 2016), has been widely investigated based on the anomalies in SST. Since OLR contains the integrated information of surface and atmosphere thermal conditions, anomalies in SST and in cloud properties are often reflected in anomalies in OLR. During ENSO, the tropical SST changes drastically and OLR responds strongly (Wong et al., 2006). Thanks to the long-term record of AVHRR data, this section investigated if, and to what extent, the developed AVHRR OLR can response to ENSO. According to widespread studies on ENSO, two regions within the central Pacific Ocean are considered the best areas to indicate the occurrence of ENSO: they are Niño 3 (5°N–5°S, 90°–150°W) for El Niño (Bamston et al., 1997; Trenberth, 1997b), and Niño 3.4 (5°N–5°S, 120°–170°W) for La Niña (Bamston et al., 1997), respectively. Currently, an El Niño

is characterized typically by five consecutive three-month running mean SST anomalies, known as the Oceanic Niño Index (ONI), in the Niño 3.4 region above a threshold of +0.5°C. For La Niña, the ONI_{SST} threshold is below -0.5°C in the Niño 4 region. Following this method, the three-month running mean of AVHRR OLR anomalies (hereinafter, ONI_{OLR}) were calculated from 1981 to 2016 and then picked up two widely recognized ENSO events occurred in December 2015 (El Niño) and December 2010 (La Niña) for illustration. Figure 3-22 exhibit the ONI_{OLR} for the central Pacific region in those two months. It is apparent that the ONI_{OLR} displays extremely negative values (< -25 W/m^2) in the Niño 3.4 region during El Niño (Figure 3-22a). The underlying mechanism is that the Pacific Walker circulation is significantly modulated, leading to enhanced atmospheric convection and hence more cloud cover in the central and eastern equatorial Pacific lowering the OLR. In addition, more convective activity in this region induces higher and colder cloud tops, further resulting in a decrease in OLR. During La Niña, the opposite occurs and OLR increases, showing highly positive anomaly in the Niño 4 region (Figure 3-22b).

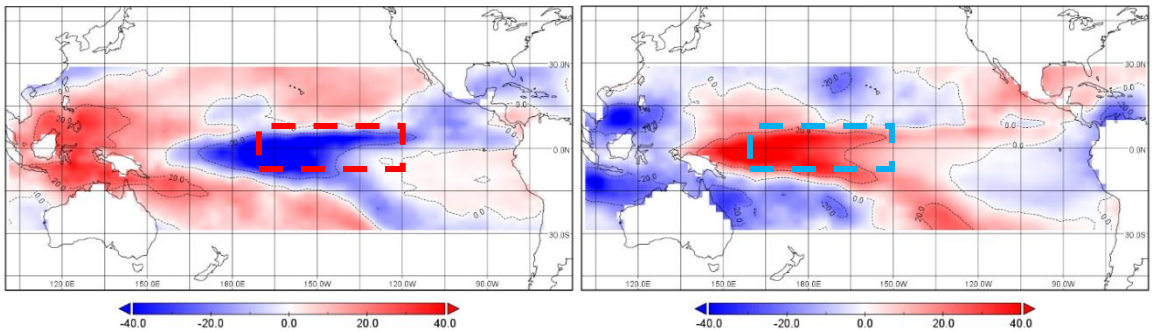

Figure 3-22 Three-month running mean of AVHRR OLR anomalies in the peak of a) a El Niño period (December 2015) and b) a La Niña period (December 2010) within the central Pacific region (30°N–30°S, 100°E–60°W). The red and blue boxes mark the Niño 3.4 and Nino 4 regions, respectively. Unit: W/m^2.

Apart from these two examples, this study further explored the capability of the developed AVHRR OLR in capturing ENSO cycles in long-time series. Thus, correlation analysis between ONI_{SST} and ONI_{OLR} was also conducted. Figure 3-23 and Figure 3-24 plot ONI_{SST} and ONI_{OLR} in both Niño 3.4 and Niño 4 regions, respectively, from 1981 to 2016. With the threshold of +0.5°C (-0.5°C) employed on ONI_{SST}, the El Niño (La Niña) cycles can be clearly identified (Figure 3-23). Meanwhile, it is evident that the temporal variations of ONI_{SST} and ONI_{OLR} are strongly and negatively correlated (correlation coefficient (R) = -0.81 in both Niño 3.4 and Niño 4), manifesting similar principles to that in Figure 3-22, and in conclusion, ONI_{OLR} has a great capability of capturing both El Niño and La Niña evens occurred in the past 35 years.

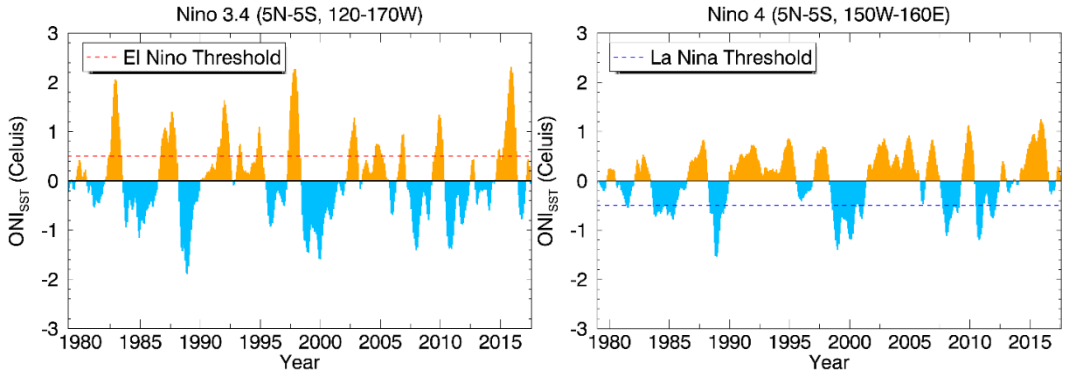

(a) (b)

Figure 3-23 Long-time series (1979–2016) of the spatially averaged ONI_{SST} for the a) Niño 3.4 and b) Niño 4 regions calculated from SST.

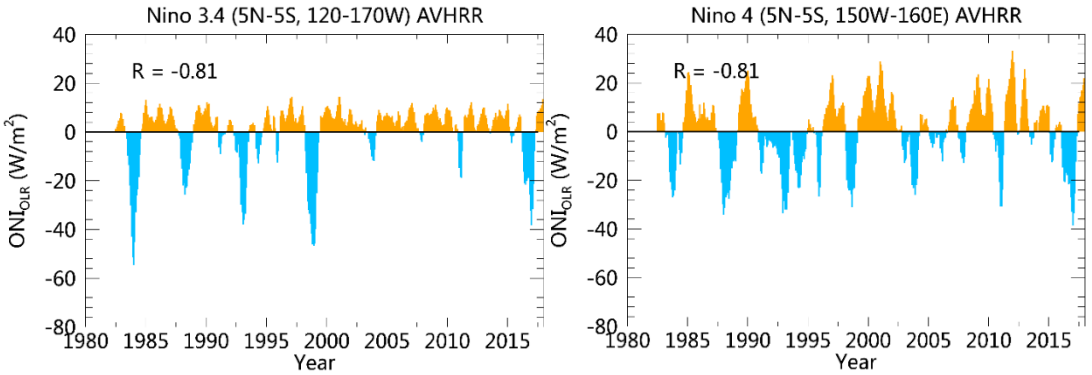

(a) (b)

Figure 3-24 Long-time series (1979–2016) of the spatially averaged ONI_{OLR} for the a) Niño 3.4 and b) Niño 4 regions calculated from AVHRR OLR.

3.4 Conclusions and Discussions

This chapter presents a hybrid algorithm framework to estimate the instantaneous OLR from multi-spectral satellite data. OLR was directly linked to the TOA spectral radiances using statistical regression models based on extensive radiative transfer simulations using MODTRAN 5 with extensive atmosphere and cloud profiles for different viewing geometries. In addition, a conversion method was developed for calculating the daily mean OLR from instantaneous retrievals and CERES hourly and daily OLR products. Based on the framework, MODIS and AVHRR data were employed to generate OLR data, and comprehensive evaluations were conducted at difference spatial and temporal scales.

For MODIS instantaneous OLR, validation based on the simulated datasets indicated that the linear model account for about 98% of the variation for clear sky condition and 96% for cloudy sky condition, and with *RMSE* less than 0.12 W/m^2 for both conditions. Comparisons with CERES data showed that the MODIS retrieval agree well with CERES SSF OLR products in general, with *RMSE*s less than 3.5 W/m^2 (6 W/m^2) and absolute biases less than ±0.15 W/m^2 (0.2 W/m^2) for clear sky (all sky) condition. Surface based comparisons indicate that biases direct to different directions for different land types (underestimation for vegetated and snow surfaces; overestimation for desert and ocean surfaces). Comparisons performed at larger scale, including 1°×1° resolution and zonal mean scale, also suggests the similar temporal and spatial OLR patterns between MODIS and CERES.

For AVHRR long-term OLR record generated from 1981 to 2016, the validation based on the simulated datasets indicates that the linear models account for ~97% of the variation for clear-sky conditions and 95% for cloudy-sky conditions. The *RMSE* of the

fitted models is < 0.13 W/m^2 for both sky conditions. Using the simulated data associating with the spectral response function of HIRS data, high agreements were achieved between local HIRS OLR calculation and the public HIRS OLR product. The comparisons with CERES data show that the instantaneous AVHRR retrievals generally agree with the CERES SSF L2 instantaneous OLR product (*RMSE* < 7 W/m^2; absolute difference (*AD)* < 4 W/m^2). For the daily mean OLR comparisons, AVHRR daily OLR also achieves high agreements with CERES SYN1deg-Day OLR product over different type of earth surfaces (*RMSE* < 3.1 W/m^2; absolute biases within 1.1 W/m^2). Moreover, climatology and long-term timeseries inter-comparisons among AVHRR monthly composited OLR and other three monthly OLR products (including CERES EBAF, HIRS, and NOAA interpolated) demonstrated that AVHRR OLR is consistent with CERES and HIRS products, and NOAA interpolated ORL products presented larger differences with the former three. Last but not least, the developed AVHRR OLR was proved to be capable of capturing the ENSO cycles during the past 35 years.

The theoretical basis of the proposed algorithm is a heritage of the direct estimation method that has been applied extensively to estimate a variety of variables including land surface albedo, land surface upward and downward longwave radiation, TOA albedo, etc. (Liang, 2003; Wang and Liang, 2016; Wang et al., 2013; Wang and Liang, 2009; Wang et al., 2009). To estimate OLR from multi-spectral satellite, this method is treated as the best option since it simplifies the whole task as a two-step procedures: radiative transfer simulation and regression analysis. This method uses the TOA spectral radiance as the major input. It does not rely on the scene type parameters which are essential in ADM model, and only the cloud detection needed to select the correct LUT. In addition, there is

no need to construct a set anisotropic factors for different scene types which need auxiliary surface and atmospheric data as input. Furthermore, since the atmospheric effect had been considered in the process of radiative simulation, atmospheric correction could be avoided and the TOA radiance is directly linked to the OLR of interest.

Both MODIS and AVHRR data have their unique advantages for the OLR production.

1) MODIS OLR has a much higher spatial resolution than CERES and ERBE, which is a valuable source of data that can help assess the impacts of human activities (e.g., urbanization) (Feng et al., 2015; Grimmond, 2007; Oleson et al., 2015) and local and regional radiation budget related to small-scale anthropogenic and natural processes (e.g., fires) (Elvidge et al., 2015; Hudak et al., 2016; O'Brien et al., 2016).

2) MODIS data provides spectral information at multiple wavelength (bands), giving us an opportunity to estimate the OLR at any bands of interest, and thereby investigating the contributions of different components to the broadband OLR. In fact, the spectrally resolved OLR had shown its advantage in GCM model validation (Huang et al., 2006; Huang et al., 2008; Huang et al., 2007). In our future works, such related issues will be investigated using the MODIS OLR retrieved by the proposed linear model in this study.

3) Compared with the same sensor, the AVHRR OLR developed in this dissertation performs much better than the existing NOAA interpolated OLR product (spatial resolution: 2.5°), with better consistency across long-term time series data records, less uncertainties with CERES and HIRS retrievals, complete data availability up to 35 years (1981 to 2016), and much finer spatial resolution (0.05°).

4) Given the similar estimation accuracy of CERES and HIRS, the current AVHRR OLR datasets uniquely provide long-term and high-resolution resources simultaneously for reliable OLR data, making up for the limitation of either the data availability or the resolution of the former two and facilitating climatic or ecological studies at global or regional scales.

Another issue worth mentioning is the method for converting instantaneous OLR to daily mean OLR. Besides the fitting method introduced in section 3.2.2, in the procedure of algorithm development, an initial attempt had ever been made to construct the conversion relationship based on OLR diurnal curves. In theory, once the instantaneous OLR and the OLR diurnal curve obtained, the daily mean OLR could be calculated. However, both *Terra* and *Aqua*, as well as the NOAA series satellites are sun-synchronous polar-orbiting platforms, and thus enough diurnal samplings are almost impossible for most areas on the earth. Owing to this fact, CERES OLR products were collected as auxiliary data to aid the AVHRR daily mean OLR calculation. First, CERES 3-hourly 1° × 1° OLR product (SYN1deg-3Hour) were collected from 2001 to 2016 and inter-annually temporal average were implemented on these datasets. With that, CERES multi-year mean OLR at 3-hour resolution (hereafter, MYM-3Hour image) could be obtained. To get the OLR diurnal curve of a certain day (Day_{target}), 17-days data (8 days before and after Day_{target}, respectively) were extracted from the MYM-3Hour image. Then, the weighted average OLR over the 17 days was calculated for each sample time point (0:00, 3:00, 6:00……18:00, 21:00) based on Equation 3-2. For the weight defined in Equation 3-3, the logic is that the closer to Day_{target} (d = 9), the larger weight was set for that day; offset 0.5

is added to avoid 0 in divisors. As results, Figure 3-25 plots the weight curves against the days.

$$OLR_{wAvg,t} = \sum_{d=1}^{N} w_d OLR_{d,t}$$

Equation 3-2

$$w_d = \frac{1/\left(|d-9|+0.5\right)}{\sum_{d=1}^{N} 1/\left(|d-9|+0.5\right)}$$

Equation 3-3

Where w_d is the weight of OLR on the d-th day, N is the total number of days and is set as 17 in this study.

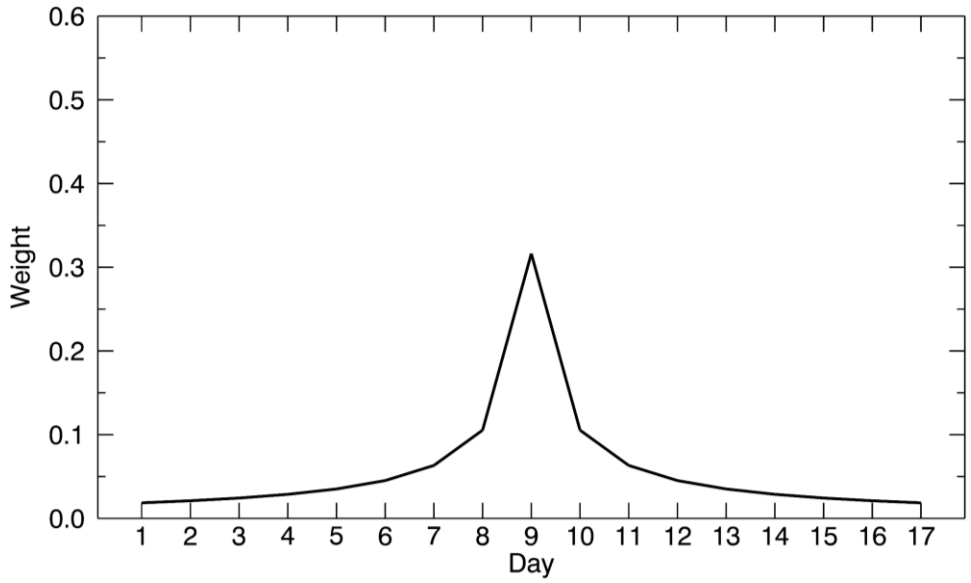

Figure 3-25 The weight set for each day within the 17-days window to calculate weighted average OLR.

By employing temporal filtering technique (e.g., moving average) on those samples, the smoothed OLR diurnal curve at the temporal resolution of ten minutes can be obtained (Figure 3-26a). Combined with the CERES daily mean OLR product (SYN1deg-Day) with same spatial resolution (1° × 1°), the diurnal curve of the ratio coefficient, which is defined

as the daily mean value divided by the instantaneous value at a certain time, can be calculated and archived (e.g., Figure 3-26b). Finally, the LUT of the ratio coefficients can be applied on real AVHRR instantaneous OLR retrieval to estimate the AVHRR daily mean OLR. Unfortunately, according to Figure 3-27, AVHRR daily mean OLR calculated based on the stated diurnal curve method performs much worse by showing much larger extreme differences with CERES daily OLR product, while the current fitting equation based method introduced in section 3.2.2 alleviate such issues to a large extent.

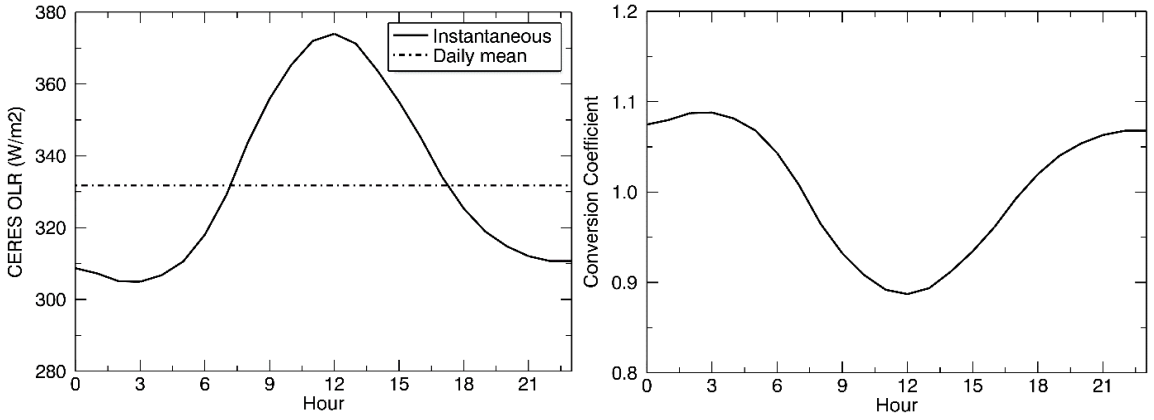

(a) (b)

Figure 3-26 Examples of a) the diurnal curve of CERES OLR and b) the "instantaneous-to-daily mean" conversion coefficients for a desert pixel in Jan 1st.

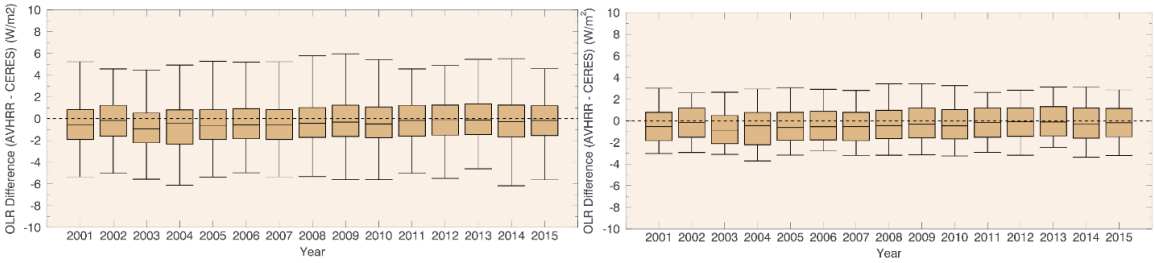

(a) (b)

Figure 3-27 Statistics of the daily-mean OLR differences between AVHRR and CERES in years from 2001 to 2015 in the case of a) diurnal curve method and b) fitting equation method.

Chapter 4 Case studies of OLR: precursors of ENSO and earthquake

As a parameter reflecting the integrated radiative conditions of surface and atmosphere, OLR has been demonstrated the strong response to some well-known climate variations like ENSO and tropical expansion. Analysis presented in Chapter 2 also clearly shows the significant correlation between the OLR anomalies and historical ENSO events. More importantly, OLR has potential to predict abnormal events prior to their occurrence. In this chapter, capability of OLR to predict ENSO and a giant earthquake will be explored using the developed AVHRR daily OLR dataset. In addition, such capabilities will be also compared among different OLR products.

ENSO is the most famous coupled ocean–atmosphere phenomenon which is one of the most important climate events from seasonal to interannual scales (Jin et al., 2008; Philander, 1990). Although originating and developing mainly in the tropical Pacific Ocean, the impacts of ENSO spread outside the original regions on the global climate, the ecology of the tropical Pacific and the economies of many countries (Bradley et al., 1987; Rasmusson and Carpenter, 1982; Ropelewski and Halpert, 1989; Ropelewski and Halpert, 1987; Trenberth et al., 1998). Thus, successful ENSO forecasts can offer an opportunity to management to consider the anticipated climate anomalies, potentially alleviate the social and economic losses of this natural phenomenon. Existing ENSO prediction approaches mainly rely on SST, and the effective and timely forecast of ENSO depends on the availability of accurately predicted SST, as the tropical atmosphere responds to large-scale SST anomalies in a coherent and reproducible way (Jin et al., 2008). Regarding the strategies for predicting SST in the tropical Pacific Ocean, there are three main categories: purely statistical techniques (Graham et al., 1987), combinations of dynamic and statistical

models (Cane et al., 1986; Neelin and Dijkstra, 1995), and purely dynamic models (Kirtman, 2003; Rosati et al., 1997; Schneider et al., 1999; Stockdale et al., 1998). Among those models, comprehensive ocean–atmosphere coupled general circulation models (CGCMs) have been utilized by some major meteorological centers around the world to produce dynamical seasonal forecasts using an ensemble approach (Kanamitsu et al., 2002; Mason et al., 1999). Correlation analysis presented in Chapter 2 suggests that OLR might be another potential index to reflect the abnormal variations on sea surface and atmosphere conditions prior to the occurrence of ENSO, and this chapter will explore the capability of OLR to predict ENSO with the aid of statistical approaches and machine learning methods.

Earthquake is one of the most destructive natural disasters around the world. It is a complex process that is coupled among lithosphere, atmosphere and ionosphere. One of such coupling is the release of radon and other radioactive gases from active tectonic faults around the earthquake epicenter (Chakraborty et al., 2018). This leads to the latent heat release due to a change in the humidity of air, and ultimately results in thermal anomaly in the tropospheric regions (Pulinets and Ouzounov, 2011). Inspired with this fact, Kang and Liu (2001) studied the spatial and temporal variations of OLR before major earthquakes using the method of Eddy field calculation mean and found the radiation to be intense around the epicenter before earthquakes (Liu, 2000). Chakraborty et al. (2018) studied a recent major earthquake occurred in Nepal with Richter scale magnitude of M=7.3 on May 12, 2015 using the NOAA Interpolated OLR product described in section 3.1.5. They found singularities in Eddy field OLR curves around the earthquake epicenter starting three days prior to the earthquake days and disappearance of such singularities after the events. For several other recent giant earthquakes like those at China (M=7.9, 2008), Haiti (M=9.0,

2011), Chile (M=8.8, 2010) and Japan (M=9.0, 2011), strong OLR anomalies were observed 5–6 days prior to the earthquakes (Ouzounov et al., 2007; Pulinets and Ouzounov, 2011; Xiong et al., 2010). In this chapter, the developed high resolution (0.05°) AVHRR daily OLR datasets will be utilized to analyze the Nepal 2015 earthquake and compared with studies in Chakraborty et al. (2018). In addition, China 2008 earthquakes will be also investigated.

4.1 Datasets

4.1.1 SST

The ERSST v4 datasets described in section 2.1.3 are also collected in this chapter. SST is used to identify the historical ENSO events through the criterion that five consecutive records of ONI (refer to section 3.3.4) go above 0.5°C for El Niño in Niño 3.4 or go below -0.5°C for La Niña in Niño 4. Accordingly, Figure 3-23 reports the historical El Niño and La Niña from 1981 to 2016, based on which Table 4-1 lists the periods, durations, and magnitudes (defined as the largest absolute ONI during the event) of those events in the past 36 years.

Table 4-1 Statistics of El Niño and La Niña occurred from 1979 to 2016

El Niño			La Niña		
Period	**Duration**	**Magnitude**	**Period**	**Duration**	**Magnitude**
04/1982-06/1983	15	2.2	09/1983-01/1984	5	1.0
09/1986-02/1988	18	1.7	10/1984-08/1985	11	1.1
05/1991-06/1992	14	1.7	04/1988-04/1989	13	1.8
09/1994-03/1995	7	1.1	08/1998-02/2001	31	1.7
05/1997-05/1998	13	2.4	11/2005-03/2006	5	0.8

06/2002-02/2003	9	1.3	08/2007-07/2008	12	1.6
07/2004-02/2005	8	0.7	11/2008-03/2009	5	0.8
09/2006-01/2007	5	0.9	06/2010-05/2011	12	1.7
08/2009-03/2010	8	1.6	08/2011-03/2012	8	1.0
11/2014-05/2016	19	2.6			

4.1.2 OLR

The AVHRR daily-mean OLR with resolution of 0.05° developed in Chapter 3 is the primary source of OLR data in this chapter. For the ENSO prediction, monthly and three-months running mean OLR anomalies are calculated for the central Pacific region (30°N–30°S, 100°E–60°W) from 1981 to 2016; for the earthquake prediction, OLR around the epicenters in Nepal (2015) are extracted accordingly. In addition, to explore the advantage of the developed high resolution AVHRR OLR, CERES (section 3.1.3) and HIRS (section 3.1.4) daily OLR products are also collected to conduct those predictions for comparisons.

4.2 Methodology

4.2.1 ENSO prediction

In this study, two approaches are tested to predict ENSO using OLR. As a reference, SST will be also fed into the proposed models, and the prediction accuracy will be compared.

4.2.1.1 Extended empirical orthogonal function (EEOF)

The understanding of the mechanism of ENSO is critical to develop the prediction model. In general, ENSO is caused by the abnormal activities of atmospheric conditions caused by variations in SST over the tropical Pacific Ocean. Taking El Niño as an example, the ocean surface in the equatorial eastern Pacific Ocean typically warms by a few degrees Celsius above the long term normal during this period. This occurs because of a change in the winds over the equatorial Pacific. As seen in Figure 4-1, in a normal situation, trade winds along the equator blow strongly from east to west, pushing the surface water from the eastern equatorial Pacific towards the west, where it "piles up". In the eastern Pacific, colder water rises from the deep ocean to the surface to replace the water the winds displaced. This results in a SST difference of about 8°C from west to east. When the trade winds become weaker, less surface water is transported to the west, keeping cooler water deep below the surface in the east. This allows the eastern equatorial Pacific to warm, leading to an El Niño.

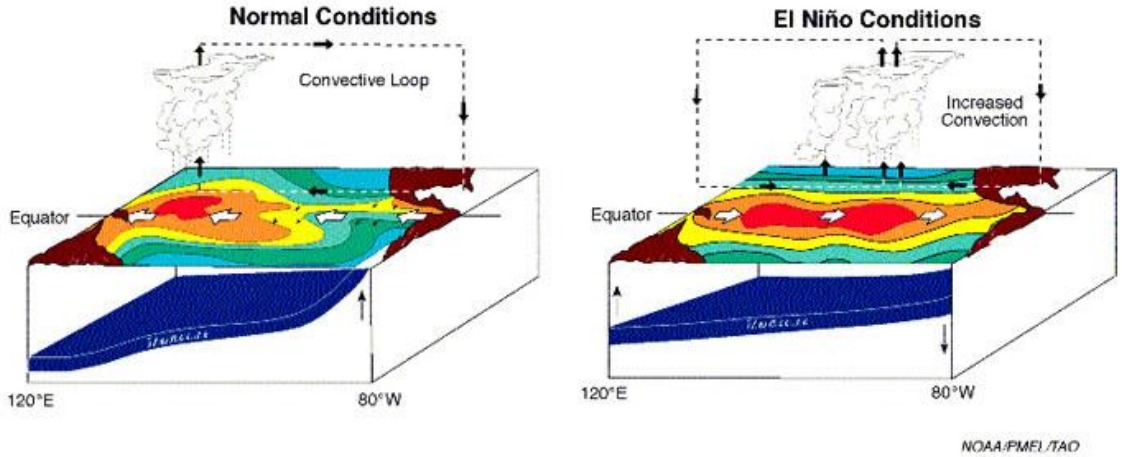

Figure 4-1 The convective circulation during normal and El Niño conditions in the equatorial Pacific Ocean. Image credit: NOAA Pacific Marine Environmental Laboratory.

Since the nature of El Niño, the EEOF technique is an appropriate candidate to characterize the eastward propagation of related atmospheric and sea surface patterns in the wind and sea level pressure that progress from the eastern Indian Ocean across the Pacific. Ordinary EOF have been applied in various oceanic and atmospheric studies in the past few decades. Basically, EOF analysis calculates the orthogonal linear combinations of variables that contribute to the maximum possible amount of variance in a dataset (Graham et al., 1987). It decomposes a space-time field into spatial patterns and associated time indices. The most advantage of this technique is that the first few principles or modes often describe the most important patterns of data variability, thus the data set can be compressed from the original number of points to the number of EOF modes retained without compromising much of such data variability. EOF analysis is also a valuable tool in exploratory data analysis, allowing the dominant interrelationships between data to be highlighted (Graham et al., 1987). Mathematic details of EOF transformation can be referred to Fukuoka (1951) and Lorenz (1956), and comprehensive discussions of this technique may be found in Davis (1978) and Barnett and Hasselmann (1979). In this study, the input matrix of EOF is created with the developed AVHRR OLR within the central Pacific Ocean (30°N~30°S, 100°E~80°W) based on the period from 1981 to 2016. In detail, let X (t, s) (Equation 4-1) denotes a gridded data set composed of a space-time filed representing the OLR value at time t and spatial position s. The value of OLR at discrete time t_i and grid point s_j is then denoted x_{ij} for i = 1, ….., n and j = 1, ….., p. As a result, Figure 4-2 shows the first mode of EOF transformation. As analyzed for Figure 3-22a in section 3.3.4, this mode is exactly the spatial pattern of OLR anomaly responding to El Niño, demonstrating that the El Niño is the dominant controller of variations in the tropical Pacific regions.

$$X = (x_1, x_2, \dots, x_n)^T = \begin{pmatrix} x_{11} & x_{12} & \cdots & x_{1p} \\ x_{21} & x_{22} & \cdots & x_{2p} \\ \vdots & \vdots & \vdots & \vdots \\ x_{n1} & x_{n2} & \cdots & x_{np} \end{pmatrix}$$

Equation 4-1

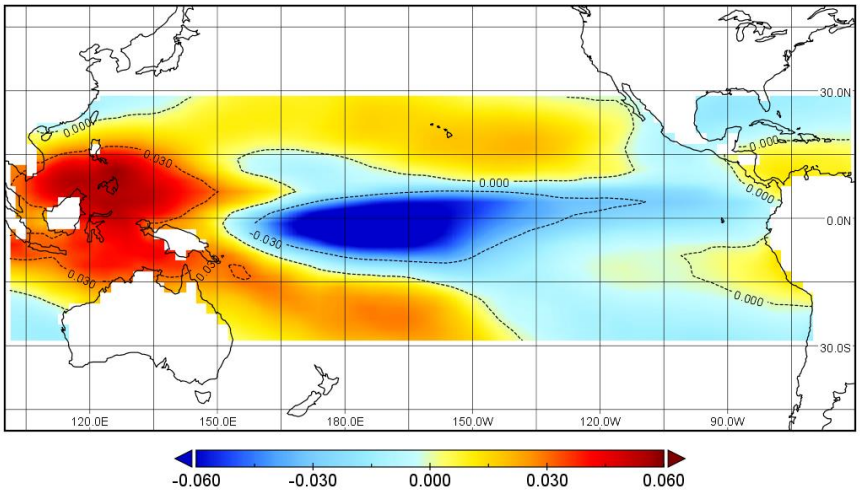

Figure 4-2 The first mode of the EOF transformation of OLR anomaly within the central Pacific Ocean based on the period from 1981 to 2016.

However, EOF cannot deal with propagating features, as the matrix only uses spatial correlation between different grid points of the studied field but forgets about any lagged information. For the aim of ENSO prediction, it is necessary to use both spatial and temporal information to identify the evolution of spatial patterns through time. Accordingly, the EEOF introduced by Weare and Nasstrom (1982) is utilized to serve the purpose. Mathematic details of EEOF can be referred to Hannachi et al. (2007). Following this idea, an EEOF transformation was employed on the time-lag incorporated spatial-temporal matrix of OLR within the equatorial Pacific Ocean (5°N~5°S, 100°E~80°W) based on the period from 1981 to 2016. The eigenvalue of the first 50 ranked modes is reported in Figure 4-3. The first two modes explicitly explain the El Niño and La Niña, and more interestingly, the fourth mode (explains about 5% of variance) is found to display strong propagation patterns of OLR anomaly across the equatorial Pacific from west to east. Figure 4-4 shows

EEOF 4 along zonal (5°N~5°S) mean as a function of time lag; this sort of diagram where space and time axes are shown is known as Hövmoller diagram (Hovmöller, 1949). Figure 4-4, clearly presents two facts: 1) OLR positive anomaly propagates from west Pacific (~130°E) to east Pacific (~100°W) within a 12-month period (the blue arrow), which is an typical spatial-temporal variation from El Niño to La Niña; 2) Around the Niño 3.4 region, the OLR anomaly has an obvious change from strongly positive to strongly negative within the 12-month period (the white arrow), suggesting a typical occurrence procedure of El Niño. Quantitatively, the decreasing speed of the normalized OLR anomaly is about 0.05/12-month. This is also the key to carry out the ENSO prediction in this study.

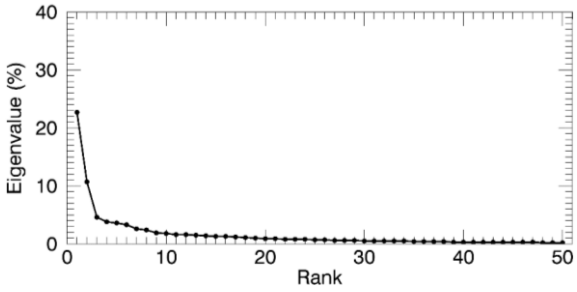

Figure 4-3 Eigenvalue of the first 50 modes of the EEOF transformation of OLR within the central Pacific Ocean.

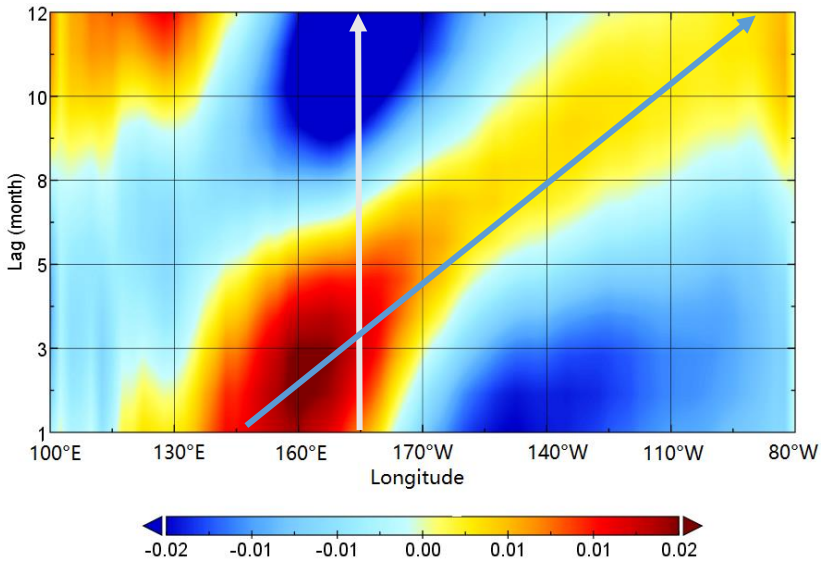

Figure 4-4 Hövmoller diagram of the mode 4 of the OLR EEOF transformation along the equatorial Pacific Ocean.

Based on Table 4-1, taking El Niño for example, it is known that ten El Niño events had occurred between 1981 to 2016. For each of these events, the most recent 12-month equatorial Pacific OLR data is extracted to construct the spatial-temporal matrix described above. Then the EEOF transformation is conducted and the Hövmoller diagram like Figure 4-4 is created, and from such a diagram, the speed of OLR anomaly changing along Niño 3.4 region can be calculated. From the set of those speeds of all the ten El Niño, the minimum one will be taken as the threshold for the prediction purpose. In the process of prediction, it can be assumed that each time the ONI_{OLR} decreases to be negative potentially indicates a beginning of El Niño (positive for La Niña). Then, the most recent 12-months equatorial Pacific OLR will be extracted to perform EEOF transformation and to calculate the changing speed of OLR anomaly in Niño 3.4 region. The final step is to identify if the current OLR decreasing will evolve to a real El Niño based on the defined threshold above.

4.2.1.2 Artificial neural network (ANN)

Machine learning (ML) always has special advantage to handle complex problems of which the physical mechanisms are not clear enough. In this study, a widely used ML model, the artificial neural network (ANN) is employed to conduct the ENSO prediction, as well as quantifying the relative magnitude of each event. To obtain the training data, Figure 3-23 is referred to extract historical ENSO events identified by ONI_{SST}, and for each one, the most recent 12-month equatorial Pacific OLR data is gathered. Then, from the west to the east equatorial Pacific, the changing trend of OLR anomaly (base period is from 1981 to the current studied year) within the 12-month for each grid is calculated and fed into the ANN model with 1 hidden layer. The dependent variables are the binary result of ENSO occurrence (0 or 1) and magnitude of the events shown in Table 4-1.

4.2.2 Earthquake prediction

Various methods have been proposed for analyzing daily/monthly variation of OLR. Among them, Eddy field calculation mean is a method which detects the presence of any spatial singularities in OLR between adjacent points within the epicenter region (Kang and Liu, 2001; Liu, 2000). The Eddy value is defined as "the total sum of the difference" of "the measured value" of OLR, its expression is:

$$S_d^*(x_{i,j}, y_{i,j}) = 4 * \mathrm{S}(x_{i,j}, y_{i,j}) - \left[\mathrm{S}(x_{i-1,j}, y_{i,j}) + \mathrm{S}(x_{i,j}, y_{i,j-1}) + \mathrm{S}(x_{i+1,j}, y_{i,j}) + \mathrm{S}(x_{i,j}, y_{i,j+1})\right]$$

Equation 4-2

Where $S_d^*(x_{i,j}, y_{i,j})$ is the daily OLR Eddy field; $\mathrm{S}(x_{i,j}, y_{i,j})$ is the daily OLR value in the grid located in *i*th column and *j*th row. For a studied earthquake event, a 10°×10° of latitude by longitude window centered with the epicenter is extracted for the Eddy field calculation through Equation 4-2. Such a window is repeatedly calculated within ±5 days relative to the recorded earthquake day, and the spatial and temporal singularity of the Eddy fields are interpreted and analyzed.

4.3 Results and discussion

4.3.1 ENSO prediction

In theory, the most rigorous test of the proposed ENSO prediction models should be conducted by verifying the predicted results derived from the current OLR data and the actual ENSO occurrence in the future. However, that is difficult and unreasonable for algorithm development in a research. An alternative way is to design the validation experiments based on historical ENSO records. In detail, based on Figure 3-23, each time

point at which the ONI_{SST} increases to positive (or re-increase from positive) will be first considered as the beginning of a potential El Niño (opposite cases for La Niña). Then the EEOF and ANN methods described in section 4.2 will be employed on the equatorial OLR data of the most recent 12-month of the current studied time point. Output will be the Yes/No binary results regarding the occurrence of ENSO from the both methods and the relative magnitude of each identified ENSO event from the ANN method.

Figure 4-5 display the binary prediction results from the developed AVHRR OLR data. Circles in the top line denotes all the starting time points that have potential to evolve to ENSO events, with red for El Niño and blue for La Niña. For those points, both EEOF and ANN methods are employed on and the predicted results are listed in the second (triangle) and third (diamond) line, respectively. As a reference, the squares in the bottom line mark the actual ENSO historical records accordingly to Table 4-1. In general, both methods can well identify ENSO events and exclude non-ENSO events for which the OLR anomaly displayed trends of ENSO but didn't go beyond the threshold value stated in section 3.3.4. Quantitatively, Table 4-2 to Table 4-5 report the confusion matrix of the prediction results for El Niño and La Niña using the EEOF and ANN methods, respectively. It is found that both the methods predict El Niño slightly better than La Niña, and ANN performs slightly better than EEOF. In addition, by comparing Figure 3-23 and Figure 4-5, it is found that the omitted El Niño (starting from 07/2004) by EEOF has the minimum magnitude (0.7, see in Table 4-1) among all the El Niño records; the omitted La Niña (starting from 10/1984) by both methods also has a relatively small magnitude (1.1) among all the La Niño records. On the other hand, the committed El Niño and La Niña have magnitudes that are quite close to the threshold line. These facts indicate that the deficiency

of the two methods are mainly attributed to the marginal cases that are prone to be miss classified due the nature of the methods. Besides the binary prediction result, ANN also calculates the absolute magnitude of each ENSO event at the same time. Figure 4-6 shows the comparison between the predicted and the referenced magnitudes according to Table 4-1. The statistics demonstrates the quite good performance of ANN to capture the historical ENSO magnitude based on OLR.

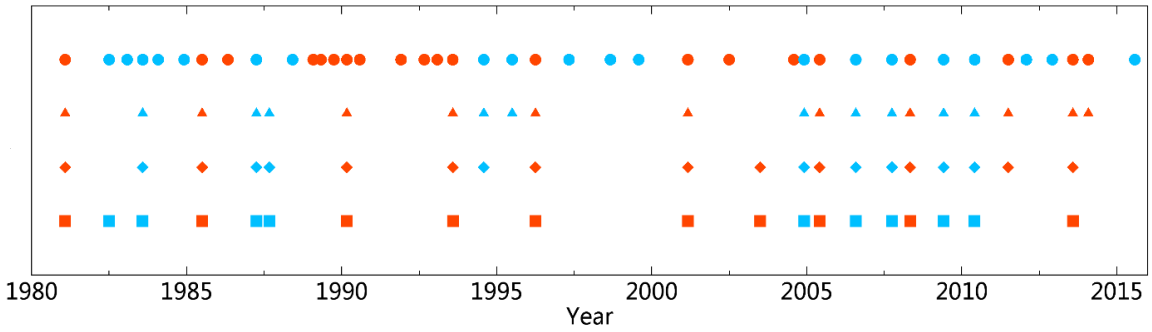

Figure 4-5 Prediction results of the occurrence of ENSO from 1981 to 2016 using EEOF (triangle) and ANN (Diamond) methods based on AVHRR OLR. Circles in the top line mark all the potential starting time points for ENSO. Squares in the bottom line mark the actual ENSO events based on Table 4-1.

Table 4-2 Confusion matrix of the El Niño prediction using EEOF method from AVHRR OLR data

Prediction	**Reference**		**Commission. Err. (%)**
	El Niño	**Non-El Niño**	
El Niño	9	2	18.2
Non-El Niño	1	9	
Omission. Err. (%)	10.0		
Overall Accuracy: 85.7%; **Kappa**: 0.75			

Table 4-3 Confusion matrix of the La Niña prediction using EEOF method from AVHRR OLR data

Prediction	**Reference**		**Commission. Err. (%)**
	La Niña	**Non-La Niña**	
La Niña	8	1	11.1
Non-La Niña	1	6	
Omission. Err. (%)	11.1		
Overall Accuracy: 87.5%; **Kappa**: 0.77			

Table 4-4 Confusion matrix of the El Niño prediction using ANN method from AVHRR OLR data

Prediction	Reference		Commission. Err. (%)
	El Niño	Non-El Niño	
El Niño	10	1	9.1
Non-El Niño	0	10	
Omission. Err. (%)	0.0		
Overall Accuracy: 95.2%; **Kappa**: 0.91			

Table 4-5 Confusion matrix of the La Niña prediction using ANN method from AVHRR OLR data

Prediction	Reference		Commission. Err. (%)
	La Niña	Non-La Niña	
La Niña	8	1	11.1
Non- La Niña	1	6	
Omission. Err. (%)	11.1		
Overall Accuracy: 87.5%; **Kappa**: 0.77			

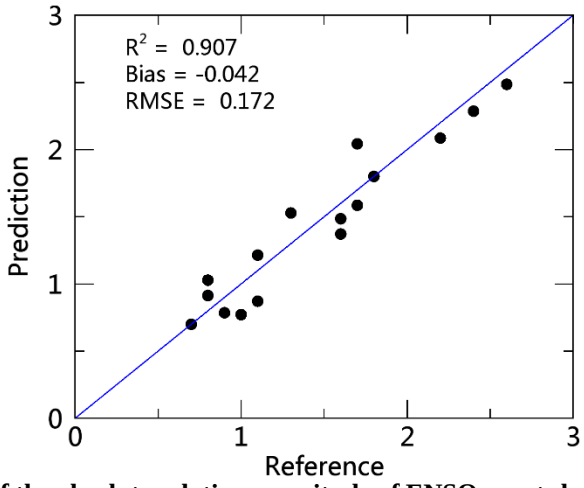

Figure 4-6 Comparison of the absolute relative magnitude of ENSO events between the prediction and reference data.

In order to exam if SST also plays as an effective indicator for predicting ENSO and manifest possible advantage of OLR, the described two prediction methods are also implemented on SST as a reference. Furthermore, the synthetic information from OLR and SST are extracted by using the maximum normalized anomaly between the two indicators to form the spatial-temporal matrix and are fed into the prediction models. Table 4-6 lists

related statistics of such experiments. It is found that OLR performs slightly better than SST for both El Niño and La Niña regardless which method is used, likely because OLR contains the integrated information of surface and atmosphere conditions. Meanwhile, the synthetic information achieves equal or even better prediction accuracy than OLR alone, suggesting that SST also has its own advantage at least for few events which OLR omitted or committed.

Furthermore, to exam if the developed high resolution AVHRR OLR data has any advantage over other existing OLR products, the same procedure described above were implemented on monthly OLR data from CERES EBAF (section 2.1.1.1), HIRS (section 2.1.1.2), and NOAA Interpolated OLR (section 3.1.5), respectively. The prediction accuracy is also reported in Table 4-6. It is seen that AVHRR performs better than the other three OLR data in general. HIRS is very close to AVHRR by showing similar statistics for most cases except for La Niña prediction using EEOF method. The NOAA interpolated AVHRR OLR is obviously inferior to the developed AVHRR and HIRS for all cases. CERES performs worst among them according to the statistics. However, it doesn't indicate large differences between CERES and AVHRR and HIRS OLR data; it is attributed to the shorter period of the CERES data availability, due to which only ENSO events occurred after 2000 can be included in the accuracy assessment. In this situation, a same misidentified event degrades the accuracy statistics more than that of other long-term OLR datasets which are available from 1980s. Setting aside CERES, it is concluded that the developed high resolution AVHRR OLR shows advantage over other long-term OLR record on the ENSO prediction using both EEOF and ANN methods.

Table 4-6 Statistics of ENSO prediction under different methods and information sources

			OLR-based				SST-based	Synthetic
			AVHRR	CERES	HIRS	NOAA Interpolated		
EEOF	**El Niño**	**OA**	85.7	75.0	85.7	80.9	80.9	90.5
		Kappa	0.75	0.58	0.75	0.68	0.68	0.83
	La Niña	**OA**	87.5	87.5	81.2	75.0	81.2	87.5
		Kappa	0.77	0.76	0.68	0.59	0.68	0.77
ANN	**El Niño**	**OA**	95.2	75.0	95.2	90.5	85.7	95.2
		Kappa	0.91	0.58	0.91	0.83	0.75	0.91
	La Niña	**OA**	87.5	75.0	87.5	81.2	81.2	93.8
		Kappa	0.77	0.60	0.77	0.68	0.68	0.88
	Combined	R^2	0.91	0.84	0.90	0.88	0.891	0.921
		Bias	-0.04	-0.55	-0.04	-0.05	-0.058	-0.040
		RMSE	0.17	0.22	0.18	0.20	0.233	0.168

***OA: overall accuracy (%)**

4.3.2 Earthquake prediction

The investigated earthquake in this study is the one occurred in Nepal on May 12th, 2015 at 07:05 UTC with a magnitude of Mw = 7.3. The location of the epicenter was at 27.809°N, 86.066°E (southeast of Kodari) and the depth was 19 km (http://www.usgs.gov/) (Figure 4-7). The epicenter was on the same fault as the larger magnitude 7.8 earthquake of April 25th, 2015, but further east than the original quake, so it is considered to be an aftershock of the April 25th quake (USGS, 2015). This shock caused mass damages and casualties in Nepal: at least 153 people were killed by the earthquake and more than 3,200 people were injured, primarily in mountain regions of the northeast. As of May 15th, 1,700 people were still receiving treatment for their injuries. Thirty-two of the nation's seventy-five districts were affected by the quake (https://indianexpress.com/article/india/fresh-tremors-in-delhi-and-ncr/).

Figure 4-7 Location of the epicenter of the earthquake occurred in Nepal on May 12th, 2015. Epicenter is marked by the red point.

Figure 4-8 represents the Eddy field variation around the earthquake epicenters generated from the developed AVHRR daily OLR data. From May 7, 2015, there is a presence of slightly higher Eddy field OLR around the epicenter. Such anomalies got intensified from May 9, three days prior to the earthquake day. On the next two days (May 10th and 11th), the field singularities became very strong and gradually spread towards the epicenter. On May 12th, the earthquake day, it has become less prominent but the intensification showed again on May 14th-15th, which was a precursor of the major aftershock on May 16th. After the aftershock, the Eddy field dissolves away from May 16th to May 18th. Such intensification of the field three days prior to the earthquake day and its fading away after the aftershock can be associated with the chemical channel responsible for the lithosphere atmosphere ionosphere coupling mechanisms (Chakraborty et al., 2018).

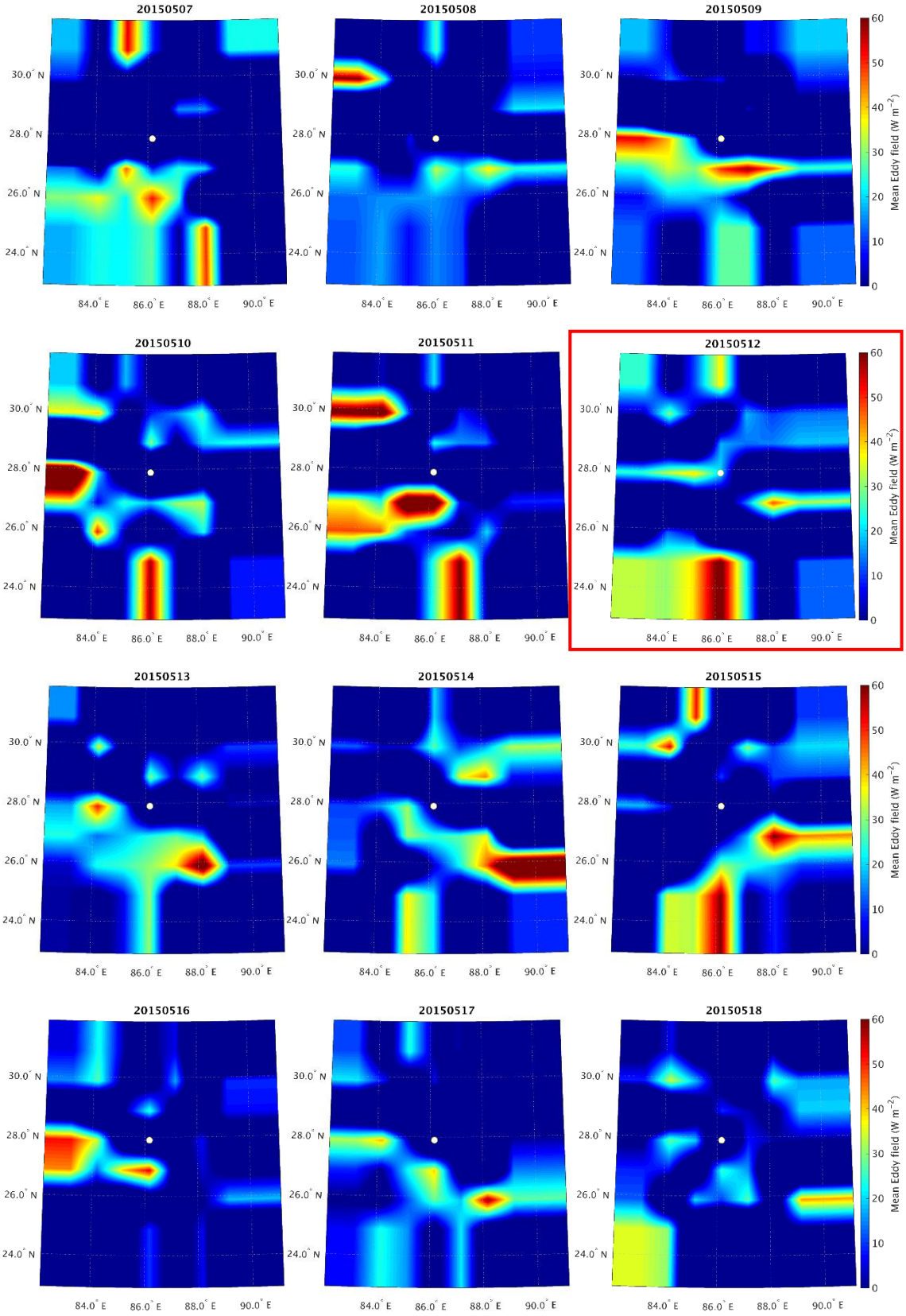
20150507
20150508
20150509
20150510
20150511
20150512
20150513
20150514
20150515
20150516
20150517
20150518
30.0° N
28.0° N
26.0° N
24.0° N
84.0° E
86.0° E
88.0° E
90.0° E
Mean Eddy field (W m⁻²)
0
10
20
30
40
50
60

Figure 4-8 Eddy field mean of AVHRR OLR around the earthquake epicenters during May 7 to May 18, 2015 with a spatial span of latitudes 23°N to 32°N and longitudes 82°E to 91°E. The epicenters are marked by white circles. The earthquake day is marked by the red color box. The color bar represents the intensity of the mean Eddy field in W/m^2

In addition to the visual interpretation of the Eddy field variation in Figure 4-8, Figure 4-9 displays such variations in a quantitative way by averaging the positive Eddy values within the investigated spatial domain. It testifies the analysis above: there is an obvious increasing trend from May 8th to May 11th; then drops down in the earthquake day (May 12th) and the following day (May 13th); the re-intensification on May 14th and 15th indicate the aftershock on May 16th; then the anomalies went away from May 16th to 18th. Chakraborty et al. (2018) conducted similar studies using the NOAA interpolated AVHRR OLR with the spatial resolution of 2.5°, and similar trends of Eddy field variation were observed. To make a comparison, such OLR datasets (see in section 3.1.5) were collected and the Eddy field calculation was implemented. As seen in Figure 4-9, the two curves show coincident trends during the selected time window. However, the curve from the developed AVHRR OLR has much larger magnitude of variation than that of the NOAA interpolated OLR. This is reasonable because the former one has much higher spatial resolution, leading to more drastic spatial contrast than the latter one. Considering that the OLR-based prediction of earthquake depends on the temporal anomaly of the spatial contrast, the developed AVHRR OLR is more sensitive to the coming earthquake than the existing NOAA AVHRR OLR products, thereby a superior indicator for the earthquake forecasting.

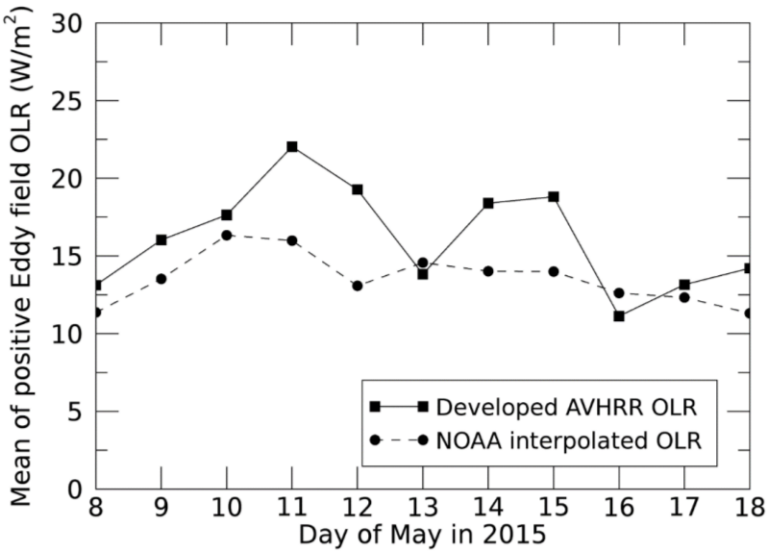

Figure 4-9 Variations of the average positive Eddy field OLR around the epicenter (10° × 10°) of the earthquake occurred in Nepal 2015

4.4 Conclusions

Successful ENSO prediction facilitates the decision makers to anticipate the climate anomalies and get well prepared for potential social and economic impacts of this natural phenomenon. Existing ENSO prediction approaches mainly relied on SST. Regarding the algorithms, there are three main categories of strategies including purely statistical techniques, combinations of dynamic and statistical models, and purely dynamic models. This chapter tests two approaches for predicting ENSO: the EEOF method takes use of the mechanism of ENSO formation and interpret the evolution of spatial pattern against time; while the ANN method shows the special advantage of ML technique on the problems that have complicated physical process. Both methods capture most of the historical ENSO record from 1981 to 2016 and have capability to filter out non-ENSO events. Between the two components of ENSO, it is found that both the methods predict El Niño slightly better than La Niña, likely due to that El Niño has relatively stronger signal as the active part of ENSO. Regarding the two methods, ANN performs slightly better than EEOF, although

the difference is not significant considering the total number of testing sample is limited. By changing the source information fed into the prediction model, it is found that OLR achieves comparable prediction with that of SST; the slightly higher accuracy from OLR is likely because OLR contains the integrated information of surface and atmosphere conditions, suggesting the potential of OLR as another effective index to identify and monitor ENSO in future studies. Among different OLR datasets, it is found that the developed high resolution AVHRR OLR performs better than the other two long-term OLR record, HIRS OLR and NOAA interpolated AVHRR OLR, in general.

Anomalies in the thermal infrared emission from the earth surface is one of the remarkable phenomena that have been widely reported to occur prior to major earthquakes. These anomalies are typically observed a few days to a week before the primary shocks and may linger on into the aftershock period (Shah et al., 2018). The underlying mechanism is that prior to an earthquake, an unbalanced heat exchange forms between earthquake breeding zones and the air column, and gases and water vapor emanating from the ground in pre-seismic regions lead to the OLR anomaly (Shah et al., 2018). In this chapter, the developed AVHRR OLR data was utilized to test such a theory on the well-known earthquake occurred in Nepal on May 12th, 2015. Results indicated that the Eddy field OLR displayed significant intensification three days prior to the earthquake day. As a comparison, the developed AVHRR OLR showed much stronger Eddy filed anomaly than the existing NOAA interpolated AVHRR OLR, suggesting that the former one as a better indicator for the earthquake prediction.

Chapter 5 Conclusions

Outgoing longwave radiation (OLR) is one of the key components of the Earth's energy budget, which can explain the overall status of the global atmospheric system. Multiple OLR products have been developed since the satellite remote sensing era. However, inconsistencies and discrepancies exist among various OLR datasets. This dissertation first quantified the magnitude of such differences and their spatial and temporal pattern; then, an algorithm framework was developed to generate more reliable and more useful OLR estimates from multi-spectral satellite observation; last, the developed OLR data were employed to predict climate (ENSO) and geological (earthquake) anomalies. Major findings of this dissertation are listed below.

5.1 Major findings

Inter-comparisons among multiple OLR products show that HIRS OLR and NCEP-NCAR OLR have the best agreement with CERES EBAF OLR product among the examined satellite OLR products and reanalysis OLR data, respectively. The two reanalysis OLR estimates from JRA-25 and JRA-55 are larger than CERES OLR by up to ~15 W/m^2 and ~12 W/m^2, respectively. For TOA longwave radiation, such biases are too large to be compatible within climatic models. In addition, all OLR products display strong response to the poleward tropical expansion and ENSO during the investigated period from 1981 to 2016. HIRS and NCEP-NCAR show the greatest capabilities to capture these two climate anomalies among the examined satellite and reanalysis OLR products, respectively.

The developed OLR algorithm framework can well generate reliable OLR estimates from multi-spectral remotely sensed data including MODIS and AVHRR.

Comparisons with CERES data at different spatial and temporal scales demonstrate that the MODIS and AVHRR instantaneous OLR estimates have comparable accuracy with CERES instantaneous OLR. For the AVHRR long-term daily mean OLR record, it also achieves high agreements with CERES daily OLR (SYN1deg-Day) product. Moreover, AVHRR monthly composited OLR is consistent with CERES and HIRS monthly OLR products, while NOAA interpolated AVHRR ORL products presented larger differences with the other three.

Taking OLR as an index, both the EEOF and ANN methods capture most of the historical ENSO record from 1981 to 2016 well and have capability to filter out non-ENSO events. It is found that both methods predict El Niño slightly better than La Niña, likely due to that El Niño has relatively stronger signal as the active part of ENSO. In addition, ANN performs slightly better than EEOF, although the difference is not significant considering the total number of testing samples is limited. Furthermore, it is found that OLR achieves comparable prediction with that of SST; the slightly better prediction from OLR owes to that OLR contains the integrated information of surface and atmosphere conditions which better couples with the mechanism of ENSO, suggesting the potential of OLR as another effective index to identify and monitor ENSO. Among different OLR datasets, it is found that the developed high resolution AVHRR OLR performs better than the other two long-term OLR record, HIRS OLR and NOAA interpolated AVHRR OLR, in general. Regarding the OLR and earthquakes, the Eddy field OLR showed significant intensification three days prior to the earthquake day, and the developed AVHRR OLR showed much stronger Eddy filed anomaly than the existing NOAA interpolated AVHRR OLR, suggesting that the former one as a better indicator for the earthquake prediction.

5.2 Major contributions

In this dissertation, the thoroughly inter-comparisons among various OLR datasets will contribute as a reference for peers in the climate community who use OLR as one of inputs in their climate models or other diagnostic purpose. The developed OLR algorithm framework could be utilized to estimate OLR from multi-spectral satellite data. This study also demonstrates that OLR is a promising indicator to predict ENSO and giant earthquakes, which has implications for decision makers to alleviate the impacts on life and property from these extreme climate variations through some preventive measures such as releasing weather alert and conducting evacuations.

Specifically: 1) Comprehensive inter-comparisons and evaluations on multiple OLR products and datasets demonstrate that most of them have similar spatial pattern of variation and temporal anomaly, resulting in close capability to capture tropical expansion and ENSO events. However, the two JRA reanalysis OLR, JRA-25 and JRA-55, are found to be significantly differ from others. 2) The developed MODIS 1km OLR has a much higher spatial resolution than CERES and ERBE, which is a valuable source of data that can help assess the impacts of human activities and local and regional radiation budget related to small-scale anthropogenic and natural processes. 3) The AVHRR OLR developed in this dissertation outperforms the existing NOAA interpolated OLR product, with better consistency across long-term time series data records, less uncertainties with CERES and HIRS retrievals, complete data availability up to 35 years (1981 to 2016), and much finer spatial resolution (0.05°). Moreover, given the similar estimation accuracy of CERES and HIRS, the current AVHRR OLR datasets uniquely provide long-term and high-resolution resources simultaneously for reliable OLR data, making up for the

limitation of either the data availability or the resolution of the former two and facilitating climatic or ecological studies at global or regional scales. The produced AVHRR OLR was used in Song et al. (2018) to characterize the energy budge at TOA at a long-term scale. 4) OLR is taken as the index to predict ENSO based on EEOF and ANN methods. Results shows slight advantage of OLR over SST to achieve this goal, suggesting the potential of OLR as another effective index to identify and monitor ENSO thanks to its nature that contains the integrated information of surface and atmosphere conditions which better couples with the mechanism of ENSO. In addition, the developed high resolution AVHRR OLR performs better than the other two long-term OLR record, HIRS OLR and NOAA interpolated AVHRR OLR, in general.

5.3 Future directions

This dissertation is a systematic study on OLR including the algorithm development, validation and evaluation, and case study using OLR. Although most critical issues have been explored and discussed in this study, several issues are still remained to be investigated in the future: 1) MODIS data provides a valuable source of spectral information at multiple wavelength (bands), facilitating the estimation the OLR at any bands of interest, and thereby investigating the contributions of different components to the broadband OLR. In fact, the spectrally resolved OLR had shown its advantage in GCM model validation (Huang et al., 2006; Huang et al., 2008; Huang et al., 2007). In future works, such related issues will be investigated using the MODIS OLR retrieved by the proposed linear model in this study. 2) The OLR from JRA-25 and JRA-55 are larger than that from CERES and other OLR products by more than 10 W/m^2, which is unacceptable for climatic studies. The longwave radiation schemes employed in these two projects may

need to be revisited in the future. Moreover, further efforts are required for global OLR studies, in terms of building more accurate OLR products from more reliable satellite observations and better algorithms for validation and evaluating both satellite retrieval and reanalysis OLR using more extreme climatic events such as hurricanes as well as forest fires, extensive urbanization, etc. 3) OLR shows its potential to predict ENSO slightly better than SST based on historical ENSO records. However, it is better to verify the proposed OLR-based models with the real occurrence of future ENSO events. Moreover, it is worth to explore the physical mechanism of OLR responding to ENSO deeper, which will fundamentally support the OLR as a regular indicator for ENSO monitoring and prediction.

Glossary

ABI	Advanced Baseline Imager
ADM	Angular Distribution Model
AER	Atmospheric and Environmental Research
AIR	Atmospheric Infrared Sounder
ANN	Artificial Neural Network
ASR	Absorbed Incoming Solar Radiation
CDR	Climate Data Record
CERES	Clouds and the Earth's Radiant Energy System
CGCM	Coupled General Circulation Models
CM SAF	Satellite Application Facility on Climate Monitoring
CPC	Climate Prediction Center
DJF	December-January-February
DOY	Day of Year
DSR	Downward Solar Radiation
EBAF	Energy Balanced and Filled
EEOF	Extended Empirical Orthogonal Function
ENSO	El Niño/Southern Oscillation
EOF	Empirical Orthogonal Function
EOS	Earth Observing System
EOT	Empirical Orthogonal Teleconnections
ERA-Interim	ECMWF Interim Reanalysis
ERB	Earth's Radiation Budget
ERBE	Earth Radiation Budget Experiment
ERSST	Extended Reconstructed Sea Surface Temperature
EUMETSAT	European Organization for the Exploitation of Meteorological Satellites
GAC	Global Area Coverage
GCM	General Circulation Model
GEOS	Geostationary Operational Environmental Satellite
GERB	Geostationary Earth Radiation Budget

GESDISC	Goddard Earth Sciences Data Information and Services Center
GEWEX	Global Energy and Water Cycle Experiment
GMAO	Global Modeling and Assimilation Office
GMT	Greenwich Mean Time
GSFS	Goddard Space Flight Center
HIRS	High-Resolution Infrared Radiation Sounder
IAU	Incremental Analysis Update
ICOADS	International Comprehensive Ocean-Atmosphere Dataset
ISCCP	International Satellite Cloud Climatology Project
JJA	June-July-August
JMA	Japan Meteorological Agency
JRA-25	Japanese 25-Year Reanalysis
JRA-55	Japanese 55-Year Reanalysis
LT	Local Time
LTDR	Land Long-term Data Record
LUT	Look Up Table
MAM	March-April-May
MERRA	Modern-Era Retrospective Analysis for Research and Applications
ML	Machine Learning
MSG	METEOSAT Second Generation
NASA	National Aeronautics and Space Administration
NCAR	National Center for Atmospheric Research
NCEP	National Centers for Environmental Prediction
NH	North Hemisphere
NOAA	National Oceanic and Atmospheric Administration
NWS	National Weather Service
OLR	Outgoing Longwave Radiation
ONI	Oceanic Niño Index
PCS	Principal Component Score
POES	Polar Orbiting Platforms
PSD	Physical Science Division

RMSD	Root-Mean-Squared-Deviation
RMSE	Root Mean Square Error
RRTM	Rapid Radiation Transfer Model
RRTMG-LW	Rapid Radiation Transfer Model for Global Models – Longwave
RT	Radiative Transfer
SH	South Hemisphere
SON	September-October-November
SRF	Spectral Response Function
SSF	Single Scanner Footprint
SST	Sea Surface Temperature
SSTA	SST Anomaly
SW	Shortwave
TIR	Thermal Infrared
TOA	Top of Atmosphere
TOT	Total Channel
USR	Upward Shortwave Radiation
VZA	View Zenith Angel
WN	Window Channel

References

Abel, P., Gruber, A., 1979. An improved model for the calculation of longwave flux at 11 micrometers. NOAA Technical Report, NESS 106, NTIS PB80-119431, 24 pp.

Allan, R.P., Ringer, M.A., Pamment, J.A., Slingo, A., 2004. Simulation of the Earth's radiation budget by the European Centre for Medium-Range Weather Forecasts 40-year reanalysis (ERA40). Journal of Geophysical Research: Atmospheres 109.

Aumann, H.H., Chahine, M.T., Gautier, C., Goldberg, M.D., Kalnay, E., McMillin, L.M., Revercomb, H., Rosenkranz, P.W., Smith, W.L., Staelin, D.H., 2003. AIRS/AMSU/HSB on the Aqua mission: Design, science objectives, data products, and processing systems. IEEE Transactions on Geoscience and Remote Sensing 41, 253-264.

Ba, M.B., Ellingson, R.G., Gruber, A., 2003. Validation of a technique for estimating OLR with the GOES sounder. Journal of Atmospheric and Oceanic Technology 20, 79-89.

Bamston, A.G., Chelliah, M., Goldenberg, S.B., 1997. Documentation of a highly ENSO-related sst region in the equatorial pacific: Research note. Atmosphere-ocean 35, 367-383.

Barkstrom, B., Harrison, E., Smith, G., Green, R., Kibler, J., Cess, R., 1989. Earth radiation budget experiment (ERBE) archival and April 1985 results. Bulletin of the American Meteorological Society 70, 1254-1262.

Barkstrom, B.R., 1984. The earth radiation budget experiment (ERBE). Bulletin of the American Meteorological Society 65, 1170-1185.

Barnes, W.L., Pagano, T.S., Salomonson, V.V., 1998. Prelaunch characteristics of the moderate resolution imaging spectroradiometer (MODIS) on EOS-AM1. Geoscience and Remote Sensing, IEEE Transactions on 36, 1088-1100.

Barnett, T., Hasselmann, K., 1979. Techniques of linear prediction, with application to oceanic and atmospheric fields in the tropical Pacific. Reviews of Geophysics 17, 949-968.

Bass, B., Hansell, R., Choi, J., 1998. Towards a simple indicator of biodiversity. Environmental Monitoring and Assessment 49, 337-347.

Berk, A., Anderson, G.P., Acharya, P.K., Bernstein, L.S., Muratov, L., Lee, J., Fox, M., Adler-Golden, S.M., Chetwynd Jr, J.H., Hoke, M.L., 2006. MODTRAN5: 2006 update, Defense and Security Symposium. International Society for Optics and Photonics, pp. 62331F-62331F-62338.

Betts, A.K., Zhao, M., Dirmeyer, P., Beljaars, A., 2006. Comparison of ERA40 and NCEP/DOE near-surface data sets with other ISLSCP-II data sets. Journal of Geophysical Research: Atmospheres 111.

Bloom, S., Takacs, L., Da Silva, A., Ledvina, D., 1996. Data assimilation using incremental analysis updates. Monthly Weather Review 124, 1256-1271.

Borbas, E., Seemann, S.W., Huang, H.-L., Li, J., Menzel, W.P., 2005. Global profile training database for satellite regression retrievals with estimates of skin temperature and emissivity, Proc. of the Int. ATOVS Study Conference-XIV.

Bradley, R., Diaz, H., Kiladis, G., Eischeid, J., 1987. ENSO signal in continental temperature and precipitation records. Nature 327, 497.

Cai, W., Santoso, A., Wang, G., Yeh, S.-W., An, S.-I., Cobb, K.M., Collins, M., Guilyardi, E., Jin, F.-F., Kug, J.-S., 2015. ENSO and greenhouse warming. Nature Climate Change 5, 849-859.

Cane, M.A., Zebiak, S.E., Dolan, S.C., 1986. Experimental forecasts of EL Nino. Nature 321, 827.

Chahine, M.T., Pagano, T.S., Aumann, H.H., Atlas, R., Barnet, C., Blaisdell, J., Chen, L., Divakarla, M., Fetzer, E.J., Goldberg, M., 2006. AIRS: Improving weather forecasting and providing new data on greenhouse gases. Bulletin of the American Meteorological Society 87, 911-926.

Chakraborty, S., Sasmal, S., Chakrabarti, S.K., Bhattacharya, A., 2018. Observational signatures of unusual outgoing longwave radiation (OLR) and atmospheric gravity waves (AGW) as precursory effects of May 2015 Nepal earthquakes. Journal of Geodynamics 113, 43-51.

Chandra, S., Ziemke, J., Min, W., Read, W., 1998. Effects of 1997–1998 El Nino on tropospheric ozone and water vapor. Geophysical Research Letters 25, 3867-3870.

Cho, H., Ho, C.H., Choi, Y.S., 2012. The observed variation in cloud-induced longwave radiation in response to sea surface temperature over the Pacific warm pool from MTSAT-1R imagery. Geophysical Research Letters 39.

Choi, Y.S., Ho, C.H., 2006. Radiative effect of cirrus with different optical properties over the tropics in MODIS and CERES observations. Geophysical Research Letters 33.

Chou, M.-D., Suarez, M.J., Liang, X.-Z., Yan, M.M.-H., Cote, C., 2001. A thermal infrared radiation parameterization for atmospheric studies.

Christensen, O.B., Christensen, J.H., Machenhauer, B., Botzet, M., 1998. Very high-resolution regional climate simulations over Scandinavia-Present climate. Journal of Climate 11, 3204-3229.

Clerbaux, N., Dewitte, S., Gonzalez, L., Bertrand, C., Nicula, B., Ipe, A., 2003. Outgoing longwave flux estimation: Improvement of angular modelling using spectral information. Remote Sensing of Environment 85, 389-395.

Comer, R.E., Slingo, A., Allan, R.P., 2007. Observations of the diurnal cycle of outgoing longwave radiation from the Geostationary Earth Radiation Budget instrument. Geophysical research letters 34.

Davis, R.E., 1978. Predictability of sea level pressure anomalies over the North Pacific Ocean. Journal of Physical Oceanography 8, 233-246.

Dee, D.P., Uppala, S., Simmons, A., Berrisford, P., Poli, P., Kobayashi, S., Andrae, U., Balmaseda, M., Balsamo, G., Bauer, P., 2011. The ERA-Interim reanalysis: Configuration and performance of the data assimilation system. Quarterly Journal of the royal meteorological society 137, 553-597.

Doelling, D.R., Loeb, N.G., Keyes, D.F., Nordeen, M.L., Morstad, D., Nguyen, C., Wielicki, B.A., Young, D.F., Sun, M., 2013. Geostationary enhanced temporal interpolation for CERES flux products. Journal of Atmospheric and Oceanic Technology 30, 1072-1090.

Ellingson, R.G., Yanuk, D.J., Lee, H.-T., Gruber, A., 1989. A technique for estimating outgoing longwave radiation from HIRS radiance observations. Journal of Atmospheric and Oceanic Technology 6, 706-711.

Elvidge, C.D., Zhizhin, M., Hsu, F.-C., Baugh, K., Khomarudin, M.R., Vetrita, Y., Sofan, P., Hilman, D., 2015. Long-wave infrared identification of smoldering peat fires in Indonesia with nighttime Landsat data. Environmental Research Letters 10, 065002.

Evans, R., Casey, K., Cornillon, P., 2010. Transition of AVHRR SST Pathfinder to Version 6, continued evolution of a CDR.

Feng, J.-M., Wang, Y.-L., Ma, Z.-G., 2015. Long-term simulation of large-scale urbanization effect on the East Asian monsoon. Climatic Change 129, 511-523.

Franch, B., Vermote, E.F., Roger, J.-C., Murphy, E., Becker-Reshef, I., Justice, C., Claverie, M., Nagol, J., Csiszar, I., Meyer, D., 2017. A 30+ year AVHRR land surface reflectance climate data record and its application to wheat yield monitoring. Remote Sensing 9, 296.

Fukuoka, A., 1951. A Study of 10-day Forecast (A Synthetic Report). The Geophysical Magazine: Tokyo XXII, 12.

Gehne, M., Kleeman, R., Trenberth, K.E., 2014. Irregularity and decadal variation in ENSO: a simplified model based on Principal Oscillation Patterns. Climate dynamics 43, 3327-3350.

Goldberg, M.D., Qu, Y., McMillin, L.M., Wolf, W., Zhou, L., Divakarla, M., 2003. AIRS near-real-time products and algorithms in support of operational numerical weather prediction. IEEE Transactions on Geoscience and Remote Sensing 41, 379-389.

Graham, N.E., Michaelsen, J., Barnett, T.P., 1987. An investigation of the El Niño-Southern Oscillation cycle With statistical models: 1. Predictor field characteristics. Journal of Geophysical Research: Oceans 92, 14251-14270.

Grimmond, S., 2007. Urbanization and global environmental change: local effects of urban warming. The Geographical Journal 173, 83-88.

Guan, H., Tremblay, A., Isaac, G.A., Strawbridge, K.B., Banic, C.M., 2000. Numerical simulations of stratus clouds and their sensitivity to radiation-A RACE case study. Journal of Applied Meteorology 39, 1881-1893.

Hannachi, A., Jolliffe, I., Stephenson, D., 2007. Empirical orthogonal functions and related techniques in atmospheric science: A review. International Journal of Climatology: A Journal of the Royal Meteorological Society 27, 1119-1152.

Hansen, J., Nazarenko, L., Ruedy, R., Sato, M., Willis, J., Del Genio, A., Koch, D., Lacis, A., Lo, K., Menon, S., 2005. Earth's energy imbalance: Confirmation and implications. science 308, 1431-1435.

Harries, J., Crommelynck, D., 1999. The geostationary earth radiation budget experiment on MSG-1 and its potential applications. Advances in Space Research 24, 915-919.

Harries, J.E., Brindley, H.E., Sagoo, P.J., Bantges, R.J., 2001. Increases in greenhouse forcing inferred from the outgoing longwave radiation spectra of the Earth in 1970 and 1997. Nature 410, 355.

Harries, J.E., Russell, J., Hanafin, J., Brindley, H., Futyan, J., Rufus, J., Kellock, S., Matthews, G., Wrigley, R., Last, A., 2005. The geostationary earth radiation budget project. Bulletin of the American Meteorological Society 86, 945-960.

Hovmöller, E., 1949. The trough-and-ridge diagram. Tellus 1, 62-66.

Hu, Y., Fu, Q., 2007. Observed poleward expansion of the Hadley circulation since 1979. Atmospheric Chemistry and Physics 7, 5229-5236.

Hu, Y., Zhou, C., Liu, J., 2011. Observational evidence for poleward expansion of the Hadley circulation. Advances in Atmospheric Sciences 28, 33-44.

Huang, B., Banzon, V.F., Freeman, E., Lawrimore, J., Liu, W., Peterson, T.C., Smith, T.M., Thorne, P.W., Woodruff, S.D., Zhang, H.-M., 2015. Extended Reconstructed Sea Surface Temperature (ERSST), Version 4. [Global]. NOAA National Centers for Environmental Information.

Huang, X., Chen, X., Potter, G.L., Oreopoulos, L., Cole, J.N., Lee, D., Loeb, N.G., 2014. A global climatology of outgoing longwave spectral cloud radiative effect and associated effective cloud properties. Journal of Climate 27, 7475-7492.

Huang, X., Ramaswamy, V., Schwarzkopf, M.D., 2006. Quantification of the source of errors in AM2 simulated tropical clear-sky outgoing longwave radiation. Journal of Geophysical Research 111.

Huang, X., Yang, W., Loeb, N.G., Ramaswamy, V., 2008. Spectrally resolved fluxes derived from collocated AIRS and CERES measurements and their application in model evaluation: Clear sky over the tropical oceans. Journal of Geophysical Research 113.

Huang, Y., Ramaswamy, V., Huang, X., Fu, Q., Bardeen, C., 2007. A strict test in climate modeling with spectrally resolved radiances: GCM simulation versus AIRS observations. Geophysical Research Letters 34.

Hudak, A.T., Dickinson, M.B., Bright, B.C., Kremens, R.L., Loudermilk, E.L., O'Brien, J.J., Hornsby, B.S., Ottmar, R.D., 2016. Measurements relating fire radiative energy density and surface fuel consumption–RxCADRE 2011 and 2012. International Journal of Wildland Fire 25, 25-37.

Inoue, H.Y., Sugimura, Y., 1992. Variations and distributions of CO2 in and over the equatorial Pacific during the period from the 1986/88 El Nino event to the 1988/89 La Nina event. Tellus B 44, 1-22.

Inoue, T., Ackerman, S.A., 2002. Radiative effects of various cloud types as classified by the split window technique over the eastern sub-tropical Pacific derived from collocated ERBE and AVHRR data. Journal of the Meteorological Society of Japan. Ser. II 80, 1383-1394.

Jin, E.K., Kinter, J.L., Wang, B., Park, C.-K., Kang, I.-S., Kirtman, B., Kug, J.-S., Kumar, A., Luo, J.-J., Schemm, J., 2008. Current status of ENSO prediction skill in coupled ocean–atmosphere models. Climate Dynamics 31, 647-664.

Johanson, C.M., Fu, Q., 2009. Hadley cell widening: Model simulations versus observations. Journal of Climate 22, 2713-2725.

Kalnay, E., Kanamitsu, M., Kistler, R., Collins, W., Deaven, D., Gandin, L., Iredell, M., Saha, S., White, G., Woollen, J., 1996. The NCEP/NCAR 40-year reanalysis project. Bulletin of the American meteorological Society 77, 437-471.

Kanamitsu, M., Ebisuzaki, W., Woollen, J., Yang, S.-K., Hnilo, J., Fiorino, M., Potter, G., 2002. Ncep–doe amip-ii reanalysis (r-2). Bulletin of the American Meteorological Society 83, 1631-1643.

Kandel, R., Viollier, M., Raberanto, P., Duvel, J.P., Pakhomov, L., Golovko, V., Trishchenko, A., Mueller, J., Raschke, E., Stuhlmann, R., 1998. The ScaRaB earth radiation budget dataset. Bulletin of the American Meteorological Society 79, 765-784.

Kang, C., Liu, D., 2001. The applicability of satellite remote sensing in monitoring earthquake. Science of Surveying and Mapping 26, 46-48.

Kim, B.-Y., Lee, K.-T., Jee, J.-B., Zo, I.-S., 2018. Retrieval of outgoing longwave radiation at top-of-atmosphere using Himawari-8 AHI data. Remote Sensing of Environment 204, 498-508.

Kirtman, B.P., 2003. The COLA anomaly coupled model: Ensemble ENSO prediction. Monthly weather review 131, 2324-2341.

Kistler, R., Collins, W., Saha, S., White, G., Woollen, J., Kalnay, E., Chelliah, M., Ebisuzaki, W., Kanamitsu, M., Kousky, V., 2001. The NCEP–NCAR 50–year reanalysis: Monthly means CD–ROM and documentation. Bulletin of the American Meteorological society 82, 247-267.

Kobayashi, S., Ota, Y., Harada, Y., Ebita, A., Moriya, M., Onoda, H., Onogi, K., Kamahori, H., Kobayashi, C., Endo, H., 2015. The JRA-55 reanalysis: General specifications and basic characteristics. Journal of the Meteorological Society of Japan. Ser. II 93, 5-48.

Lau, K.-M., Chan, P., 1986. Aspects of the 40–50 day oscillation during the northern summer as inferred from outgoing longwave radiation. Monthly Weather Review 114, 1354-1367.

Lau, K.-M., Chan, P.H., 1985. Aspects of the 40–50 day oscillation during the northern winter as inferred from outgoing longwave radiation. Monthly Weather Review 113, 1889-1909.

Lau, K.M., Ho, C.H., Chou, M.D., 1996. Water vapor and cloud feedback over the tropical oceans: Can we use ENSO as a surrogate for climate change? Geophysical research letters 23, 2971-2974.

Lee, H.-T., Ellingson, R.G., 2013. HIRS OLR climate data record–production and validation updates, AIP conference proceedings. AIP, pp. 420-423.

Lee, H.-T., Gruber, A., Ellingson, R.G., Laszlo, I., 2007. Development of the HIRS outgoing longwave radiation climate dataset. Journal of Atmospheric and Oceanic Technology 24, 2029-2047.

Lee, H.-T., Heidinger, A., Gruber, A., Ellingson, R.G., 2004. The HIRS outgoing longwave radiation product from hybrid polar and geosynchronous satellite observations. Advances in Space Research 33, 1120-1124.

Lee, T.F., Hawkins, J., Kuciauskas, A., Miller, S., 2010. Applications and Training for Next-Generation Imagers. American Meteorological Society.

Liang, S., 2003. A Direct Algorithm for Estimating Land Surface Broadband Albedos From MODIS Imagery. IEEE TRANSACTIONS ON GEOSCIENCE AND REMOTE SENSING 41, 10.

Liebmann, B., Smith, C., 1996a. Description of a complete (interpolated) OLR NOAA/NESDIS E/OC21, US Department of Commerce, Washington, DC, 117 pp. NOAA/NESDIS E/OC21, US Department of Commerce, Washington, DC, 99 pp. dataset. Bull. Amer. Meteor. Soc 77, 1275-1277.

Liebmann, B., Smith, C.A., 1996b. Description of a complete (interpolated) outgoing longwave radiation dataset. Bulletin of the American Meteorological Society 77, 1275-1277.

Lindzen, R.S., Choi, Y.-S., 2011. On the observational determination of climate sensitivity and its implications. Asia-Pacific Journal of Atmospheric Sciences 47, 377-390.

Liu, 2000. Anomalies analyses on satellite remote sensing OLR before Jiji earthquake of Taiwan Province. Geo-Information Science 2, 33-36.

Loeb, N.G., Doelling, D.R., Wang, H., Su, W., Nguyen, C., Corbett, J.G., Liang, L., Mitrescu, C., Rose, F.G., Kato, S., 2018. Clouds and the earth's radiant energy system (CERES) energy balanced and filled (EBAF) top-of-atmosphere (TOA) edition-4.0 data product. Journal of Climate 31, 895-918.

Loeb, N.G., Kato, S., Loukachine, K., Manalo-Smith, N., 2005. Angular distribution models for top-of-atmosphere radiative flux estimation from the Clouds and the Earth's Radiant Energy System instrument on the Terra satellite. Part I: Methodology. J. Atmos. Oceanic Technol 22, 338-351.

Loeb, N.G., Kato, S., Loukachine, K., Manalo-Smith, N., Doelling, D.R., 2007. Angular distribution models for top-of-atmosphere radiative flux estimation from the Clouds and the Earth's Radiant Energy System instrument on the Terra satellite. Part II: Validation. Journal of Atmospheric and Oceanic Technology 24, 564-584.

Loeb, N.G., Kato, S., Su, W., Wong, T., Rose, F.G., Doelling, D.R., Norris, J.R., Huang, X., 2012. Advances in understanding top-of-atmosphere radiation variability from satellite observations. Surveys in geophysics 33, 359-385.

Loeb, N.G., Manalo-Smith, N., Kato, S., Miller, W.F., Gupta, S.K., Minnis, P., Wielicki, B.A., 2003a. Angular distribution models for top-of-atmosphere radiative flux estimation from the Clouds and the Earth's Radiant Energy System instrument on the Tropical Rainfall Measuring Mission satellite. Part I: Methodology. Journal of applied meteorology 42, 240-265.

Loeb, N.G., Manalo-Smith, N., Kato, S., Miller, W.F., Gupta, S.K., Minnis, P., Wielicki, B.A., 2003b. Angular distribution models for top-of-atmosphere radiative flux estimation from the Clouds and the Earth's Radiant Energy System instrument on the Tropical

Rainfall Measuring Mission satellite. Part I: Methodology. Journal of applied meteorology 42, 240-265.

Loeb, N.G., Priestley, K.J., Kratz, D.P., Geier, E.B., Green, R.N., Wielicki, B.A., Hinton, P.O.R., Nolan, S.K., 2001. Determination of unfiltered radiances from the Clouds and the Earth's Radiant Energy System instrument. Journal of Applied Meteorology 40, 822-835.

Loeb, N.G., Wielicki, B.A., Doelling, D.R., Smith, G.L., Keyes, D.F., Kato, S., Manalo-Smith, N., Wong, T., 2009. Toward Optimal Closure of the Earth's Top-of-Atmosphere Radiation Budget. Journal of Climate 22, 748-766.

Lohmann, S., Schillings, C., Mayer, B., Meyer, R., 2006. Long-term variability of solar direct and global radiation derived from ISCCP data and comparison with reanalysis data. Solar energy 80, 1390-1401.

Lorenz, E.N., 1956. Empirical orthogonal functions and statistical weather prediction.

Loukachine, K., Loeb, N.G., 2004. Top-of-atmosphere flux retrievals from CERES using artificial neural networks. Remote Sensing of Environment 93, 381-390.

Lucas, C., Timbal, B., Nguyen, H., 2014. The expanding tropics: a critical assessment of the observational and modeling studies. Wiley Interdisciplinary Reviews: Climate Change 5, 89-112.

Mason, S.J., Goddard, L., Graham, N.E., Yulaeva, E., Sun, L., Arkin, P.A., 1999. The IRI seasonal climate prediction system and the 1997/98 El Niño event. Bulletin of the American Meteorological Society 80, 1853-1874.

Mayer, M., Fasullo, J.T., Trenberth, K.E., Haimberger, L., 2016. ENSO-driven energy budget perturbations in observations and CMIP models. Climate Dynamics 47, 4009-4029.

Mlawer, E.J., Taubman, S.J., Brown, P.D., Iacono, M.J., Clough, S.A., 1997. Radiative transfer for inhomogeneous atmospheres: RRTM, a validated correlated-k model for the longwave. Journal of Geophysical Research: Atmospheres 102, 16663-16682.

Morel, P., 1985. Plan for the implementation of the World Climate Research Programme. Advances in Space Research 5, 15-20.

Neelin, J.D., Dijkstra, H.A., 1995. Ocean-atmosphere interaction and the tropical climatology. Part I: the dangers of flux correction. Journal of climate 8, 1325-1342.

O'Brien, J.J., Loudermilk, E.L., Hornsby, B., Hudak, A.T., Bright, B.C., Dickinson, M.B., Hiers, J.K., Teske, C., Ottmar, R.D., 2016. High-resolution infrared thermography for capturing wildland fire behaviour: RxCADRE 2012. International Journal of Wildland Fire 25, 62-75.

Oleson, K., Monaghan, A., Wilhelmi, O., Barlage, M., Brunsell, N., Feddema, J., Hu, L., Steinhoff, D., 2015. Interactions between urbanization, heat stress, and climate change. Climatic Change 129, 525-541.

Onogi, K., Tsutsui, J., Koide, H., Sakamoto, M., Kobayashi, S., Hatsushika, H., Matsumoto, T., Yamazaki, N., Kamahori, H., Takahashi, K., 2007. The JRA-25 reanalysis. Journal of the Meteorological Society of Japan. Ser. II 85, 369-432.

Ouzounov, D., Liu, D., Chunli, K., Cervone, G., Kafatos, M., Taylor, P., 2007. Outgoing long wave radiation variability from IR satellite data prior to major earthquakes. Tectonophysics 431, 211-220.

Ouzounov, D., Pulinets, S., Romanov, A., Romanov, A., Tsybulya, K., Davidenko, D., Kafatos, M., Taylor, P., 2013. Atmosphere-Ionosphere Response to the M9 Tohoku Earthquake Revealed by Joined Satellite and Ground Observations. Preliminary results. Ref: arxiv. org/abs/1105.2841, DOI 10.

Park, M.-S., Ho, C.-H., Cho, H., Choi, Y.-S., 2015. Retrieval of outgoing longwave radiation from COMS narrowband infrared imagery. Advances in Atmospheric Sciences 32, 375-388.

Parrish, D.F., Derber, J.C., 1992. The National Meteorological Center's spectral statistical-interpolation analysis system. Monthly Weather Review 120, 1747-1763.

Pedelty, J., Devadiga, S., Masuoka, E., Brown, M., Pinzon, J., Tucker, C., Vermote, E., Prince, S., Nagol, J., Justice, C., Roy, D., Ju, J., Schaaf, C., Liu, J., Privette, J., Pinheiro, A., 2007. Generating a long-term land data record fromthe AVHRR and MODIS instruments. IEEE International Geoscience and Remote Sening Symposium, 1021-1024.

Philander, S.G., 1990. El Niño, La Niña, and the southern oscillation/by S. George Philander. San Diego: Academic Press, International geophysics series.

Pulinets, S., Ouzounov, D., 2011. Lithosphere–Atmosphere–Ionosphere Coupling (LAIC) model–An unified concept for earthquake precursors validation. Journal of Asian Earth Sciences 41, 371-382.

Rasmusson, E.M., Carpenter, T.H., 1982. Variations in tropical sea surface temperature and surface wind fields associated with the Southern Oscillation/El Niño. Monthly Weather Review 110, 354-384.

Rienecker, M.M., Suarez, M.J., Gelaro, R., Todling, R., Bacmeister, J., Liu, E., Bosilovich, M.G., Schubert, S.D., Takacs, L., Kim, G.-K., 2011. MERRA: NASA’s modern-era retrospective analysis for research and applications. Journal of climate 24, 3624-3648.

Ropelewski, C., Halpert, M., 1989. Precipitation patterns associated with the high index phase of the Southern Oscillation. Journal of climate 2, 268-284.

Ropelewski, C.F., Halpert, M.S., 1987. Global and regional scale precipitation patterns associated with the El Niño/Southern Oscillation. Monthly weather review 115, 1606-1626.

Rosati, A., Miyakoda, K., Gudgel, R., 1997. The impact of ocean initial conditions on ENSO forecasting with a coupled model. Monthly weather review 125, 754-772.

Saha, S., Moorthi, S., Pan, H.-L., Wu, X., Wang, J., Nadiga, S., Tripp, P., Kistler, R., Woollen, J., Behringer, D., 2010. The NCEP climate forecast system reanalysis. Bulletin of the American Meteorological Society 91, 1015-1057.

Schneider, E.K., Huang, B., Zhu, Z., DeWitt, D.G., Kinter III, J.L., Kirtman, B.P., Shukla, J., 1999. Ocean data assimilation, initialization, and predictions of ENSO with a coupled GCM. Monthly Weather Review 127, 1187-1207.

Schulz, J., Albert, P., Behr, H.-D., Caprion, D., Deneke, H., Dewitte, S., Durr, B., Fuchs, P., Gratzki, A., Hechler, P., 2009. Operational climate monitoring from space: the EUMETSAT Satellite Application Facility on Climate Monitoring (CM-SAF). Atmospheric Chemistry and Physics 9, 1687-1709.

SCOR, 1983. Prediction of El Niño. Proc. No. 19, Paris, France, Scientific Committee for Ocean Research Working Group 55, 47-51.

Seidel, D.J., Fu, Q., Randel, W.J., Reichler, T.J., 2008. Widening of the tropical belt in a changing climate. Nature geoscience 1, 21.

Shah, M., Khan, M., Ullah, H., Ali, S., 2018. THERMAL ANOMALIES PRIOR TO THE 2015 GORKHA (NEPAL) EARTHQUAKE FROM MODIS LAND SURFACE TEMPERATURE AND OUTGOING LONGWAVE RADIATIONS. GEODYNAMICS & TECTONOPHYSICS 9, 123-138.

Singh, A., Mohanty, U., Mishra, G., 2014. Long-Lead Prediction Skill of Indian Summer Monsoon Rainfall Using Outgoing Longwave Radiation (OLR): an Application of Canonical Correlation Analysis. Pure and Applied Geophysics 171, 1519-1530.

Soci, C., Fischer, C., Horányi, A., 2006. Sensitivity of high-resolution forecasts using the adjoint technique at the 10-km scale. Monthly weather review 134, 772-790.

Song, Z., Liang, S., Wang, D., Zhou, Y., Jia, A., 2018. Long-term record of top-of-atmosphere albedo over land generated from AVHRR data. Remote sensing of environment 211, 71-88.

Stackhouse, P.W., Zhang, T., Mikovitz, J.C., Hinkelman, L.M., 2011. The NASA/GEWEX Surface Radiation Budget Release 3.0: 24.5-Year Dataset. GEWEX News 21, 10-12.

Stephens, G.L., Li, J., Wild, M., Clayson, C.A., Loeb, N., Kato, S., L'Ecuyer, T., Stackhouse Jr, P.W., Lebsock, M., Andrews, T., 2012. An update on Earth's energy balance in light of the latest global observations. Nature Geoscience 5, 691-696.

Stockdale, T.N., Anderson, D.L., Alves, J.O.S., Balmaseda, M.A., 1998. Global seasonal rainfall forecasts using a coupled ocean–atmosphere model. Nature 392, 370.

Su, W., Loeb, N.G., Liang, L., Liu, N., Liu, C., 2017. The El Niño–Southern Oscillation effect on tropical outgoing longwave radiation: A daytime versus nighttime perspective. Journal of Geophysical Research: Atmospheres 122, 7820-7833.

Sugi, M., 1990. Description and performance of the JMA operational global spectral model (JMA-GSM88). Geophys. Magazine 43, 105-130.

Sun, F., Goldberg, M.D., Liu, X., Bates, J.J., 2010. Estimation of outgoing longwave radiation from Atmospheric Infrared Sounder radiance measurements. Journal of Geophysical Research: Atmospheres 115.

Trenberth, K.E., 1997a. The definition of el nino. Bulletin of the American Meteorological Society 78, 2771-2777.

Trenberth, K.E., 1997b. Forecasts of the development of the 1997-98 El Niño event, The 2nd Hayes Symposium on Seasonal to Interannual Climate Variability--The 1997/1998 ENSO Cycle.

Trenberth, K.E., Branstator, G.W., Karoly, D., Kumar, A., Lau, N.C., Ropelewski, C., 1998. Progress during TOGA in understanding and modeling global teleconnections associated with tropical sea surface temperatures. Journal of Geophysical Research: Oceans 103, 14291-14324.

Trenberth, K.E., Caron, J.M., Stepaniak, D.P., Worley, S., 2002. Evolution of El Niño–Southern Oscillation and global atmospheric surface temperatures. Journal of Geophysical Research: Atmospheres 107.

Trenberth, K.E., Fasullo, J.T., 2012. Tracking Earth’s energy: From El Niño to global warming. Surveys in geophysics 33, 413-426.

Trenberth, K.E., Fasullo, J.T., O'Dell, C., Wong, T., 2010. Relationships between tropical sea surface temperature and top-of-atmosphere radiation. Geophysical Research Letters 37.

Trenberth, K.E., Zhang, Y., Fasullo, J.T., Taguchi, S., 2015. Climate variability and relationships between top-of-atmosphere radiation and temperatures on Earth. Journal of Geophysical Research: Atmospheres 120, 3642-3659.

USGS, 2015. M 7.3 - 19km SE of Kodari, Nepal https://earthquake.usgs.gov/.

Vermote, E., Kaufman, Y., 1995. Absolute calibration of AVHRR visible and near-infrared channels using ocean and cloud views. International Journal of Remote Sensing 16, 2317-2340.

Vermote, E., Saleous, N., 2006. Calibration of NOAA16 AVHRR over a desert site using MODIS data. Remote sensing of Environment 105, 214-220.

Wang, D., Liang, S., 2016. Estimating high-resolution top of atmosphere albedo from Moderate Resolution Imaging Spectroradiometer data. Remote Sensing of Environment 178, 93-103.

Wang, D., Liang, S., He, T., Yu, Y., 2013. Direct estimation of land surface albedo from VIIRS data: Algorithm improvement and preliminary validation. Journal of Geophysical Research: Atmospheres 118.

Wang, P.H., Minnis, P., Wielicki, B.A., Wong, T., Vann, L.B., 2002. Satellite observations of long-term changes in tropical cloud and outgoing longwave radiation from 1985 to 1998. Geophysical research letters 29.

Wang, W., Liang, S., 2009. Estimation of high-spatial resolution clear-sky longwave downward and net radiation over land surfaces from MODIS data. Remote sensing of environment 113, 745-754.

Wang, W., Liang, S., Augustine, J.A., 2009. Estimating high spatial resolution clear-sky land surface upwelling longwave radiation from MODIS data. Geoscience and Remote Sensing, IEEE Transactions on 47, 1559-1570.

Weare, B.C., Nasstrom, J.S., 1982. Examples of extended empirical orthogonal function analyses. Monthly Weather Review 110, 481-485.

Wielicki, B.A., Barkstrom, B.R., Harrison, E.F., Lee III, R.B., Louis Smith, G., Cooper, J.E., 1996. Clouds and the Earth's Radiant Energy System (CERES): An earth observing system experiment. Bulletin of the American Meteorological Society 77, 853-868.

Wielicki, B.A., Harrison, E.F., Cess, R.D., King, M.D., Randall, D.A., 1995. Mission to planet Earth: Role of clouds and radiation in climate. Bulletin of the American Meteorological Society 76, 2125-2153.

Wild, M., Folini, D., Schär, C., Loeb, N., Dutton, E.G., König-Langlo, G., 2013. The global energy balance from a surface perspective. Climate dynamics 40, 3107-3134.

Wong, T., Wielicki, B.A., Lee III, R.B., Smith, G.L., Bush, K.A., Willis, J.K., 2006. Reexamination of the observed decadal variability of the earth radiation budget using altitude-corrected ERBE/ERBS nonscanner WFOV data. Journal of Climate 19, 4028-4040.

Xie, P., Arkin, P.A., 1998. Global monthly precipitation estimates from satellite-observed outgoing longwave radiation. Journal of Climate 11, 137-164.

Xiong, P., Shen, X., Bi, Y., Kang, C., Chen, L., Jing, F., Chen, Y., 2010. Study of outgoing longwave radiation anomalies associated with Haiti earthquake. Natural Hazards and Earth System Sciences 10, 2169.

Yanai, M., Tomita, T., 1998. Seasonal and interannual variability of atmospheric heat sources and moisture sinks as determined from NCEP–NCAR reanalysis. Journal of climate 11, 463-482.

Yuanjing, Z., Ting, T.N., Hunt, G.E., 2015. ANOMALIES IN OUTGOING LONGWAVE RADI-ATION AND THEIR POSSIBLE RELATIONSHIP TO PRECIPITATION IN CHINA DURING, Atmospheric Radiation: Progress and Prospects, Proceedings of the Beijing International Radiation Symposium-Beijing, China, August 26-30, 1986. Springer, p. 231.

Zelinka, M.D., Hartmann, D.L., 2011. The observed sensitivity of high clouds to mean surface temperature anomalies in the tropics. Journal of Geophysical Research: Atmospheres 116.

Zhang, X., Liang, S., Wang, G., Yao, Y., Jiang, B., Cheng, J., 2016. Evaluation of the reanalysis surface incident shortwave radiation products from NCEP, ECMWF, GSFC, and JMA using satellite and surface observations. Remote Sensing 8, 225.

Zopf, D., Short, K., Yang Kuo, R., 1978. Historical trends and statistics of the Southern Oscillation, El Nin o and Indonesian droughts. Fish. Bull 76, 663-678.